THE UNIVERSITY
of ADELAIDE

FACULTY OF SCIENCES, ENGINEERING AND TECHNOLOGY

SCHOOL OF PHYSICS, CHEMISTRY AND EARTH SCIENCES

The Structure of Baryon Resonances

Curtis David Abell

Supervisors:
Prof. Derek B. LEINWEBER
Prof. Anthony W. THOMAS

A thesis submitted in fulfillment of the requirements for the degree of Doctor of Philosophy

October 2023

ABSTRACT

Hamiltonian Effective Field Theory (HEFT) is a non-perturbative extension of effective field theory which provides a bridge between the infinite-volume scattering data of experiment, and finite-volume energy spectra from lattice QCD. By discretising a Hamiltonian which has been constrained to experimental scattering data, solving the eigenvalue equation for the Hamiltonian provides a finite-volume energy spectrum, which may be compared with lattice QCD eigenstates. In addition, eigenvectors of the Hamiltonian provide insight into the structure of these eigenstates. This matrix Hamiltonian has been made finite by finite-range regularisation, and by considering the range of regularisation parameters which allow the Hamiltonian to describe experimental scattering data, insight is gained into the degree of model-dependence in the infinite-volume and finite-volume quantities. This formalism is extended for the first time to systems with multiple quark-model like baryon states. By considering the effect of a second bare basis state on both the infinite-volume poles, and finite-volume energy spectrum, we gain a unique intuition into the relationship between these two regimes. Finally, we apply the multiple bare-baryon formalism to the odd-parity nucleon sector. We find that the interpretation of the two odd-parity nucleons as three-quark cores dressed by πN, ηN, and $K\Lambda$ two-particle states is consistent with both the experimental scattering data, and lattice QCD results at three lattice volumes. We also introduce a novel HEFT simulation of lattice QCD correlation functions, allowing for a determination of the two-particle scattering-state contamination in lattice QCD eigenstates.

STATEMENT OF ORIGINALITY

I certify that this work contains no material which has been accepted for the award of any other degree or diploma in my name, in any university or other tertiary institution and, to the best of my knowledge and belief, contains no material previously published or written by another person, except where due reference has been made in the text. In addition, I certify that no part of this work will, in the future, be used in a submission in my name, for any other degree or diploma in any university or other tertiary institution without the prior approval of the University of Adelaide and where applicable, any partner institution responsible for the joint award of this degree. The author acknowledges that copyright of published works contained within the thesis resides with the copyright holder(s) of those works.

I give permission for the digital version of my thesis to be made available on the web, via the University's digital research repository, the Library Search and also through web search engines, unless permission has been granted by the University to restrict access for a period of time.

I acknowledge the support I have received for my research through the provision of an Australian Government Research Training Program Scholarship.

Curtis David Abell

ACKNOWLEDGEMENTS

Firstly, this thesis could not have come together without the endless support and patience of my supervisors. To Derek, thank you for your constant enthusiasm for my projects, your willingness to have 2+ hour meetings until we're happy we understand a result, and for making Comp Phys workshops the highlight of my week. To Tony, I've always been in awe of the shear breadth of your physics knowledge, and your ability to reorient a conversation with incredibly insightful comments. I hope one day I can accumulate even a fraction of your physics knowledge. I'm also very grateful to Jia-Jun Wu for all of your assistance in helping me understand HEFT early on in my PhD, and for the many insightful physics discussions we've had during your several visits to Adelaide since then.

To everyone in the University of Adelaide physics department, I'm extremely grateful for the welcoming and friendly environment that everyone has had a role in cultivating. A special thanks goes to Sharon and Silvana for the endless work they put in making sure everything runs smoothly, and especially for the 2022 Cairns trip, which was the highlight of my time here. A huge thanks to every organiser and speaker for S4S, an incredible group without which I would be significantly poorer in my public speaking skills, general physics knowledge, and random trivia. Other departments have no idea what they're missing.

To all my fellow HDR students, past and present, thank you for making my time infinitely more bearable, particularly during a game of Officeball. I'm convinced that my most productive periods immediately followed an intense Officeball game. Thank you especially to Alec and Zeno, for the many hours spent discussing a crazy problem, both on a whiteboard and at the Unibar. To Shanette, Bill, and Josh, I'm glad I could always find solace with you all when I was struggling, and I'm especially thankful to Shanette for always encouraging me both to be myself, and to keep going when I was ready to give up. To Matt, Tom, Jolene, Adam, and Niki, thank you for all the brewery crawls, pool games, holidays, and wonderful distractions throughout my day. My world would be much darker without you all in it. Finally, to everyone I did not name who has been a meaningful part of my life over the last four years, know that I'm endlessly grateful for your friendship, and the times we probably shared at the Cranker.

And last, but never least, thank you to Mum, Dad, Livvy, and the rest of my family. You've provided me with a lifetime of support, encouragement, and love, for which I will never be able to fully express my gratitude for.

Love you all.

CONTENTS

1

INTRODUCTION

1.1 Quantum Chromodynamics

In our modern understanding of the universe, almost all observable phenomena may be described by four fundamental interactions. The first of these, gravity, is described by general relativity, and yet to be successfully formulated in a quantum system. The remaining three interactions, electromagnetism, the weak force, and the strong force, are well-described by quantum field theories, collectively referred to as the Standard Model.

Of the three fundamental interactions which may be described by quantum field theories, the modern understanding of the strong interaction, known as Quantum Chromodynamics (QCD), is perhaps the most mysterious. QCD is a non-abelian gauge theory [1, 2], described by the symmetry group SU(3), where the conserved quantities for the theory are referred to as colour charge, along with the complimentary anticolour charges. The three coloured charges are labelled red, green, and blue, along with the corresponding anticolour charges, antired, antigreen, and antiblue (commonly illustrated with cyan, magenta, and yellow respectively). Interactions between coloured particles are mediated by the eight gauge bosons collectively known as the gluon. As gluons carry both a colour and an anticolour, there are eight possible combinations which do not result in a colourless (white) state.

In the Standard Model, coloured fermions are known as quarks, of which there are six flavours, and carry a single colour charge. Similarly, antiquarks carry a single anticolour. The six flavours of quark are summarised in Table 1.1, and are divided into the three "up-type" quarks, with electric charge $+2/3$, and the three "down-type" quarks, with charge $-1/3$.

Importantly, at low energy we do not observe free quarks and gluons, only colourless combinations of quarks, antiquarks, and gluons. This property is called colour confinement, the source of which is a long-standing mystery in QCD. Recent years however have seen considerable progress in understanding this phenomena [4, 5]. The colourless composite states which we observe due to colour confinement are primarily formed from a combination of quarks and gluons, known as hadrons, and have an integer electric charge. Hadronic matter forms the majority of visible matter in the universe, and is catagorised into one of two types of composite particles.

Mesons are formed from an equal number of (valence) quarks and antiquarks, resulting in an integer spin. The lightest mesons, with a mass of approximately 140 MeV, are the charged pions, π^+ and π^-, and the neutral pion, π^0. In terms of their quark compo-

Table 1.1: The six quark flavours, along with their electric charges. The $\overline{\text{MS}}$ masses of the three light quarks are quoted at a $\mu = 2$ GeV renormalisation scale. The c and b quark $\overline{\text{MS}}$ masses are reported at the running mass with $\mu = \overline{m_c}$ and $\mu = \overline{m_b}$ respectively. The t quark mass is extracted from $t\bar{t}$ cross-section measurements [3].

Flavour	Symbol	Mass (MeV)	Electric Charge (e)
Up	u	2.16	+2/3
Down	d	4.67	-1/3
Strange	s	93.4	-1/3
Charm	c	1270	+2/3
Bottom	b	4180	-1/3
Top	t	172700	+2/3

sition, these three pions may be written as $\pi^+ = u\bar{d}$, $\pi^- = d\bar{u}$, and $\pi^0 = \frac{1}{\sqrt{2}}\left(u\bar{u} - d\bar{d}\right)$. While the pions are the lightest hadronic state, they are unstable, with charged pions only having a lifetime of only $\sim 2.6 \times 10^{-8}$ seconds [3]. Despite this, they are particularly important in the interactions between hadronic states. This interaction is known as the strong nuclear force, and is typically mediated by pion exchange.

Hadronic states may also form spin-$1/2$ states, denoted baryons, and are composed of an odd number of quarks and antiquarks. Typically, baryons are composed of three quarks (qqq) or three antiquarks ($\bar{q}\bar{q}\bar{q}$), though exotic quark compositions such as $qqqq\bar{q}$ are also permitted. The lightest baryon states are the proton (uud) and neutron (udd).

At high energy, quarks and gluons interact weakly. This is a property of QCD known as asymptotic freedom [6], and it is only at this energy scale that one is able to analyse QCD perturbatively. At lower energies, where quarks and gluons are confined to hadronic states, this coupling becomes the order of one. As a result, all orders of diagram contribute to a scattering amplitude, and in the study of low-lying hadronic states we therefore require non-perturbative techniques. To motivate the use of non-perturbative techniques in the study of baryon states in particular, we must first consider how baryons are structured within the quark model.

1.2 Baryon Resonances

In this dissertation, we will focus on hadrons which are composed of the three lightest quarks: the up, down, and strange quarks. As the up and down quarks have similar constituent quark masses, they form a good approximation of the SU(2) symmetry group. The conserved quantity for this symmetry is isospin ($\boldsymbol{I}$), and utilising this approximation allows us to represent protons and neutrons as the $I = 1/2$ states of the nucleon (N), distinguished by isospin projections $I_3 = \pm 1/2$. Similarly for mesons, the three pions may be considered as three isospin states of the general pion (π), which has total isospin $I = 1$. Much like angular momentum, which is also a representation of SU(2), the number of isospin states for a total isospin I is given by $2I + 1$.

More generally, we may construct the set of ground-state spin-$1/2$ baryons by considering combinations of u, d, and s quarks. In addition to isospin, particles are labelled by their strangeness, given by $S = n_{\bar{s}} - n_s$, where n_s and $n_{\bar{s}}$ count the number of strange and antistrange quarks in the baryon. To construct a physical baryon, we require a total baryon number of one, and an integer charge. There are eight ground-state baryons which satisfy this condition: the p^+ and n^0, which have strangeness 0, the Σ^+, Σ^0, Σ^-, and Λ^0, which have strangeness -1, and the Ξ^0 and Ξ^-, which have strangeness -2. Under isospin symmetry, these may be simply referred to as the N, Σ, Λ, and Ξ baryons. Similarly, through a consideration of the spin-$3/2$ baryons, we obtain the baryon decuplet, which under isospin symmetry consists of the Δ, Σ^*, Ξ^*, and Ω baryons. These multiplets are naturally obtained by considering the three light quarks as forming an approximate SU(3) flavour symmetry, forming the basis of Gell-Mann's "Eightfold Way" [7].

In a scattering experiment, such as pion-nucleon scattering, a commonly measured quantity is the cross-section σ, measured in units of barns (100 fm^2). The cross-section measures the probability of a collision occurring, and may be qualitatively expressed in terms of the differential cross-section as

$$\frac{d\sigma}{d\Omega} = \frac{\text{\# particles scattered/sec/unit solid angle/target particle}}{\text{\# particles incident/sec/unit area}} \, . \tag{1.1}$$

In a scattering experiment where the cross-section is measured, it is common to observe "peaks" in the cross-section at certain centre-of-mass energies E. These peaks are referred to as "resonances", where the mass of the resonance is typically considered to be the E which corresponds with the peak. In addition, resonances are considered to have a width (Γ), corresponding to the full-width half-maximum of the cross-sectional peak. This is of particular interest, as the lifetime (τ) of the resonant state is given by $\tau = \hbar/\Gamma$.

In a simple pion-nucleon scattering experiment, we may better understand these resonances by performing partial-wave analysis, where the scattering amplitude is decomposed into a series of partial-waves, representing the relative angular momentum between the pion and the nucleon. For angular momentum l, this takes the form

$$f(k,\theta) = \sum_l (2l+1)\, P_l(\cos\theta)\, \frac{e^{i\delta_l(k)}\, \sin\delta_l}{k} \, , \tag{1.2}$$

where $P_l(\cos\theta)$ are the Legendre polynomials, and $\delta_l(k)$ is the phase shift at momentum k. This scattering amplitude may be related back to the cross-section by the Optical Theorem [2],

$$\sigma(k) = \frac{4\pi}{k}\, \operatorname{Im} f(k,0) \, . \tag{1.3}$$

Given this partial-wave decomposition, we may consider the cross-section for specific angular momentum, providing insight into the quantum numbers of the resonances in the scattering process. Following the convention from atomic spectroscopy, partial-wave states are named the S, P, D, F, and G-waves for $l = 0, 1, 2, 3, 4$, where the alphabet is followed for higher angular momenta. As an example, the lowest lying resonance in P-wave pion-nucleon scattering has a mass of 1.232 GeV, and is identified as the Δ baryon.

As a result, it is commonly referred to as both the Δ baryon, and as the Δ resonance depending on the context.

Due to the wealth of πN scattering data, along with other scattering processes, considering only the N and Δ channels there are well over 50 recorded resonances [3]. While many of these resonances are able to be described by the quark model, the reality is far more complicated. Considering the low-lying N resonances alone, we have the surprising result of the first positive-parity excitation of the nucleon lying below the first negative-parity excitation, contrary to simple quark model predictions [8, 9]. Along with issues in quark model predictions, whether particular resonances even correspond with quark model states is in question, such as for the $\Lambda^*(1405)$, which lies near the $\overline{K}N$ threshold, and contains two nearby poles [10, 11]. As such, it is clear that the quark model alone cannot describe the diverse baryon spectrum. In particular, given the non-perturbative nature of QCD at low-energy, we will consider how we can gain insight into the structure of baryons through finite-volume physics.

1.3 Lattice QCD

Lattice QCD [12, 13] is a first principles, non-perturbative approach to QCD. While the details of conducting a lattice QCD study are beyond the scope of this dissertation, we will proceed with a brief overview of the relevant physics. In lattice QCD, space-time is discretised into a grid of space-time points, separated by a lattice spacing a. Considering a lattice with n spatial sites, and n_t temporal sites, the spatial extent of the lattice is given by $L = n\,a$, and the temporal extent is given by $L_t = n_t\,a$. This therefore results in a four-dimensional volume $V = L^3\,L_t$. Typically, a lattice is constrained to have periodic boundary conditions, although antiperiodic and twisted boundary conditions may also be taken. In the periodic case, the lattice may be visualised as a four-dimensional torus.

As lattice QCD is formulated using the path integral approach, we may define the generating function for a field ψ as

$$\mathcal{Z} = \int \mathcal{D}\psi \, \exp\left(iS[\psi]\right) \,, \tag{1.4}$$

where in QCD, the action is given by $S[\psi] = \int d^4x \, \mathcal{L}_{\text{QCD}}(\psi; x)$. We may therefore calculate the expectation value for an observable $\mathcal{O}$ as

$$\langle \mathcal{O} \rangle = \frac{1}{\mathcal{Z}} \int \mathcal{D}\psi \, \mathcal{O}[\psi] \, \exp\left(iS[\psi]\right) \,. \tag{1.5}$$

Considering this expression, we observe that the generating function $\mathcal{Z}$ almost has the form of a partition function, as typically defined in statistical mechanics. The key difference is the presence of the imaginary unit in the exponential. By performing a Wick rotation [14], where $t \to i\tau$, we rotate the system into Euclidean space, with Euclidean time τ. As a result, the generating function takes the form of a partition function,

$$\mathcal{Z} = \int \mathcal{D}\psi \, \exp\left(-S[\psi]\right) \, , \tag{1.6}$$

allowing for the formulation of lattice QCD. As a result of this Wick rotation and the finite volume, the asymptotic states utilised in scattering theory are unachievable, and therefore scattering as typically considered cannot be performed.

Despite this, lattice QCD has proven successful in many aspects of fundamental research. In the context of baryon spectroscopy, one can construct baryons in lattice QCD by constructing operators $\chi_i(\boldsymbol{x}, t)$ with quantum numbers corresponding to the baryons of interest. By acting on the QCD vacuum, given by $|\Omega\rangle$, a correlation matrix may be constructed of the form

$$G_{ij}(\boldsymbol{p}, t) = \sum_{\boldsymbol{x}} e^{-i\boldsymbol{p}\cdot\boldsymbol{x}} \, \left\langle \overline{\Omega} \right| \chi_i(\boldsymbol{x}, t) \, \overline{\chi_j}(0, 0) \, |\Omega\rangle \, . \tag{1.7}$$

The energy of the finite-volume eigenstates may be extracted through established generalised eigenvalue equation techniques. In order to compare these finite-volume energy eigenstates to experiment however, a formalism relating lattice QCD and the continuum is required.

1.3.1 Lüscher's Method

In order to relate the discretised, Euclidean-time quantities from lattice QCD to experimental scattering results, Lüscher's method [15–17] was formulated. This formalism provides a relationship between the finite-volume energy eigenstates from lattice QCD to scattering observables such as the phase shift. Consider a simple case of low-energy πN scattering, where only one scattering channel is open. Given a finite-volume energy eigenvalues of energy E_i, one could solve for the corresponding back-to-back πN momentum k_i from $E_i = \sqrt{k_i^2 + m_\pi^2} + \sqrt{k_i^2 + m_N^2}$, giving

$$k_i^2 = \frac{E_i^2}{4} + \frac{\left(m_N^2 - m_\pi^2\right)^2}{4E_i^2} - \frac{m_\pi^2 + m_N^2}{2} \, . \tag{1.8}$$

Converting this momentum to the dimensionless $q_i = k_i L / 2\pi$, where L is the lattice extent, Lüscher's method provides a relationship to phase shifts

$$\delta(q_i) = j\pi + \mathrm{atan}\left(\frac{\pi^{3/2} \, q_i}{\mathcal{Z}_{00}(1, q_i^2)}\right) \, . \tag{1.9}$$

The integer j allows for multiple phase shifts at a given momentum, allowing for the periodicity of the arctangent function. Here, we have also defined the generalised Zeta function,

$$\mathcal{Z}_{00}(s,q^2) = \frac{1}{\sqrt{4\pi}} \sum_{\boldsymbol{n}\in\mathbb{Z}^3} \frac{1}{(n^2-q^2)^s} \,. \tag{1.10}$$

As this form of the generalised Zeta function possesses divergences, we instead utilise a regularised form [18], given by

$$\mathcal{Z}_{00}(q^2) = \frac{1}{\sqrt{4\pi}} \left(-\frac{1}{q^2} - 8.91383282 + 16.53231596\, q^2 + \sum_{\boldsymbol{n}\in\mathbb{Z}^3, \boldsymbol{n}\neq\boldsymbol{0}} \frac{q^4}{n^4\,(n^2-q^2)} \right) . \tag{1.11}$$

Given the regularised Zeta function, we can therefore solve for the phase shifts corresponding with a finite-volume energy eigenstate of energy E.

While this process is relatively straightforward, the generalised case with multiple scattering channels [19–25], and three-body systems [26–28] is considerably more complicated. In particular, they require a parametrisation of the scattering observables, to account for the additional observables corresponding with a particular finite-volume eigenstate, at a particular lattice size L.

As an alternative, this dissertation will consider Hamiltonian Effective Field Theory (HEFT) as a formalism for relating finite-volume eigenstates to infinite-volume scattering observables. Indeed it has been demonstrated [18, 29] that Lüscher's formalism is embedded within HEFT, up to exponentially suppressed corrections. In addition to this relationship, HEFT provides additional information in the eigenvectors of the Hamiltonian, providing key insights into the structure of baryon resonances.

1.4 Outline

In Chapter 2, we commence this dissertation with a review of the Hamiltonian Effective Field Theory (HEFT) formalism, with a particular emphasis on the full coupled-channel, multiple bare state extraction of the scattering observables. In Sec. 2.4.6, we also introduce a novel formalism for the single bare state HEFT simulation of lattice QCD correlation functions, and how these can be utilised to find two-particle scattering state contaminations.

In Chapter 3, we conduct an overview of how finite-range regularisation manifests in HEFT, using the $\Delta(1232)$ as a case study. Our aim in this chapter is to investigate how the regularisation scheme affects model-dependent quantities in particular, such as the eigenvectors of the Hamiltonian. By considering the effects of the regulator, we probe the extent into which one can gain insight into the structure of a baryon through a HEFT analysis, in a vast range of regularisation parameters, and multiple regulators. This chapter initially considers the single-channel case, where the Hamiltonian is fully constrained by πN scattering data in the energy range considered. This allows us to consider the fullest range of regulator parameters possible, and view the effects of varying this degree of regularisation on both infinite-volume and finite-volume quantities. In the second half of this chapter, we consider the more complicated two-channel case, where the lack of $\pi\Delta$ scattering data prevents the Hamiltonian from being fully constrained. We investigate the degree to which this manifests in both infinite-volume and finite-volume quantities, and view how we may take guidance from lattice QCD results to constrain the Hamiltonian, reducing the degree of model-dependence.

Chapter 4 provides the first investigation into the use of two bare-baryon basis states in HEFT, in a toy model extension of the low-energy $\Delta(1232)$ system. By considering this low-energy system, we are able to gain intuition into how the introduction of a second bare basis state affects the position of the original $\Delta(1232)$ pole, without considering complex coupled-channel effects. In addition, by comparing the pole movements to how the finite-volume energy spectrum is affected, we are able to gain unique insights into the relationship between poles in the T-matrix, and the finite-volume spectrum.

Building on the confidence gained in Chapter 3 as to the ability of HEFT to describe a physical system independent of regularisation scheme, as well as the unique insight gained in Chapter 4 into the effects of introducing a second bare basis state, in Chapter 5 we conduct an analysis of the two low-lying odd-parity nucleon resonances using two bare basis states. By constraining the Hamiltonian to experimental scattering data, we are able to obtain pole positions for each of the two nucleon states in agreement with established results. In addition, we compare finite-volume HEFT to lattice QCD results at three lattice volumes. By associating lattice QCD eigenstates with HEFT energy eigenstates, we are able to gain insight into the structure of these eigenstates through eigenvector analysis. We also introduce an extension of the contamination function formalism for a system with two bare basis states, allowing for a novel simulation of both two-particle and single-particle contaminations in lattice QCD eigenstates.

Finally, Chapter 6 summarises the results presented in this dissertation.

2

HAMILTONIAN EFFECTIVE FIELD THEORY

Hamiltonian Effective Field Theory (HEFT) [8–10, 18, 29–35] is a non-perturbative extension of effective field theory, providing a bridge between infinite-volume scattering theory and the finite-volume of lattice QCD. By parametrising the interactions between bare basis states and coupled two-particle channels, one can constrain a Hamiltonian to experimental scattering data. Formulating the Hamiltonian in a finite volume, energy eigenvalues for the system can be found, which can be used to make a connection with lattice QCD quantities. This relationship between infinite-volume scattering quantities and finite-volume lattice QCD quantities is guaranteed at low-energies by Lüscher's formalism. By isolating the pole term within the eigenvalue equation for the Hamiltonian, one obtains an expression equivalent to Lüscher's formula, up to exponentially suppressed terms in $m_\pi L$ [18]. In addition, eigenvectors of the Hamiltonian provide insight into the structure and composition of these eigenstates.

This chapter will describe the details of the HEFT approach, beginning with the motivation for the formalism from finite-range regularisation in conventional perturbation theory. Following that, we will build the Hamiltonian in an infinite-volume, providing a mechanism for constraining the Hamiltonian using scattering observables. This constrained Hamiltonian will then be considered in a finite-volume, and extended to unphysical pion masses, allowing for comparison with lattice QCD.

2.1 Finite-Range Regularisation in Perturbation Theory

Finite-range regularisation (FRR) is a regularisation scheme which introduces a finite-range regulator, $u(k, \Lambda)$, a function which removes higher-momentum contributions at a rate governed by the regulator parameter Λ. In principle, the regulator can be any form factor which equals one at $k = 0$, and negates higher-momentum contributions, the simplest example being a step function which equals one for $k \leq \Lambda$, and zero for $k > \Lambda$. Phenomenologically however, the regulator can be considered representative of the size of the interaction considered. As an example, for a dipole form factor, a regulator parameter of $\Lambda \sim 0.8$ GeV can be considered as an interaction with a range of ~ 1 fm, or the size of a light baryon. As such, this dissertation will focus on smooth, phenomenologically motivated regulator forms which represent the source of the interaction.

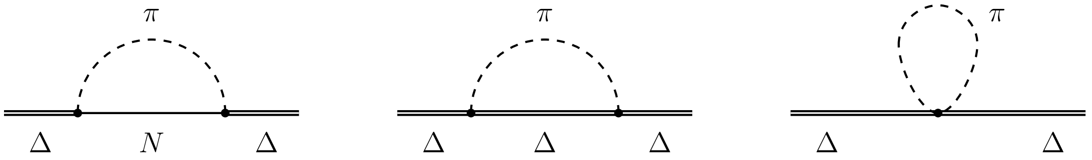

Figure 2.1: Self-energy contributions to the Δ mass, giving rise to the terms $\Sigma_{\pi N}(m_\pi^2, \Lambda)$, $\Sigma_{\pi\Delta}(m_\pi^2, \Lambda)$, and $\Sigma_{t\Delta}(m_\pi^2, \Lambda)$ in Eq. (2.1).

While within the power-counting regime (PCR) the choice of regulator form is unimportant [36–38], the regulator form is particularly important as one moves beyond the PCR. In Ref. [36], comparison was made between FRR and the more common technique of dimensional regularisation in χPT. There it was found that while within the power-counting regime ($m_\pi \sim m_\pi^{\mathrm{phys}}$), FRR was able to achieve equivalent reproductions of the nucleon mass, for all regulator forms considered and at all pion masses [36]. Beyond this region, the expansion of FRR is regulator-dependent, and therefore the regulator takes on the role of modelling the chiral expansion, allowing one to extend the range of utility [36–38]. The resummation of higher-order terms in this expansion ensures that as one moves to higher pion masses outside the PCR, contributions from higher-order loop intergrals smoothly approach zero. In particular, FRR allows for a preservation of the leading nonanalytic terms from chiral perturbation theory, as the coefficients of these terms are independent of the regulator parameter Λ.

As a demonstration, and motivation for the residual series expansion of the Δ baryon as considered in Chapter 3, consider the quark-mass expansion ($m_q \propto m_\pi^2$ [39]) of the Δ baryon in χPT, which takes the form [40]

$$\begin{aligned} m_\Delta(m_\pi^2) = {} & a_0^\Lambda + a_2^\Lambda\, m_\pi^2 + a_4^\Lambda\, m_\pi^4 + \cdots \\ & + \Sigma_{\pi N}(m_\pi^2, \Lambda) + \Sigma_{\pi\Delta}(m_\pi^2, \Lambda) + \Sigma_{t\Delta}(m_\pi^2, \Lambda)\,. \end{aligned} \tag{2.1}$$

The leading order terms in this expansion are referred to as the residual series expansion, and contain model-dependent coefficients a_i^Λ. Also present are the self-energy terms $\Sigma_{\pi N}(m_\pi, \Lambda)$, which describe the interactions between the Δ baryon and πN two-particle states, $\Sigma_{\pi\Delta}(m_\pi, \Lambda)$, which describes the same but for $\pi\Delta$ states, and $\Sigma_{t\Delta}(m_\pi, \Lambda)$, describing the contribution from the tadpole diagram. These three self-energy contributions are represented diagrammatically in Fig. 2.1. Additionally, these self-energy quantities are regulated by the regulator $u(k, \Lambda)$, at a rate governed by the regulator parameter Λ.

This finite-range regulator generates a resummation of the ultraviolet terms in Eq. (2.1), in a form dependent on both the choice of regulator form, and regulator parameter, which is also manifest in the Λ-dependent coefficients a_i^Λ. Within the power-counting regime, the Λ-dependent portions of the self-energies are absorbed into the coefficients a_i^Λ, giving a model-independent expansion up to terms suppressed by powers of m_π/Λ. Outside of the PCR, this resummation provides a model for higher-order terms.

Utilising the heavy-baryon approximation for ease of presentation, and a dipole form factor for the regulator, these self-energies may be analytically evaluated to

$$\Sigma_{\pi\Delta}(m_\pi^2,\Lambda) = b_0^\Delta\,\Lambda^3 + b_2^\Delta\,\Lambda\,m_\pi^2 + \chi_{\pi\Delta}\,m_\pi^3 + b_4^\Delta\,\frac{m_\pi^4}{\Lambda} + \cdots\,, \tag{2.2a}$$

$$\Sigma_{\pi N}(m_\pi^2,\Lambda) = b_0^N\,\Lambda^3 + b_2^N\,\Lambda\,m_\pi^2 + \chi_{\pi N}\,\frac{m_\pi^4}{\delta M}\,\log m_\pi + b_4^N\,\frac{m_\pi^4}{\Lambda} + \cdots\,, \tag{2.2b}$$

$$\Sigma_{t\Delta}(m_\pi^2,\Lambda) = b_2^t\,\Lambda^2\,m_\pi^2 + c_2\,\chi_{t\Delta}\,m_\pi^4\,\log m_\pi + b_4^t\,m_\pi^4 + \cdots\,, \tag{2.2c}$$

where δM is the mass-splitting between the Δ baryon and the nucleon at the chiral limit ($m_\pi = 0$), and $\chi_{\pi\Delta}$, $\chi_{\pi N}$ and $\chi_{t\Delta}$ are model-independent coefficients [38]. The value c_2 appears within the contribution from the tadpole diagram as it originates from the term in the chiral Lagrangian proportional to the quark mass (where $m_q \sim m_\pi^2$), and $c_2\,m_\pi^2$ is responsible for the quark-mass expansion at leading order, as is described in the following text.

Here, one observes both nonanalytic terms, and terms polynomial in m_π^2. Inserting these self-energy expansions into Eq. (2.1), we are able to gather terms by powers of m_π and define the constants c_i,

$$c_0 = a_0^\Lambda + b_0^\Delta\,\Lambda^3 + b_0^N\,\Lambda^3\,, \tag{2.3a}$$

$$c_2 = a_2^\Lambda + b_2^\Delta\,\Lambda + b_2^N\,\Lambda + b_2^t\,\Lambda^2\,, \tag{2.3b}$$

$$c_4 = a_4^\Lambda + \frac{b_4^\Delta}{\Lambda} + \frac{b_4^N}{\Lambda} + b_4^t\,. \tag{2.3c}$$

Through the definitions of these constants, it can be seen that the model-dependence of the expansion may be absorbed into the free coefficients a_i^Λ, and therefore the coefficients c_i are made model-independent within the power-counting regime. Given these definitions, the Δ-mass expansion is therefore of the form

$$\begin{aligned} m_\Delta(m_\pi^2) = c_0 + c_2\,m_\pi^2 + \chi_{\pi\Delta}\,m_\pi^3 + c_4\,m_\pi^4 \\ + \left(\frac{\chi_{\pi N}}{\delta M} + c_2\,\chi_{t\Delta}\right)\,m_\pi^4\,\log m_\pi + \cdots\,. \end{aligned} \tag{2.4}$$

It is clear that the values of the coefficients are determined from the choice of regulator parameter Λ. In practice, a regulator parameter of order 1 GeV is able to both remove necessary short-distance contributions, and phenomenologically represents the size of source of the pion cloud. As the coefficients of the residual series describe the short-distance physics, they may be thought of as an expansion describing the dressing of a "bare" baryon, a concept which will heavily feature in this thesis. This intuition into the role of the regulator is particularly useful for HEFT. An appropriate choice of Λ allows for the higher-order coefficients in the expansion to be minimised. As such, the first few terms of the residual series expansion are able to provide a basis for comparison with lattice QCD results at unphysical pion masses. This will be considerably explored in Chapter 3, where the influence of the choice of Λ is explicitly explored.

2.2 Hamiltonian Formalism

In the rest frame, where the centre-of-mass momentum is zero, the Hamiltonian for a system of particles can be deconstructed into the sum of two Hamiltonians,

$$H = H_0 + H_{\mathrm{I}} \,. \tag{2.5}$$

The first, denoted the free Hamiltonian and labelled H_0, consists of two types of states. The first type of state is a non-interacting two-particle state with back-to-back momentum $\boldsymbol{k}$, which may be labelled $|\alpha(\boldsymbol{k})\rangle$, consisting of particles α_{M} and α_{B}. These represent the meson and baryon constituents of meson-baryon scattering, though this formalism also applies for meson-meson scattering. However, as this thesis focuses on pion-nucleon scattering, we will label these particles as mesons and baryons for clarity. The energy associated with such a state is defined as

$$\omega_\alpha(\boldsymbol{k}) = \omega_{\alpha_{\mathrm{M}}}(\boldsymbol{k}) + \omega_{\alpha_{\mathrm{B}}}(-\boldsymbol{k}) = \sqrt{k^2 + m_{\alpha_{\mathrm{M}}}} + \sqrt{k^2 + m_{\alpha_{\mathrm{B}}}} \,, \tag{2.6}$$

where $m_{\alpha_{\mathrm{M}}}$ and $m_{\alpha_{\mathrm{B}}}$ are the physical masses of particles α_{M} and α_{B} respectively. Along with two-particle states, this formalism also allows for the presence of single-particle bare basis states in the Hamiltonian, labelled $|B_0\rangle$, with unphysical masses $m_{B_0}^{(0)}$. These bare states may be thought of as quark model-like states, or those generated in lattice QCD from two or three-quark interpolating field operators. In the notation of Ref. [41], these may be described as states in P-space. For a Hamiltonian with n_c two-particle states and n_b bare states, H_0 therefore takes the form

$$H_0 = \sum_{B_0}^{n_b} |B_o\rangle\, m_{B_0}^{(0)}\, \langle B_0| + \sum_{\alpha}^{n_c} \int d^3k\ |\alpha(\boldsymbol{k})\rangle\, \omega_\alpha(\boldsymbol{k})\, \langle \alpha(\boldsymbol{k})| \ . \tag{2.7}$$

The interaction Hamiltonian H_{I} describes two types of interactions. Interactions between two-particle states $|\alpha(\boldsymbol{k})\rangle$ and $|\beta(\boldsymbol{k'})\rangle$ are parameterised by a momentum-dependent, potential labelled $V_{\alpha\beta}(\boldsymbol{k}, \boldsymbol{k'})$, and governed by an energy-independent coupling strength $v_{\alpha\beta}$. Typically the potential is chosen such that $v_{\alpha\beta}$ is dimensionless. An example of this interaction for two πN two-particle states is given by the middle vertex of the right-most diagram in Fig. 2.2. This interaction is denoted by v, and given a normalisation of $\langle \beta(\boldsymbol{k'})|\alpha(\boldsymbol{k})\rangle = \delta_{\alpha\beta}\, \delta(\boldsymbol{k} - \boldsymbol{k'})$ is

$$v = \sum_{\alpha,\beta} \int d^3k \int d^3k'\ |\alpha(\boldsymbol{k})\rangle\, V_{\alpha\beta}(\boldsymbol{k}, \boldsymbol{k'})\, \langle \beta(\boldsymbol{k'})| \ . \tag{2.8}$$

Similarly, the interactions between a scattering state $|\alpha(\boldsymbol{k})\rangle$ and a bare state $|B_0\rangle$ are parameterised by a momentum-dependent potential labelled $G_\alpha^{B_0}(\boldsymbol{k})$, and are governed

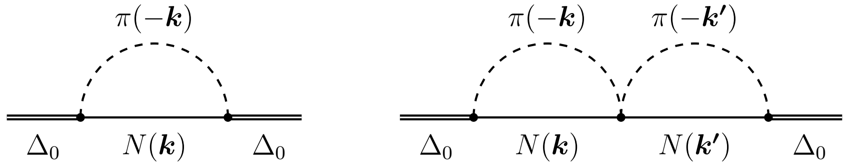

Figure 2.2: Example dressing of a bare Δ_0 state. These include an interaction between a bare Δ baryon and a πN scattering state, as described by Eq. (2.9) (left), and an interaction between two πN scattering states, as described by Eq. (2.8) (right).

by a coupling strength $g_\alpha^{B_0}$. This interaction is labelled g, given by

$$g = \sum_{B_0} \sum_{\alpha} \int d^3k \left\{ |B_0\rangle\, G_\alpha^{B_0}(\boldsymbol{k})\, \langle \alpha(\boldsymbol{k})| + |\alpha(\boldsymbol{k})\rangle\, G_\alpha^{B_0\,\dagger}(\boldsymbol{k})\, \langle B_0| \right\} . \tag{2.9}$$

The $\boldsymbol{k}$-dependence of this type of interaction is typically chosen such that it reproduces established results from chiral perturbation theory (χPT). An example for this interaction is illustrated in the left-most diagram of Fig. 2.2, where a bare Δ_0 state is dressed by an interaction with a πN two-particle state. The full interaction Hamiltonian is therefore given by

$$H_{\mathrm{I}} = g + v\,. \tag{2.10}$$

2.2.1 Finite-Range Regularisation in HEFT

As can be seen in Sec. 2.2, the Hamiltonian is described by integrals over all momentum space, giving rise to ultraviolet divergences. To move to a finite Hilbert space, a regularisation scheme is required, and by choice of finite-range regularisation, we may make a connection between χEFT and the description of the bare baryon from Sec. 2.1.

To best phenomenologically represent the source of the interactions, we will primarily consider smooth regulators, such as a dipole regulator of the form

$$u(k, \Lambda) = \frac{1}{\left(1 + \frac{k^2}{\Lambda^2}\right)^2}\,, \tag{2.11}$$

and a Gaussian regulator of the form

$$u(k, \Lambda) = \exp\left(-\frac{k^2}{\Lambda^2}\right)\,. \tag{2.12}$$

We utilise these finite-range regulators in the potentials which parametrise the interactions g and v from Sec. 2.2, removing ultraviolet divergences and giving the interactions a finite range. As such, future references to $G_\alpha^{B_0}(\boldsymbol{k})$ will implicitly include a factor of $u(\boldsymbol{k}, \Lambda)$, while future references to $V_{\alpha\beta}(\boldsymbol{k}, \boldsymbol{k}')$ will implicitly include a factor of $u(\boldsymbol{k}, \Lambda)u(\boldsymbol{k}', \Lambda)$. In general, Λ may not necessarily be the same for each interaction. In this case, the regulator parameter for a the potential $G_\alpha^{B_0}(\boldsymbol{k})$ will be labelled $\Lambda_\alpha^{B_0}$, while the regulator parameters for the incoming and outgoing scattering channels of $v_{\alpha\beta}(\boldsymbol{k},\boldsymbol{k}')$ will be labelled $\Lambda_{v,\alpha}$ and $\Lambda_{v,\beta}$.

As previously described in Sec. 2.1, in χEFT the functional form of the regulator is irrelevant within the power-counting regime (PCR), while outside of the PCR, the regulator provides a model for the large quark mass description. Within HEFT, an investigation into the effects of both the choice of form factor and regulator parameters Λ are presented in Chapter 3.

2.2.2 Renormalisation of the Coupling

In determining the strength of the potential terms g and v as described in Sec. 2.2, the summation of self-energy terms at all orders in the process of solving the scattering equations for the system renormalises the coupling strengths, moving away from SU(3) flavour couplings as would be considered in χPT. Consider a system with a single bare basis state, dressed by loop-integral contributions from scattering states with self-energy $\Sigma(E)$. From Ref. [42], the full propagator $A(E)$ takes the form

$$A(E) = \frac{1}{E - m_{B_0} - \Sigma(E)}\,. \tag{2.13}$$

The self-energies $\Sigma(E)$ are taken such that $A(E)$ contains a pole associated with the resonance of interest, or rather such that there is some complex energy m with a negative imaginary component such that $m = m_{B_0} - \Sigma(m)$. As we are interested in studying the properties of resonances, we consider only self-energy diagrams which have a dominant contribution to the region about the resonance, and as such the propagator may be written as

$$\begin{aligned} A(E)^{-1} &= E - m - \{\Sigma(E) - \Sigma(m)\}\,, \\ &= (E-m)\left\{1 - \frac{\Sigma(E)-\Sigma(m)}{E-m}\right\}\,. \end{aligned} \tag{2.14}$$

Expanding about $E = m$, we have

$$\begin{aligned} A(E)^{-1} &= (E-m)\left\{1 - \Sigma'(m) - \frac{\Sigma^{\mathrm{R}}(E)}{E-m}\right\}\,, \\ &= (E-m)\left\{1 - \Sigma'(m)\right\} - \Sigma^{\mathrm{R}}(E)\,, \end{aligned} \tag{2.15}$$

where $\Sigma'(m)$ is the first derivative of $\Sigma(E)$ evaluated for $E = m$, and we define the term $\Sigma^{\mathrm{R}}(E)$ such that it contains all higher-order contributions to the self-energy, with $\Sigma^{\mathrm{R}}(m) = 0$. Based on this expression, we define the renormalised self-energy

$$\tilde{\Sigma}(E) = \left\{1 - \Sigma'(m)\right\}^{-1}\, \Sigma^{R}(E)\,. \tag{2.16}$$

Rewriting the propagator in terms of the renormalised self-energy,

$$A(E) = \frac{\{1 - \Sigma'(m)\}^{-1}}{E - m - \tilde{\Sigma}(E)} \tag{2.17}$$

reveals a propagator with a similar form as that of Eq. (2.13), though now in terms of the pole position m rather than the unphysical bare mass m_{B_0}. Here we see that both the propagator $A(E)$ and the self-energy diagrams have been renormalised by a factor of $\{1 - \Sigma'(m)\}^{-1}$. As this factor is constant for a given regulator, it may be absorbed into the interaction coupling constants within the self-energy contributions, and thus the coupling is considered to have been renormalised in the vicinity of the resonance.

2.3 Infinite-Volume Scattering

In order to constrain the Hamiltonian, there are several sources of information. The scale of the finite-range regulator has considerable impact on both the masses of the bare basis states, and the strengths of the interactions g and v, through the renormalisation process as defined in Sec. 2.2.2. The regulator parameters Λ can be considered phenomenological representations of the size of these bare states. One method for constraining the Hamiltonian is to calculate scattering observables such as cross sections, phase shifts, and inelasticities. In particular, these quantities may be calculated for each partial wave, allowing one to study particular resonances which are only produced in certain partial wave interactions. These may then be compared to scattering data available from hadron-hadron scattering experiments, giving the Hamiltonian a strong grounding in experimental data.

2.3.1 Coupled-Channel Scattering

For each partial wave, the scattering observables are readily obtained from the T-matrix, which may be solved from the coupled-channel scattering equations, which are a reduced form of the Bethe-Salpeter equations. As this thesis considers only meson-baryon scattering, for clarity we will consider only meson-baryon scattering states, where for a scattering state $|\alpha(k)\rangle$, the constituent particles are labelled $\alpha_{\rm M}$ and $\alpha_{\rm B}$ representing the meson and baryon respectively, with masses $m_{\alpha_{\rm M}}$ and $m_{\alpha_{\rm B}}$, and energies $\omega_{\alpha_{\rm M}}(k) = \sqrt{k^2 + m_{\alpha_{\rm M}}}$ and $\omega_{\alpha_{\rm B}}(k) = \sqrt{k^2 + m_{\alpha_{\rm B}}}$. In general, this formalism is largely unchanged for meson-meson scattering, though scattering such as $\pi\pi$ scattering would be considerably simplified, as the energy of such as state would simply be $\omega_{\pi\pi}(k) = 2\sqrt{k^2 + m_\pi^2}$. For interactions between two-particle states $|\alpha(k)\rangle$ and $|\beta(k')\rangle$, we choose only separable potentials $V_{\alpha\beta}(k, k')$ to describe the strength of this interaction. The simplest form of a separable potential is one in which the incoming and outgoing momentum are separable, and may be written in the form

$$V_{\alpha\beta}(k, k') = v_{\alpha\beta}\, f_\alpha(k)\, f_\beta(k')\,, \tag{2.18}$$

for some phenomenologically motivated form factor $f(k)$, and coupling constant $v_{\alpha\beta}$. The concept of a separable potential may be generalised to what we define as an n_f-separable potential, a potential which may be written in matrix form (with no sum over α and β) as

$$\begin{aligned} V_{\alpha\beta}(k,k') &= \boldsymbol{f}_\alpha^{\mathrm{T}}(k)\,\tilde{v}_{\alpha\beta}\,\boldsymbol{f}_\beta(k')\,, \\ &= \begin{pmatrix} f_\alpha^1(k) & \cdots & f_\alpha^{n_f}(k) \end{pmatrix} \begin{pmatrix} v_{\alpha\beta}^{1,1} & \cdots & v_{\alpha\beta}^{1,n_f} \\ \vdots & \ddots & \vdots \\ v_{\alpha\beta}^{n_f,1} & \cdots & v_{\alpha\beta}^{n_f,n_f} \end{pmatrix} \begin{pmatrix} f_\beta^1(k') \\ \vdots \\ f_\beta^{n_f}(k')\,. \end{pmatrix}\,. \end{aligned} \tag{2.19}$$

where $\boldsymbol{f}_\alpha(k)$ is a length n_f vector of functions $f_\alpha^i(k)$ for channel α, and $\tilde{v}_{\alpha\beta}$ is an $n_f \times n_f$ matrix containing coupling strengths $v_{\alpha\beta}^{ij}$. As an example, consider the potential derived from the Weinberg-Tomozawa term [43],

$$V_{\alpha\beta}(k,k') = v_{\alpha\beta}\,\frac{\omega_{\alpha_{\mathrm{M}}}(k) + \omega_{\beta_{\mathrm{M}}}(k')}{\sqrt{2\omega_{\alpha_{\mathrm{M}}}(k)}\,\sqrt{2\omega_{\beta_{\mathrm{M}}}(k')}}\,u(k)\,u(k')\,, \tag{2.20}$$

with finite-range regulator $u(k)$. This potential has the matrix form

$$V_{\alpha\beta}(k,k') = \begin{pmatrix} \frac{\omega_{\alpha_{\mathrm{M}}}(k)\,u(k)}{\sqrt{2\omega_{\alpha_{\mathrm{M}}}(k)}} & \frac{u(k)}{\sqrt{2\omega_{\alpha_{\mathrm{M}}}(k)}} \end{pmatrix} \begin{pmatrix} 0 & v_{\alpha\beta} \\ v_{\alpha\beta} & 0 \end{pmatrix} \begin{pmatrix} \frac{\omega_{\beta_{\mathrm{M}}}(k')\,u(k')}{\sqrt{2\omega_{\beta_{\mathrm{M}}}(k')}} \\ \frac{u(k')}{\sqrt{2\omega_{\beta_{\mathrm{M}}}(k')}} \end{pmatrix}\,, \tag{2.21}$$

clearly indicating that in this notation, may be considered a 2-separable potential.

With this definition of an n_f-separable potential, consider a system of n_b bare basis states, and n_c two-particle basis states, with Hamiltonian as defined in Sec. 2.2. The set of coupled-channel scattering equations for this system takes the form

$$T_{\alpha\beta}(k,k';E) = \tilde{V}_{\alpha\beta}(k,k';E) + \sum_\gamma \int dq\,q^2\,\frac{\tilde{V}_{\alpha\gamma}(k,q;E)\,T_{\gamma\beta}(q,k';E)}{E - \omega_\gamma + i\varepsilon}\,, \tag{2.22}$$

where γ sums over the n_c meson-baryon scattering channels considered. Here, we have also defined the coupled-channel potential, which includes both contributions from bare-scattering state interactions and background interactions. This takes the form

$$\tilde{V}_{\alpha\beta}(k,k';E) = \sum_{B_0} \frac{G_\alpha^{B_0}(k)\,G_\beta^{B_0}(k')}{E - m_{B_0}^{(0)}} + V_{\alpha\beta}(k,k')\,, \tag{2.23}$$

where the sum over B_0 considers all n_b bare states. This potential is represented diagrammatically in Fig. 2.3.

In general, the scattering equations as defined in Eq. (2.22) cannot be solved analytically, however we may proceed by first considering only the T-matrix associated with interactions between two-particle scattering states, and then adding on contributions from explicit poles associated with each bare state. This is done by first setting all couplings $g_\alpha^{B_0}$ to zero, effectively removing the contributions from bare basis states. The remaining

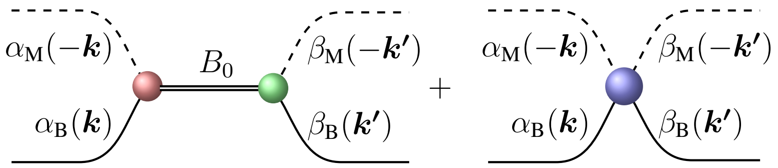

Figure 2.3: Diagrammatic representation of the coupled-channel potential $\tilde{V}_{\alpha\beta}(k,k';E)$. The red and green vertices correspond with the interactions $G_\alpha^{B_0}(k)$ and $G_\beta^{B_0}(k')$, while the blue vertex corresponds with $V_{\alpha\beta}(k,k')$.

T-matrix is denoted the background t-matrix, $t_{\alpha\beta}(k,k';E)$, and may be found as solutions of

$$t_{\alpha\beta}(k,k';E) = V_{\alpha\beta}(k,k') + \sum_\gamma \int dq\, q^2 \, \frac{V_{\alpha\gamma}(k,q)\, t_{\gamma\beta}(q,k';E)}{E - \omega_\gamma + i\varepsilon} \,. \tag{2.24}$$

Here, we emphasise the use of the original two-particle potential $V_{\alpha\beta}(k,k')$, rather than the coupled-channel potential $\tilde{V}_{\alpha\beta}(k,k';E)$. As we are considering only n_f separable potentials $V_{\alpha\beta}(k,k')$, the background t-matrix is also separable in momentum [44], and may therefore be written as

$$t_{\alpha\beta}(k,k';E) = \begin{pmatrix} f_\alpha^1(k) & \cdots & f_\alpha^{n_f}(k) \end{pmatrix} \begin{pmatrix} \tilde{t}_{\alpha\beta}^{1,1}(E) & \cdots & \tilde{t}_{\alpha\beta}^{1,n_f} \\ \vdots & \ddots & \vdots \\ \tilde{t}_{\alpha\beta}^{n_f,1}(E) & \cdots & \tilde{t}_{\alpha\beta}^{n_f,n_f}(E) \end{pmatrix} \begin{pmatrix} f_\beta^1(k') \\ \vdots \\ f_\beta^{n_f}(k')\,. \end{pmatrix} ,$$
$$\implies t_{\alpha\beta}(k,k';E) = \boldsymbol{f}_\alpha^{\rm T}(k)\, \tilde{t}_{\alpha\beta}(E)\, \boldsymbol{f}_\beta(k') \,. \tag{2.25}$$

We may substitute both this separable form of the t-matrix and the separable form of the potential from Eq. (2.19) into Eq. (2.24), giving

$$\begin{aligned} \boldsymbol{f}_\alpha^{\rm T}(k)\, \tilde{t}_{\alpha\beta}(E)\, \boldsymbol{f}_\beta(k') &= \boldsymbol{f}_\alpha^{\rm T}(k)\, \tilde{v}_{\alpha\beta}\, \boldsymbol{f}_\beta(k') \\ &\quad + \sum_\gamma \int dq\, q^2 \, \frac{\boldsymbol{f}_\alpha^{\rm T}(k)\, \tilde{v}_{\alpha\gamma}\, \boldsymbol{f}_\gamma(q)\, \boldsymbol{f}_\gamma^{\rm T}(q)\, \tilde{t}_{\gamma\beta}(E)\, \boldsymbol{f}_\beta(k')}{E - \omega_\gamma + i\varepsilon} \,, \end{aligned} \tag{2.26}$$

Pre-multiplying by $\boldsymbol{f}_\alpha(k)^{-1}$, and post-multiplying by $\boldsymbol{f}_\beta^{\rm T}(k)^{-1}$ (where $\boldsymbol{f}_\alpha(k)^{-1}\boldsymbol{f}_\alpha^{\rm T}(k) = 1$), this expression simplifies to

$$\tilde{t}_{\alpha\beta}(E) = \tilde{v}_{\alpha\beta} + \sum_\gamma \int dq\, q^2 \, \frac{\tilde{v}_{\alpha\gamma}\, \boldsymbol{f}_\gamma(q)\, \boldsymbol{f}_\gamma^{\rm T}(q)\, \tilde{t}_{\gamma\beta}(E)}{E - \omega_\gamma + i\varepsilon} \,. \tag{2.27}$$

Rewriting in index notation, where Greek indices specify the n_c scattering channels, and Latin indices specify the n_f elements of function-space,

$$\tilde{t}^{ij}_{\alpha\beta}(E) = v^{ij}_{\alpha\beta} + \sum_{\gamma} \sum_{m,n=1}^{n_f} v^{im}_{\alpha\gamma} \int dq\, q^2\, \frac{f^m_\gamma(q)\, f^n_\gamma(q)}{E - \omega_\gamma + i\varepsilon}\, \tilde{t}^{nj}_{\gamma\beta}(E)\,, \tag{2.28}$$

$$= v^{ij}_{\alpha\beta} + \sum_{\gamma} \sum_{m,n=1}^{n_f} v^{im}_{\alpha\gamma}\, M^{mn}_\gamma(E)\, \tilde{t}^{nj}_{\gamma\beta}(E)\,. \tag{2.29}$$

Defining the integrals

$$M^{ij}_\gamma(E) = \int dq\, q^2\, \frac{f^i_\gamma(q)\, f^j_\gamma(q)}{E - \omega_\gamma + i\varepsilon}\,, \tag{2.30}$$

and rewriting in matrix form in channel-space, solving for $\tilde{t}(E)$ gives

$$\tilde{t}^{ij}(E) = \left(1 - v^{ij}\, M^{ij}(E)\right)^{-1} v^{ij}\,. \tag{2.31}$$

Here, $M^{ij}(E)$ is an $n_c \times n_c$ diagonal matrix, where the diagonal entries are given by $M^{ij}_\gamma(E)$ for each channel γ. Having found this matrix expression for $\tilde{t}^{ij}(E)$, the full background t-matrix may therefore be re-constructed as

$$\begin{aligned} t_{\alpha\beta}(k,k';E) &= f^i_\alpha(k)\, \tilde{t}^{ij}_{\alpha\beta}(E)\, f^j_\beta(k')\,, \\ &= \boldsymbol{f}^{\mathrm{T}}_\alpha(k)\, \tilde{t}_{\alpha\beta}(E)\, \boldsymbol{f}_\beta(k')\,. \end{aligned} \tag{2.32}$$

It is worth noting that for a system with no bare basis states, such as a system where one is considering only purely dynamically-generated resonances, this expression is in fact the full T-matrix, giving

$$T_{\alpha\beta}(k,k';E) = t_{\alpha\beta}(k,k';E)\,. \tag{2.33}$$

For a system containing one or more bare basis states, the full T-matrix can be constructed by adding the contributions from said bare states,

$$T_{\alpha\beta}(k,k';E) = t_{\alpha\beta}(k,k',E) + T^{\text{bare}}_{\alpha\beta}(k,k';E)\,. \tag{2.34}$$

Inserting the forms of the full T-matrix from Eq. (2.22) and background t-matrix from Eq. (2.24), we may solve for $T^{\text{bare}}_{\alpha\beta}(k,k';E)$ as

$$T^{\text{bare}}_{\alpha\beta}(k,k';E) = \sum_{B_0,B_0'} \mathcal{G}^{B_0}_\alpha(k;E)\, A_{B_0,B_0'}(E)\, \mathcal{G}^{B_0'\,\dagger}_\beta(k';E)\,. \tag{2.35}$$

The process for deriving this expression is given in Appendix A.

Here we have defined two new expressions associated with the bare basis states. For a system with only interactions between bare states and scattering states, and no background interactions, we simply have $\mathcal{G}^{B_0}_\alpha(k;E) = G^{B_0}_\alpha(k)$, independent of the on-shell energy E. In the more general case, $\mathcal{G}^{B_0}_\alpha(k;E)$ is a modified potential describing how the bare states are dressed by the background interactions, denoted as the “dressed potential” in this text, and found as solutions of the integral equation

$$\mathcal{G}_\alpha^{B_0}(k;E) = G_\alpha^{B_0}(k) + \sum_\gamma \int dq\, q^2\, \frac{V_{\alpha\gamma}(k,q)\, \mathcal{G}_\gamma^{B_0}(q;E)}{E - \omega_\gamma(q) + i\varepsilon} \,. \tag{2.36}$$

However, this dressed potential is defined such that

$$\frac{V_{\alpha\beta}(k,k')\, \mathcal{G}_\beta^{B_0}(k';E)}{E - \omega_\beta(k) + i\varepsilon} = \frac{t_{\alpha\beta}(k,k';E)\, G_\beta^{B_0}(k')}{E - \omega_\beta(k) + i\varepsilon} \,. \tag{2.37}$$

Substituting this property into Eq. (2.36), we have

$$\mathcal{G}_\alpha^{B_0}(k;E) = G_\alpha^{B_0}(k) + \sum_\gamma \int dq\, q^2\, \frac{t_{\alpha\gamma}(k,q;E)\, G_\gamma^{B_0}(q)}{E - \omega_\gamma(q) + i\varepsilon} \,. \tag{2.38}$$

Using the separable nature of the background t-matrix,

$$\mathcal{G}_\alpha^{B_0}(k;E) = G_\alpha^{B_0}(k) + \sum_\gamma \sum_{i=1}^{n_f} \int dq\, q^2\, \frac{f_\alpha^i(k)\, \tilde{t}_{\alpha\gamma}(E)\, f_\gamma^i(q)\, G_\gamma^{B_0}(q)}{E - \omega_\gamma(q) + i\varepsilon} \,. \tag{2.39}$$

This can be further simplified by defining the integral

$$g_{f,\gamma,B_0}^i(E) = \int dq\, q^2\, \frac{f_\gamma^i(q)\, G_\gamma^{B_0}(q)}{E - \omega_\gamma(q) + i\varepsilon} \,, \tag{2.40}$$

and therefore the dressed potential is given by

$$\mathcal{G}_\alpha^{B_0}(k;E) = G_\alpha^{B_0}(k) + \sum_\gamma \sum_{i=1}^{n_f} f_\alpha^i(k)\, \tilde{t}_{\alpha\gamma}(E)\, g_{f,\gamma,B_0}^i(E) \,. \tag{2.41}$$

Similarly, we have that for ${\mathcal{G}_\alpha^{B_0}}^\dagger(k;E)$,

$$\frac{\mathcal{G}_\alpha^{B_0}(k;E)^\dagger\, V_{\alpha\beta}(k,k')}{E - \omega_\alpha(k) + i\varepsilon} = \frac{G_\alpha^{B_0}(k)\, t_{\alpha\beta}(k,k';E)}{E - \omega_\alpha(k) + i\varepsilon} \,. \tag{2.42}$$

Following a similar process, we find that $\mathcal{G}_\alpha^{B_0}(k;E) = {\mathcal{G}_\alpha^{B_0}}^\dagger(k;E)$.

Within Eq. (2.34), to calculate the bare state contribution to the T-matrix, we require the matrix of dressed bare states,

$$A_{B_0,B_0'}(E) = \left[\delta_{B_0,B_0'}\,(E - m_{B_0}) - \Sigma_{B_0,B_0'}(E) - \Sigma_{B_0,B_0'}^{\mathrm{I}}(E)\right]^{-1} \,. \tag{2.43}$$

For a single bare state, this takes the form of a simple propagator, as in Sec. 2.2.2. For a system with multiple bare basis states, this matrix describes the complex interplay between bare basis states interacting through intermediary scattering state loops. Within this matrix, $\Sigma_{B_0,B_0'}(E)$ describes the self-energy associated with loop integrals generated purely from the interaction between a bare state and a scattering state, governed by the interaction strength $G_\alpha^{B_0}(k)$. This self-energy is given by

$$\Sigma_{B_0,B_0'}(E) = \sum_\gamma \Sigma_{\gamma,B_0,B_0'}(E) = \sum_\gamma \int dq\, q^2 \, \frac{G_\gamma^{B_0}(q)\, G_\gamma^{B_0'}(q)}{E - \omega_\gamma(q) + i\varepsilon} \,. \tag{2.44}$$

This integral, along with $M_\gamma^{ij}(E)$ from Eq. (2.30) and $g_{f,\alpha,B_0}(E)$ from Eq. (2.40) contain a pole at $E - \omega_\gamma(q) + i\varepsilon = 0$. As such, to evaluate these integrals, we may extract the contributions from the pole using Sokhotski's formula [45]. Given some function $f(x)$, which is continuous over the range $[a, b]$, with some $x_0 \in [a, b]$, Sokhotski's formula is given by

$$\int_a^b dx \, \frac{f(x)}{x - x_0 + i\varepsilon} = \mathcal{P} \int_a^b dx \, \frac{f(x)}{x - x_0} - i\pi\, f(x_0) \,. \tag{2.45}$$

Here, the notation $\mathcal{P} \int$ is used to denote that a Cauchy principle value integral should be taken, which is defined such that given a singularity at x_0,

$$\mathcal{P} \int_a^b dx \, \frac{f(x)}{x - x_0} = \lim_{\varepsilon \to 0^+} \left[\int_a^{x_0 - \varepsilon} dx \, \frac{f(x)}{x - x_0} + \int_{x_0 + \varepsilon}^b dx \, \frac{f(x)}{x - x_0} \right] \,. \tag{2.46}$$

These integrals may then be evaluated using standard numerical techniques, such as the Gaussian quadrature method.

The second category of self-energy is the background self-energy $\Sigma^{\mathrm{I}}_{B_0,B_0'}(E)$. Similarly, this self-energy describes the self-energy corrections to the bare state masses due to background interactions. This depends on the background t-matrix, and takes the form

$$\Sigma^{\mathrm{I}}_{B_0,B_0'}(E) = \sum_{\alpha,\beta} \sum_{i,j=1}^{n_f} g^i_{f,\alpha,B_0}(E)\, \tilde{t}^{ij}_{\alpha\beta}(E)\, g^j_{f,\beta,B_0'}(E) \,. \tag{2.47}$$

The derivation of this expression may be found in Appendix A. Given these self-energy contributions, the matrix of dressed bare states can be constructed. This matrix describes how the bare states are dressed by loop integrals, and higher-order interactions between different bare states. Having found this matrix, we are able to calculate the positions of any poles in the T-matrix, or extract scattering observables as described in Sec. 2.3.3.

2.3.2 Poles in the T-Matrix

As the T-matrix can be separated into two parts, given by Eq. (2.34), poles may be found in each component. To do so, we search for the complex energy E_{pole} of the on-shell channel α (e.g. $\alpha = \pi N$ for pion-Nucleon scattering), which takes the form

$$E_{\text{pole}} = \sqrt{k^2_{\alpha,\text{pole}} + m^2_{\alpha_{\mathrm{M}}}} + \sqrt{k^2_{\alpha,\text{pole}} + m^2_{\alpha_{\mathrm{B}}}} \,, \tag{2.48}$$

where we may solve for momentum $k_{\alpha,\text{pole}}$ associated with the pole,

$$k^2_{\alpha,\text{pole}} = \frac{E^2_{\text{pole}}}{4} + \frac{\left(m^2_{\alpha_\text{B}} - m^2_{\alpha_\text{M}}\right)}{4E^2_{\text{pole}}} - \frac{m^2_{\alpha_\text{B}} + m^2_{\alpha_\text{M}}}{2} \,. \tag{2.49}$$

Given this complex momentum, any poles associated with dynamically-generated resonances will be found such that

$$t_{\alpha\alpha}(k_{\alpha,\text{pole}}, k_{\alpha,\text{pole}}; E_{\text{pole}})^{-1} = 0 \,. \tag{2.50}$$

With $t_{\alpha\alpha}$ as defined in Eq. (2.31), this is equivalent to finding energies which satisfy

$$1 - v^{ij}\, M^{ij}(E_{\text{pole}}) = 0 \,. \tag{2.51}$$

Considering the component of the T-matrix associated with the bare state, given by the second term of Eq. (2.34), the positions of any poles are found as solutions of

$$\det\left[A_{B_0,B_0'}(E_{\text{pole}})^{-1}\right] = 0 \,. \tag{2.52}$$

For a system with a single bare state, this simplifies to finding zeroes in the denominator of the propagator, or rather complex energies which satisfy

$$A_{B_0}(E_{\text{pole}})^{-1} = E_{\text{pole}} - m_{B_0} - \Sigma_{B_0}(E_{\text{pole}}) - \Sigma^{\text{I}}_{B_0}(E_{\text{pole}}) = 0 \,. \tag{2.53}$$

2.3.3 Scattering Observables

Given both $A_{B_0,B_0'}(E)$ from Eq. (2.43), and the modified potential $\mathcal{G}^{B_0}_{\alpha}(k;E)$ from Eq. (2.41), we are now able to calculate the full T-matrix as defined in Eq. (2.34). Using the T-matrix, we can calculate a variety of scattering observables, beginning with the scattering cross-section. The cross-section $\sigma_{\alpha\beta}(E)$ describes the cross-section associated with a transition from channel α to channel β at some energy E, and is given by

$$\sigma_{\alpha\beta}(E) = \frac{4\pi\, k_{\alpha_\text{on}}}{E^2\, k_{\beta_\text{on}}}\, \omega_{\alpha_\text{M}}(k_{\alpha_\text{on}})\, \omega_{\alpha_\text{B}}(k_{\alpha_\text{on}})\, \omega_{\alpha_\text{M}}(k_{\alpha_\text{on}})\, \omega_{\alpha_\text{B}}(k_{\alpha_\text{on}})\, \left|T_{\alpha\beta}(k_{\alpha_\text{on}}, k_{\beta_\text{on}}; E)\right|^2 \,. \tag{2.54}$$

Here, we have defined the on-shell momentum k_{α_on}, which for on-shell energy E is the real solution of $E = \omega_{\alpha_\text{M}}(k_{\alpha_\text{on}}) + \omega_{\alpha_\text{B}}(k_{\alpha_\text{on}})$, and therefore

$$k^2_{\alpha_\text{on}} = \frac{E^2}{4} + \frac{\left(m^2_{\alpha_\text{B}} - m^2_{\alpha_\text{M}}\right)}{4E^2} - \frac{m^2_{\alpha_\text{B}} + m^2_{\alpha_\text{M}}}{2} \,. \tag{2.55}$$

Other scattering observables such as the phase shifts and inelasticities associated with the scattering process may be calculated from the unitary S-matrix. Given the density of states in channel α,

$$\rho_\alpha(E) = \frac{\omega_{\alpha_\text{M}(k_{\alpha_\text{on}})}\, \omega_{\alpha_\text{B}(k_{\alpha_\text{on}})}}{E}\, k_{\alpha_\text{on}} \,, \tag{2.56}$$

the S-matrix is parameterised in terms of the T-matrix as

$$S_{\alpha\beta}(E) = \delta_{\alpha\beta} - 2\pi i \sqrt{\rho_\alpha(E)}\, T_{\alpha\beta}(k_{\alpha_{\text{on}}}, k_{\beta_{\text{on}}}; E)\sqrt{\rho_\beta(E)}\,. \tag{2.57}$$

Considering the on-shell channel α_{on}, which for this thesis will be either S-wave or P-wave pion-nucleon scattering, we label the phase shift associated with the transition from the on-shell channel to some channel β as $\delta_\beta(E)$, and the inelasticity associated with this scattering process as $\eta(E)$. These quantities are related to the S-matrix by the simple relation

$$S_{\alpha_{\text{on}}\beta}(E) = \eta(E)\, \exp\{2i\,\delta_\beta(E)\}\ . \tag{2.58}$$

Solving for these two scattering quantities, we therefore have that

$$\begin{aligned}\delta_\beta(E) &= \frac{1}{2}\ \text{atan}\left\{\frac{\text{Im}\, S_{\alpha_{\text{on}}\beta}(E)}{\text{Re}\, S_{\alpha_{\text{on}}\beta}(E)}\right\}\,,\\ \eta(E) &= |S_{\alpha_{\text{on}}\beta}(E)|\ .\end{aligned} \tag{2.59}$$

By comparing these scattering observables with those extracted from experimental scattering data, we are able to constrain the free parameters in the Hamiltonian.

2.4 Finite-Volume Hamiltonian

In lattice QCD, space-time is discretised to a four-dimensional lattice of points, with volume $V = L^3 \times L_t$, where L is the spatial extent of the lattice, and L_t is the temporal extent. Additionally, the boundary conditions for this lattice are typically taken to be periodic. Considering the Hamiltonian as constructed in Sec. 2.2, we may make a connection to lattice QCD results by formulating the Hamiltonian in a finite-volume L^3 with periodic boundary conditions.

2.4.1 Two-Particle Quantisation Condition

For such a system, in the centre-of-mass frame the momenta of the two particles are discretised according to

$$\boldsymbol{k_n} = \frac{2\pi}{L}\,\boldsymbol{n}\,, \qquad \boldsymbol{n} = (n_x, n_y, n_z) \in \mathbb{Z}^3\,. \tag{2.60}$$

In S-wave scattering, $\boldsymbol{n}$ is permitted to run over all integer values. However we require at least one unit of momentum to construct higher partial wave states, and in those cases $\boldsymbol{n} = \boldsymbol{0}$ is forbidden. In this frame, the energy of the two-particle system with back-to-back

Table 2.1: Degeneracy of momentum states in each type of shell. The degeneracy is obtained by considering the number of ways the entries can be permuted across the three dimensions, and allowing two signs for each momentum component. These momentum states are defined by integers $a, b, c \in \mathbb{N}\backslash\{0\}$, where $a \neq b \neq c$.

Shell	Degeneracy
$(0,0,0)$	1
$(a,0,0)$	6
$(a,a,0)$	12
(a,a,a)	8
$(a,b,0)$	24
(a,a,b)	24
(a,b,c)	48

momentum $\boldsymbol{k_n}$ will therefore be

$$E = \omega_{\alpha_\mathrm{M}}(\boldsymbol{k_n}) + \omega_{\alpha_\mathrm{B}}(-\boldsymbol{k_n}) = \sqrt{k_{\boldsymbol{n}}^2 + m_{\alpha_\mathrm{M}}^2} + \sqrt{k_{\boldsymbol{n}}^2 + m_{\alpha_\mathrm{B}}^2} \,. \tag{2.61}$$

With this momentum discretisation, integrals in the Hamiltonian such as those in Eq. (2.8) are similarly discretised, and therefore are transformed according to

$$4\pi \int dk\, k^2 = \int d^3k \to \sum_{\boldsymbol{n}\in\mathbb{Z}^3} \left(\frac{2\pi}{L}\right)^3 . \tag{2.62}$$

In a system with an exact rotational symmetry, integrals are often simplified by considering the degenerate momenta $k = |\boldsymbol{k}|$. In a finite-volume with discretised momentum we may make a similar simplification, where we consider degenerate momentum states

$$k_n = \frac{2\pi}{L}\sqrt{n} \,, \tag{2.63}$$

with $n = n_x^2 + n_y^2 + n_z^2$. In the finite volume of the lattice, we must consider the energy spectrum in representations of the cubic group O_h, and include the possible effects of angular momentum mixing. An extension of HEFT to include these partial wave mixing effects, including an isospin-2 $\pi\pi$ scattering example is presented in Ref. [31]. Fortunately, $l = 0$ and $l = 1$ scattering potentials map on to single cubic group irreps with $\mathbf{0}^+ = \mathbf{A}_1^+$, and $\mathbf{1}^- = \mathbf{T}_1^-$ (as seen in Eq. (3.10) in Ref. [31]), and therefore we are able to proceed without these additional complications.

In the notation of Ref. [26], the momentum states of Eq. (2.63) exist on "shells", analogous to the spheres of constant momenta in a system with spherical symmetry. There are seven types of shells, as shown in Table 2.1, and these shells may be considered as representations of the octahedral symmetry group O_h, as described in Ref. [31]. Using these shell definitions we are able to calculate the total degeneracy of a momentum state k_n, which we label $C_3(n)$. This function describes the number of possible combinations of n_x^2, n_y^2 and n_z^2 which combine to produce n. For values of n such as $n = 1$ and $n = 2$, only one type of shell ($\boldsymbol{n} = (1,0,0)$ and $\boldsymbol{n} = (1,1,0)$) is able to construct each momentum state, and therefore $C_3(n)$ is equal to the degeneracy of each shell, giving $C_3(1) = 6$ and $C_3(2) = 12$. For values such as $n = 9$ however, the momentum state may be constructed by either the $\boldsymbol{n} = (2,2,1)$ or $\boldsymbol{n} = (3,0,0)$ shells, and therefore the degeneracy is given by $C_3(9) = 30$. States such as $n = 7$ are forbidden, as there is no combination of three squared integers which produce the shell, and therefore $C_3(7) = 0$. Using the function $C_3(n)$, we may reduce the three-dimensional sums over all $\boldsymbol{n} \in \mathbb{Z}^3$ to single-dimensional sums, giving

$$\sum_{\boldsymbol{n}\in\mathbb{Z}^3} \left(\frac{2\pi}{L}\right)^3 \to \sum_{n=0}^{\infty} \left(\frac{2\pi}{L}\right)^3 C_3(n)\,. \tag{2.64}$$

We re-emphasise that this sum over n only begins at $n = 0$ for S-wave scattering. In higher partial waves, we only consider sums from $n = 1$.

2.4.2 Finite-Volume Regularisation

In Sec. 2.1, the finite-range regulator $u(k, \Lambda)$ provides a mechanism to smoothly remove higher-momentum contributions from integrals over all k, preventing ultraviolet divergences. In a finite-volume, by choosing some minimum allowed value for the regulator, u_{min}, we may truncate the sum in Eq. (2.64), giving a finite Hamiltonian matrix. Giving this minimum regulator value, we therefore have a maximum allowed momentum k_{max} in the system, given as the solution of $u(k_{\text{max}}, \Lambda) = u_{\text{min}}$. Given this maximum momentum, we may solve for the size of the Hamiltonian matrix,

$$n_{\text{max}} = \left(\frac{k_{\text{max}} L}{2\pi}\right)^2 . \tag{2.65}$$

In choosing a value for u_{min}, we require that the maximum momentum k_{max} is sufficiently larger than the regulator mass Λ, such that increasing k_{max} any further does not alter the solutions of the Hamiltonian. Additionally, as the Hamiltonian has size $(n_{\text{max}} + n_{\text{bare}}) \times (n_{\text{max}} + n_{\text{bare}})$, we require n_{max} to be minimised to reduce computational requirements. The effect of varying u_{min} on the eigenvalues of the Hamiltonian for a single-channel P-wave πN scattering system as considered in Sec. 3.1 is shown in Fig. 2.4, where it was found that a regulator minimum of $u_{\text{min}} = 10^{-2}$ is able to sufficiently balance these two requirements.

2.4.3 Finite-Volume Interactions

In addition to the discretisation of the momenta of the system, the strength of the interactions between basis states of the Hamiltonian is also affected by the finite volume. To calculate the magnitude of these finite-volume effects on the potentials, consider a simple toy system with a single bare basis state $|B_0\rangle$, and a single two-particle state $|\alpha(k)\rangle$. in

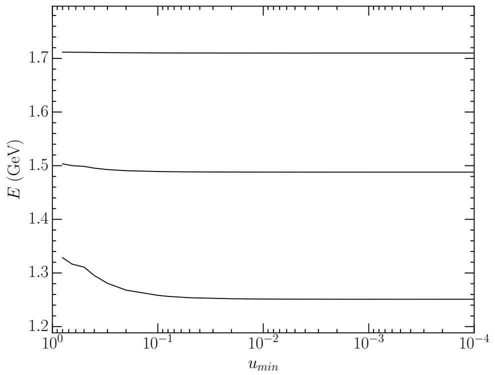

Figure 2.4: Dependence of Hamiltonian energy eigenvalues on $u_{\rm min}$ for the single-channel P-wave πN analysis as presented in Sec. 3.1, governing the maximum allowed momentum and therefore the size of the finite-volume Hamiltonian matrix.

particular, the only allowed interaction for this system is between the bare state and the two-particle state (equivalently, $v_{\alpha\alpha} = 0$), and we label this interaction strength $G_\alpha(k)$ in an infinite volume. A scenario such as this is analogous to leading order one-loop calculations in χPT.

In a finite volume, we label the interaction strength between the bare basis state and the scattering state $\overline{G}_\alpha(k)$. A matrix Hamiltonian for the system would take the form

$$H^{\rm fin} = \begin{pmatrix} m_{B_0} & \overline{G}_\alpha(k_1) & \overline{G}_\alpha(k_2) & \cdots \\ \overline{G}_\alpha(k_1) & \omega_\alpha(k_1) & 0 & \cdots \\ \overline{G}_\alpha(k_2) & 0 & \omega_\alpha(k_2) & \ddots \\ \vdots & \vdots & \ddots & \ddots \end{pmatrix} . \tag{2.66}$$

As this matrix is mostly sparse, we can algebraically solve the eigenvalue equation $\left|H^{\rm fin} - E_i\,\mathbb{I}\right| = 0$, giving energy eigenvalues

$$E_i = m_{B_0}^{(0)} - \sum_n \frac{\overline{G}_\alpha^2(k_n)}{\omega_\alpha(k_n) - E_i} . \tag{2.67}$$

By considering the relationship between energy eigenvalues of the finite-volume Hamiltonian as defined here, and poles in the infinite-volume S-matrix, we are able to find the relationship between $G_\alpha(k)$ and $\overline{G}_\alpha(k)$. For the toy system considered in this section, due to the absence of any two-particle scattering state interactions the coupled-channel potential as defined in Eq. (2.23) takes the simplified form

$$\tilde{V}(k,k';E) = \frac{G_\alpha(k)\,G_\alpha(k')}{E - m_{B_0}^{(0)}} . \tag{2.68}$$

Due to this, the T-matrix may be written in the simple separable form

$$T(k,k';E)=G_\alpha(k)\,t(E)\,G_\alpha(k')\,. \tag{2.69}$$

Substituting these two equations into Eq. (2.22), we therefore have that the energy dependent portion of the T-matrix is given by

$$t(E)=\left[E-m_{B_0}^{(0)}-\int_0^\infty dq\,q^2\,\frac{G_\alpha^2(q)}{E-\omega_\alpha(q)+i\varepsilon}\right]^{-1}\,. \tag{2.70}$$

As shown in Eq. (2.57), the S-matrix is directly proportional to the T-matrix, and therefore the energy corresponding with a pole will be equal in both cases. Poles in the S-matrix are therefore solutions of

$$E=m_{B_0}^{(0)}-\int_0^\infty dq\,q^2\,\frac{G_\alpha^2(q)}{\omega_\alpha(q)-E+i\varepsilon}\,. \tag{2.71}$$

As described in Sec. 2.4.1, there is a well-defined transformation from an infinite-volume integral to a finite-volume sum, however this is defined for an integral over all $\boldsymbol{k}\in\mathbb{R}^3$. As we have a system spherically symmetric in momentum-space, we make the transformation

$$\int dq\,q^2\to\int dq\,q^2\int\frac{d\Omega}{4\pi}\to\int\frac{d^3q}{4\pi} \tag{2.72}$$

onto Eq. (2.71), giving

$$E=m_{B_0}^{(0)}-\int\frac{d^3q}{4\pi}\,\frac{G_\alpha^2(q)}{\omega_\alpha(q)-E+i\varepsilon}\,. \tag{2.73}$$

Moving to a finite-volume, and apply the subsequent finite-volume discretisations as described in Sec. 2.4.1 with $q\to k_n$, we find the position of any finite-volume poles to be given by

$$E=m_{B_0}^{(0)}-\sum_n\frac{C_3(n)}{4\pi}\left(\frac{2\pi}{L}\right)^3\frac{G_\alpha^2(k_n)}{\omega_\alpha(k_n)-E}\,. \tag{2.74}$$

Comparing this expression with the expression obtained for the finite-volume Hamiltonian eigenvalues from Eq. (2.67), it is clear that the relationship between the finite and infinite-volume interaction strengths is given by

$$\overline{G}_\alpha(k_n)=\sqrt{\frac{C_3(n)}{4\pi}}\left(\frac{2\pi}{L}\right)^{\frac{3}{2}}G_\alpha(k_n)\,. \tag{2.75}$$

Returning to the general forms of the interaction strengths, the finite-volume potentials are therefore given by

$$\overline{G}_\alpha^{B_0}(k_n) = \sqrt{\frac{C_3(n)}{4\pi}} \left(\frac{2\pi}{L}\right)^{\frac{3}{2}} G_\alpha^{B_0}(k_n)\,, \tag{2.76}$$

$$\overline{V}_{\alpha\beta}(k_n, k_m) = \sqrt{\frac{C_3(n)}{4\pi}}\sqrt{\frac{C_3(m)}{4\pi}} \left(\frac{2\pi}{L}\right)^{3} V_{\alpha\beta}(k_n, k_m)\,. \tag{2.77}$$

2.4.4 Finite Hamiltonian Matrix

Given the finite-volume factors for the interaction strengths, we are now able to express the Hamiltonian as defined in Sec. 2.2 as a finite matrix. Applying the finite-volume transformations with discretised momenta and inserting the finite-volume potentials, the components of the finite Hamiltonian are therefore

$$H_0^{\text{fin}} = \sum_{B_0} |B_o\rangle\, m_{B_0}^{(0)}\, \langle B_0| + \sum_n^{n_{\max}} \sum_\alpha |\alpha(\boldsymbol{k}_n)\rangle\, \omega_\alpha(\boldsymbol{k}_n)\, \langle \alpha(\boldsymbol{k}_n)|\ , \tag{2.78}$$

$$\bar{g} = \sum_n^{n_{\max}} \sum_{\alpha, B_0} \sqrt{\frac{C_3(n)}{4\pi}} \left(\frac{2\pi}{L}\right)^{\frac{3}{2}} \left\{ |B_0\rangle\, G_\alpha^{B_0}(\boldsymbol{k}_n)\, \langle \alpha(\boldsymbol{k}_n)| + |\alpha(\boldsymbol{k}_n)\rangle\, G_\alpha^{B_0\,\dagger}(\boldsymbol{k}_n)\, \langle B_0| \right\}\ , \tag{2.79}$$

$$\bar{v} = \sum_{n,m}^{n_{\max}} \sum_{\alpha,\beta} \sqrt{\frac{C_3(n)}{4\pi}}\sqrt{\frac{C_3(m)}{4\pi}} \left(\frac{2\pi}{L}\right)^{3} |\alpha(\boldsymbol{k}_n)\rangle\, V_{\alpha\beta}\, \langle \beta(\boldsymbol{k}_m)|\ , \tag{2.80}$$

where the summations over n and m initialise at either 0 for an S-wave scattering channel, or 1 for a higher partial-wave process. The full finite Hamiltonian is therefore given by

$$H^{\text{fin}} = H_0^{\text{fin}} + \bar{g} + \bar{v}\,. \tag{2.81}$$

As the Hamiltonian is discretised, with a finite extent, it is convenient to express it in matrix form. Considering n_b bare basis states, labelled B_1 to B_{n_b}, and n_c two-particle scattering channels, labelled α_1 to α_{n_c}, the free Hamiltonian is a diagonal matrix of the form

$$H_0^{\text{fin}} = \text{diag}\left(m_{B_1}^{(0)},\, \ldots,\, m_{B_{n_b}}^{(0)},\, \omega_{\alpha_1}(k_1),\, \omega_{\alpha_{n_c}}(k_1),\, \omega_{\alpha_1}(k_2),\, \ldots,\, \omega_{\alpha_{n_c}}(k_{\max})\right)\ , \tag{2.82}$$

where k_1 corresponds with either $k = 0$ or $k = 2\pi/L$ depending on which partial wave channel α_i is scattering in. Considering the finite-volume interaction $\bar{g}$, it is convenient to express it in a block matrix form. We therefore define the block matrix

$$\overline{G}(k_i) = \begin{pmatrix} \overline{G}^{B_1}_{\alpha_1}(k_i) & \overline{G}^{B_1}_{\alpha_2}(k_i) & \cdots & \overline{G}^{B_1}_{\alpha_{n_c}}(k_i) \\ \overline{G}^{B_2}_{\alpha_1}(k_i) & \overline{G}^{B_2}_{\alpha_2}(k_i) & \cdots & \overline{G}^{B_2}_{\alpha_{n_c}}(k_i) \\ \vdots & \vdots & \ddots & \vdots \\ \overline{G}^{B_{n_b}}_{\alpha_1}(k_i) & \overline{G}^{B_{n_b}}_{\alpha_2}(k_i) & \cdots & \overline{G}^{B_{n_b}}_{\alpha_{n_c}}(k_i) \end{pmatrix} . \tag{2.83}$$

Using this definition, $\bar{g}$ may be written as

$$\bar{g} = \begin{pmatrix} 0_{n_b\times n_b} & \overline{G}(k_1) & \overline{G}(k_2) & \overline{G}(k_3) & \cdots & \overline{G}(k_{\max}) \\ \overline{G}(k_1)^{\mathrm{T}} & 0 & 0 & 0 & \cdots & 0 \\ \overline{G}(k_2)^{\mathrm{T}} & 0 & 0 & 0 & \cdots & 0 \\ \overline{G}(k_3)^{\mathrm{T}} & 0 & 0 & 0 & \cdots & 0 \\ \vdots & \vdots & \vdots & \vdots & \ddots & 0 \\ \overline{G}(k_{\max})^{\mathrm{T}} & 0 & 0 & 0 & \cdots & 0 \end{pmatrix} . \tag{2.84}$$

Similarly, we may also represent the interaction $\bar{v}$ in a block matrix form, defining

$$\overline{V}(k_i, k_j) = \begin{pmatrix} \overline{V}_{\alpha_1\alpha_1}(k_i, k_j) & \overline{V}_{\alpha_1\alpha_2}(k_i, k_j) & \cdots & \overline{V}_{\alpha_1\alpha_{n_c}}(k_i, k_j) \\ \overline{V}_{\alpha_2\alpha_1}(k_i, k_j) & \overline{V}_{\alpha_2\alpha_2}(k_i, k_j) & \cdots & \overline{V}_{\alpha_2\alpha_{n_c}}(k_i, k_j) \\ \vdots & \vdots & \ddots & \vdots \\ \overline{V}_{\alpha_{n_c}\alpha_1}(k_i, k_j) & \overline{V}_{\alpha_{n_c}\alpha_2}(k_i, k_j) & \cdots & \overline{V}_{\alpha_{n_c}\alpha_{n_c}}(k_i, k_j) \end{pmatrix} . \tag{2.85}$$

Expressing $\bar{v}$ in terms of these block matrices, we have that

$$\bar{v} = \begin{pmatrix} 0_{n_b\times n_b} & \cdots & & & \\ \vdots & \overline{V}(k_1, k_1) & \overline{V}(k_1, k_2) & \cdots & \overline{V}(k_1, k_{\max}) \\ & \overline{V}(k_2, k_1) & \overline{V}(k_2, k_2) & \cdots & \overline{V}(k_2, k_{\max}) \\ & \vdots & \vdots & \ddots & \vdots \\ & \overline{V}(k_{\max}, k_1) & \overline{V}(k_{\max}, k_2) & \cdots & \overline{V}(k_{\max}, k_{\max}) \end{pmatrix} . \tag{2.86}$$

Using these matrix representations, the full finite Hamiltonian may therefore be calculated from Eq. (2.81). Expressing these components in this form proves to be particularly helpful for numerically constructing the Hamiltonian. As the Hamiltonian has been constructed in a finite matrix form, the allowed energies of the system may be calculated by solving the eigenvalue equation

$$\left| H^{\text{fin}} - E_i\,\mathbb{I} \right| = 0\,, \tag{2.87}$$

giving energy eigenvalues E_i. With the exception of a simple system such as the toy system constructed in Sec. 2.4.3, solving for the eigenvalues of the Hamiltonian matrix must be done numerically, using a real, symmetric eigenvalue solver such as the `syevd` routine found as part of the LAPACK [46] package.

A unique advantage of the HEFT formalism is the ability to also solve for the eigenvectors of the Hamiltonian. These eigenvectors are labelled $\langle B_j | E_i \rangle$. This describes the contribution from each basis state $|B_j\rangle$ to the energy eigenstate $|E_i\rangle$. By considering these eigenvectors, one can gain insight into the structure of finite-volume eigenstates, where the fractional contribution from each basis state to an eigenstate is given by $|\langle B_j | E_i \rangle|^2$.

2.4.5 Pion Mass Dependence

In order to reduce computational requirements, lattice QCD calculations have typically been performed at larger-than-physical pion masses. While contemporary calculations are able to be performed near or even below the physical point, a pion mass interpolation/extrapolation scheme is generally required to compare lattice QCD results with experimental results. To make connection to spectroscopic lattice QCD calculations using HEFT, we are able to extend the HEFT formalism to unphysical pion masses.

As the pion mass moves away from the physical point, labelled as $m_\pi|_{\text{phys}}$, we need to proportionally alter the masses of other hadrons. In particular, they should vary by m_π^2, which is typically taken as proportional the light quark mass ($m_q \sim m_\pi^2$). A meson with mass m_{M} is taken to vary according to

$$m_{\text{M}}^2(m_\pi^2) = m_{\text{M}}^2\big|_{\text{phys}} + \alpha_{\text{M}} \left(m_\pi^2 - m_\pi^2\big|_{\text{phys}} \right) . \tag{2.88}$$

The rate at which the meson mass varies, labelled α_{M}, is referred to as the *mass slope* of the meson in this thesis. As the strange quark mass is held fixed in the lattice QCD results considered, the mass slopes of the pseudoscalar mesons may be found by simply considering the light quark content of the meson. As an example, the slope for the kaon is $\alpha_K = 0.5$ GeV^{-1}.

The pion mass dependence for baryons with mass m_{B} is taken as the first term of the residual series expansion, giving

$$m_{\text{B}}(m_\pi^2) = m_{\text{B}}\big|_{\text{phys}} + \alpha_{\text{B}} \left(m_\pi^2 - m_\pi^2\big|_{\text{phys}} \right) . \tag{2.89}$$

To calculate the mass slopes for baryon states, we fit this functional form to ground state mass calculations from lattice QCD, such as those from Ref. [47]. In practice, this process correctly finds that baryons with a smaller light quark content have a lower mass slope.

While the pion mass dependence of ground state hadrons is well-understood due to the wealth of lattice QCD results, it is less clear how the mass of the bare basis states used in HEFT should vary with the light quark mass. As this thesis focuses on three-quark bare states however, we postulate them to take a linear dependence on the quark mass, giving

$$m_{B_0}(m_\pi^2) = m_{B_0}^{(0)} + \alpha_{B_0} \left(m_\pi^2 - m_\pi^2\big|_{\text{phys}} \right) . \tag{2.90}$$

Given that bare states correspond with quark-model states, we expect this form to be a good approximation for the pion mass dependence, given that a majority of the non-linearity in a physical state's pion mass extrapolation arises from self-energy interactions. In order to constrain the mass slopes for the bare states, we calculate the finite-volume energy spectrum at given pion masses and lattice sizes which correspond with lattice QCD calculations. We then vary the bare mass slopes such that HEFT eigenstates with large bare state eigenvector components correspond with lattice QCD eigenstates constructed from three-quark interpolating fields. This process will be explored further in Chapter 3 and Chapter 5.

While in principle one could also vary couplings which govern interaction strengths with pion mass, in HEFT the couplings are taken to be fixed as found at the physical point, following the convention of χPT where the couplings are fixed to their determination at the chiral limit. Given the mass slopes of all hadrons and bare basis states, we are able to extrapolate to unphysical pion masses and make connection with a wide range of lattice QCD results. In particular, by considering the eigenvector composition of HEFT eigenstates corresponding with lattice QCD eigenstates, we are able to make predictions about the structure of the lattice QCD states.

2.4.6 Correlation Functions

In this section we introduce a novel HEFT formalism for estimating scattering-state contaminations in lattice QCD correlation functions constructed with standard three-quark operators. The analysis draws on the extensive information available in the finite-volume eigenvectors of the Hamiltonian.

We commence with the consideration of a single bare basis state. Given a three-quark operator $\chi(\boldsymbol{x},t)$ with quantum numbers corresponding to a baryonic state of interest, the correlation function [48, 49] is given by

$$\begin{aligned} G_\chi(t,\boldsymbol{p}) &= \sum_{\boldsymbol{x}} e^{-i\boldsymbol{p}\cdot\boldsymbol{x}} \left\langle\overline{\Omega}\right| \chi(\boldsymbol{x},t)\,\overline{\chi}(0,0)\left|\Omega\right\rangle\,, \\ G_\chi(t) &= \sum_i \left|\langle\Omega|\,\chi\,|E_i\rangle\right|^2 e^{-E_i t}\,, \end{aligned} \tag{2.91}$$

where a complete set of energy eigenstates $\mathbb{I} = \sum_i |E_i\rangle\,\langle E_i|$ has been introduced, $|\Omega\rangle$ is the nontrivial QCD vacuum, and zero momentum has been taken.

In Ref. [50], Bär and coworkers provided a χPT estimate of the coupling between a smeared nucleon interpolating field and a non-interacting pion-nucleon basis state as

$$\frac{3}{16}\,\frac{1}{(f_\pi\,L)^2\,E_\pi\,L}\left(\frac{E_N-m_N}{E_N}\right) \approx 10^{-3}\,, \tag{2.92}$$

where E_π and E_N are on-shell pion and nucleon energies. The numerical estimate is based on a 3 fm lattice and the lowest nontrivial momentum contribution where the coupling is largest. Here the $1/L^3$ dependence of the coupling is manifest as the non-interacting two-particle momentum state is spread uniformly throughout the lattice volume.

Noting the small magnitude of the overlap between the local interpolating field and the two-particle basis states, one concludes that the state excited by the local interpolating field is the only local state in the Hamiltonian basis, the bare-baryon basis state. As such, we associate the three-quark nucleon interpolating field $\overline{\chi}$ acting on the nontrivial QCD vacuum, $|\Omega\rangle$, with the bare basis state of HEFT, via $\overline{\chi}(0)\,|\Omega\rangle = |B_0\rangle$. Inserting this into Eq. (2.91) gives

$$G_{B_0}(t) = \sum_i |\langle B_0|E_i\rangle|^2 \, e^{-E_i t} \,. \tag{2.93}$$

Drawing on the eigenvector components $\langle B_0|E_i\rangle$, and eigenenergies E_i of HEFT, we can simulate the scattering-state contaminations in lattice QCD correlation functions. We define the "contamination function" $C_{B_0}(t)$ for the bare basis state $|B_0\rangle$ as

$$C_{B_0}(t) = \frac{1}{G_{B_0}(t)} \sum_{i \neq B_0} |\langle B_0|E_i\rangle|^2 \, e^{-E_i t} \,, \tag{2.94}$$

where the sum over all $i \neq B_0$ is considering all energy eigenstates, barring the eigenstate with the largest contribution from the bare state. We label this eigenstate $|E_{B_0}\rangle$. If this eigenstate is the ground state, for sufficiently large Euclidean time evolution the contamination function will tend to zero, where all excited states have exponentially decayed through the Euclidean time evolution. If $|E_{B_0}\rangle$ is not the ground state, we expect a minimum in the contamination function at some Euclidean time, where the state has the least scattering-state contamination, before becoming completely dominated by the lowest-lying scattering state.

This construction of the correlation function and resultant contamination function is relatively straightforward for a system with a single bare basis state. The generalisation to two bare basis states is presented in Chapter 5 in the context of the two low-lying odd-parity nucleon resonances.

3

REGULARISATION IN HEFT

The content of this chapter is based upon the publication: Curtis D. Abell, Derek B. Leinweber, Anthony W. Thomas, and Jia-Jun Wu. Regularization in nonperturbative extensions of effective field theory. Phys. Rev. D,106(3):034506, 2022[34].

In chiral perturbation theory (χPT), it has been shown that within the power-counting regime (PCR) the chiral expansion of quantities of interest is independent of choice of regularisation scheme. Finite-range regularisation (FRR) is one such choice, where a smooth momentum regulator $u(k,\Lambda)$ is introduced to loop integrals, suppressing large momentum contributions, and thereby removing ultraviolet divergences. Within the PCR, the choice of regulator form factor, and regulator parameter Λ is irrelevant. However, outside of the PCR the regulator serves as a model, introducing Λ-dependent terms. This process is described in more detail in Sec. 2.1. In a non-perturbative extension of effective field theory, such as Hamiltonian Effective Field Theory (HEFT), the process of finite-range regularisation has a significant impact. As described in Sec. 2.2.2, the dimensionless coupling strengths are renormalised in some Λ-dependent manner to describe experimental data, and the mass of the bare basis state has a strong dependence on the regulator parameter. In line with the approach taken in χPT [51], we hold these couplings fixed as the pion mass is varied, instead varying the masses of the two-particle state hadrons and any bare state masses to describe physics away from the physical point.

While these quantities are Λ-dependent and therefore model dependent, as they are constrained by experimental scattering data it is expected that the observables should be model-independent. In practice however, to what degree this model-independence manifests in the Hamiltonian is unclear, and therefore in this section we will focus on exploring the effects of a varying regulator in both infinite and finite volume physics. In particular, the relationship between the regulator and the bare basis state will be explored, investigating the role of the regulator in describing the resonance as being dynamically generated, versus generated by a three-quark core dressed by meson-baryon interactions.

To study the effects of regularisation in HEFT, the P-wave $\Delta(1232)$ resonance with quantum numbers spin-$\frac{3}{2}$ and isospin-$\frac{3}{2}$ will be taken as a case study. This resonance is particularly suitable for an exploratory study, as it lies near the pion-nucleon threshold, and therefore is largely independent of contributions from three-particle $\pi\pi N$ and hyperon states.

In this chapter, we will begin by considering the effects of our choice of regulator parameter for a simple system with a single bare state and one πN scattering state. This will allow for a consideration of the effects of regularisation on both infinite-volume and finite-volume physics, without any complicated dynamics above the $\pi\Delta$ threshold. In addition, the effects of the choice of regulator itself will be considered. Following this, we will consider a more complex system, with an additional $\pi\Delta$ scattering channel. This will provide insight into how the coupled-channel formalism responds to a varying regulator parameter, and how we can use lattice QCD to find a preferred regulator parameter. We will also consider how this formalism compares to contemporary lattice QCD results, without any additional changes to the constraints of the Hamiltonian.

3.1 Single Channel Analysis

In order to study the effects of our choice of regulator form, and regulator parameter, a simple system is best considered first in order to gain intuition into the behaviour of the system under changes in the regulator. As such, we will first consider a system with one bare state, labelled $|\Delta_0\rangle$, with mass $H_0 |\Delta_0\rangle = m_{\Delta_0} |\Delta_0\rangle$. This bare state will then be dressed by a single scattering channel labelled $|\pi(\boldsymbol{k})N(-\boldsymbol{k})\rangle$. Due to the symmetries of the system however, we can consider this channel more simply as $|\pi N(k)\rangle$. The energy of this state is given by $H_0 |\pi N(k)\rangle = \omega_{\pi N}(k) |\pi N(k)\rangle$, where

$$\omega_{\pi N}(k) = \sqrt{k^2 + m_\pi^2} + \sqrt{k^2 + m_N^2} \,. \tag{3.1}$$

The interaction between the bare state and a πN scattering channel of momentum k is taken as the χPT-motivated form

$$G^{\Delta}_{\pi N}(k) = \frac{g^{\Delta}_{\pi N}}{m_\pi^{\text{phys}}} \frac{k}{\sqrt{\omega_\pi(k)}} \, u(k, \Lambda) \,. \tag{3.2}$$

Here, the coupling strength $g^{\Delta}_{\pi N}$ is made dimensionless by the pion mass at the physical point, $u(k, \Lambda)$ is the regulator of a form to be specified, $1/\sqrt{\omega_\pi(k)}$ is a kinematic factor, where $\omega_\pi(k) = \sqrt{k^2 + m_\pi^2}$, and the potential is proportional to a single power of k to represent the P-wave nature of the interaction.

Considering interactions between two scattering channels with back-to-back momenta k and k', this interaction is parameterised by the potential

$$V_{\pi N \pi N}(k, k') = \frac{v_{\pi N \pi N}}{(m_\pi^{\text{phys}})^2} \frac{k}{\omega_\pi(k)} \frac{k'}{\omega_\pi(k')} \, u(k, \Lambda) \, u(k', \Lambda) \,. \tag{3.3}$$

In the notation of Sec. 2.3, it can be seen that this potential is separable in the incoming and outgoing momentum, and can be written in the form

$$V_{\pi N \pi N}(k, k') = \frac{v_{\pi N \pi N}}{(m_\pi^{\text{phys}})^2} f_{\pi N}(k) \, f_{\pi N}(k') \,, \quad \text{with} \quad f_{\pi N}(k) = \frac{k}{\omega_\pi(k)} \, u(k, \Lambda) \,. \tag{3.4}$$

In general, these two types of interactions can have different ranges, and therefore different regulator parameters. To simplify the analysis, and allow for a better building of intuition into the role of the regulator, Λ will be held equal for both $G^{\Delta}_{\pi N}$ and $V_{\pi N \pi N}$. As a result, for a particular choice of Λ, this system has three free parameters: the bare mass m_{Δ_0}, and coupling strengths $g^{\Delta}_{\pi N}$ and $v_{\pi N \pi N}$. In order to constrain these parameters for a given Λ, we will consider experimental P-wave pion-nucleon scattering data.

3.1.1 Fitting Experimental Data

To initially verify the ability of this system to describe experimental data, we begin by considering a dipole regulator,

$$u(k) = \frac{1}{\left(1 + \frac{k^2}{\Lambda^2}\right)^2}\,, \tag{3.5}$$

where a regulator parameter of $\Lambda = 0.8$ GeV, associated with the induced pseudoscalar form factor of the nucleon[52], will be used. To make connection with pion-nucleon scattering data, we construct the scattering equations as formulated in Sec. 2.3 for this system. As we are working within a single-channel framework, rather than a coupled-channel framework, the coupled-channel scattering equations in Eq. (2.22) becomes

$$T_{\pi N \pi N}(k, k'; E) = \tilde{V}_{\pi N \pi N}(k, k'; E) + \int dq\, q^2\, \frac{\tilde{V}_{\pi N \pi N}(k, q; E)\, T_{\pi N \pi N}(q, k'; E)}{E - \omega_{\pi N}(q) + i\varepsilon}\,, \tag{3.6}$$

where the modified potential $\tilde{V}_{\pi N \pi N}$ is given by

$$\tilde{V}_{\pi N \pi N}(k, k'; E) = \frac{G^{\Delta}_{\pi N}(k)\, G^{\Delta}_{\pi N}(k')}{E - m_{\Delta_0}} + V_{\pi N \pi N}(k, k')\,. \tag{3.7}$$

Solving for this T-matrix with the techniques outlined in Sec. 2.3, we decompose the T-matrix into a background component, given by $t_{\pi N \pi N}$, and a bare state component, given by $t^{\Delta}_{\pi N \pi N}$. The background portion of the T-matrix is considerably simplified from the general description in Sec. 2.3, giving

$$t_{\pi N \pi N}(k, k'; E) = \frac{V_{\pi N \pi N}(k, k')}{(1 - v_{\pi N \pi N}\, M_{\pi N}(E))}\,, \tag{3.8}$$

where $M_{\pi N}(E)$ is an integral defined below. Additionally, the component of the T-matrix associated with the bare state is given by $t^{\Delta}_{\pi N \pi N} = \mathcal{G}^{\Delta}_{\pi N}(k; E)\, A(E)\, \mathcal{G}^{\Delta}_{\pi N}(k'; E)$, where the dressed potential is given by

$$\mathcal{G}^{\Delta}_{\pi N}(k) = G^{\Delta}_{\pi N}(k) + \frac{v_{\pi N \pi N}\, f_{\pi N}(k)}{1 - v_{\pi N \pi N}\, M_{\pi N}(E)}\, g_{f, \pi N, \Delta}(E)\,, \tag{3.9}$$

and the propagator is of the form

$$A(E) = \frac{1}{E - m_{\Delta_0} - \Sigma_{\pi N}(E) - \Sigma^{\mathrm{I}}_{\pi N}(E)}\,, \tag{3.10}$$

with $\Sigma^{\mathrm{I}}_{\pi N}(E)$ given by Eq. (2.47). Within this formulation, there are three integrals to be calculated numerically,

$$M_{\pi N}(E) = \int dq\, q^2\, \frac{f_{\pi N}(q)^2}{E - \omega_{\pi N}(q) + i\varepsilon}\,. \tag{3.11a}$$

$$g_{f,\pi N,\Delta}(E) = \int dq\, q^2\, \frac{f_{\pi N}(q)\, G^{\Delta}_{\pi N}(q)}{E - \omega_{\pi N}(q) + i\varepsilon}\,, \tag{3.11b}$$

$$\Sigma_{\pi N}(E) = \int dq\, q^2\, \frac{G^{\Delta}_{\pi N}(q)^2}{E - \omega_{\pi N}(q) + i\varepsilon}\,. \tag{3.11c}$$

As all three of these integrands contain a pole for $E - \omega_{\pi N}(q) + i\varepsilon = 0$, we are able to use Sokhotski's formula to rewrite them in terms of a principle value integral as described in Eq. (2.45), Taking Eq. (3.11a) as an example, the integral may therefore be rewritten as

$$\begin{aligned} M_{\pi N}(E) = \mathcal{P} \int dq\, q^2\, \frac{f_{\pi N}(q)^2}{E - \omega_{\pi N}(q)} \\ - i\pi \int dq\, q^2\, f_{\pi N}(q)^2\, \delta(E - \omega_{\pi N}(q))\,. \end{aligned} \tag{3.12}$$

Given the on-shell momentum k_{on}, which is the solution of $E = \omega_{\pi}(k_{\text{on}}) + \omega_N(k_{\text{on}})$, the delta function may be simplified using the property that

$$\delta(E - \omega_{\pi N}(q)) = \frac{1}{|\omega'_{\pi N}(q)|}\, \delta(k_{\text{on}} - q)\,, \tag{3.13}$$

where $\omega'_{\pi N}(q)$ represents the first derivative of $\omega_{\pi N}(q)$ with respect to q. As such, this integral may be evaluated as

$$M_{\pi N}(E) = \mathcal{P} \int dq\, q^2\, \frac{f_{\pi N}(q)^2}{E - \omega_{\pi N}(q)} - i\pi\, \frac{k_{\text{on}}^3\, f_{\pi N}(k_{\text{on}})^2}{E}\, \omega_{\pi}(k_{\text{on}})\, \omega_N(k_{\text{on}})\,. \tag{3.14}$$

A similar process may be used to also simplify the integrals $g_{f,\pi N,\Delta}(E)$ and $\Sigma_{\pi N}(E)$. In general, these principle value integrals may be evaluated numerically using standard Gaussian quadrature techniques, such as that offered by the `qawc` function in QUADPACK [53]. Given these integrals, the T-matrix may therefore be calculated as

$$T_{\pi N \pi N}(k, k'; E) = t_{\pi N \pi N}(k, k'; E) + t^{\Delta}_{\pi N \pi N}(k, k'; E)\,. \tag{3.15}$$

Table 3.1: Single-channel fit parameters constrained to the WI08 solution of the P_{33} πN scattering data [54, 55], where a dipole regulator with $\Lambda = 0.8$ GeV was used.

Parameter	Fit Value
m_{Δ_0}/ GeV	1.3589
$g^{\Delta}_{\pi N}$	0.1762
$v_{\pi N,\pi N}$	-0.0286
Λ/ GeV	0.8000
d.o.f	13
χ^2	236.81
χ^2/d.o.f.	18.22

Evaluating the T-matrix at the on-shell momentum k_{on}, we may solve for the S-matrix using the density of states as defined in Eq. (2.56), giving

$$S_{\pi N \pi N}(E) = 1 = 2\pi i \, \frac{k_{\text{on}}}{E} \, \omega_\pi(k_{\text{on}}) \, \omega_N(k_{\text{on}}) \, T_{\pi N \pi N}(k_{\text{on}}, k_{\text{on}}; E) \,. \tag{3.16}$$

From the S-matrix, the phase shift is therefore

$$\delta_{\pi N}(E) = \frac{1}{2} \, \text{atan} \left(\frac{\text{Im} \, S_{\pi N \pi N}(E)}{\text{Re} \, S_{\pi N \pi N}(E)} \right) \,. \tag{3.17}$$

By comparing this phase shift to experimental data, we are able to constrain the three free parameters in the Hamiltonian. Considering an energy range of $E = m_\pi + m_N$ to the $\pi\Delta$ threshold at approximately $E = 1.35$ GeV, we vary the bare mass m_{Δ_0}, and the coupling strengths $g^{\Delta}_{\pi N}$ and $v_{\pi N \pi N}$, and compare to P_{33} pion-nucleon scattering data available from Refs. [54] and [55], specifically the WI08 solution. In order to fit this data, a variety of minimisation methods were considered, though it was found that Powell's derivative-free optimisation method [56] was best performing. As each function evaluation requires several numerical integrals at each energy value, a single function evaluation is relatively expensive. Therefore, a derivative-free method which doesn't need to calculate the Jacobian requires significantly less computational time.

The phase shifts predicted by HEFT can be compared to the scattering data by a simple χ^2 test. Given the choice of a dipole regulator with Λ = 0.8 GeV, the resultant best fit parameters are presented in Table 3.1. Additionally, the phase shift produced by this set of fit parameters is illustrated in Fig. 3.1. A χ^2 of 236.81 was found for this fit, with a χ^2/d.o.f. of 18.22. While it appears surprising that the χ^2/d.o.f. is so high, the πN data used for fitting was taken from the single-energy WI08 solution, which has a very large degree of statistical precision. However, there is a degree of systematic uncertainty not present in the statistical error bars shown in Fig. 3.1. As such, many authors either do not report a χ^2, or assign some relative error instead. As an example, Meissner *et. al.* assign a 3% error to their data, quoting a χ^2/d.o.f. of 0.77 for a fit range of up to 1.2 GeV. Similarly, in Ref. [57] a 5% error is assigned providing a χ^2/d.o.f. of 0.78 when fitting up

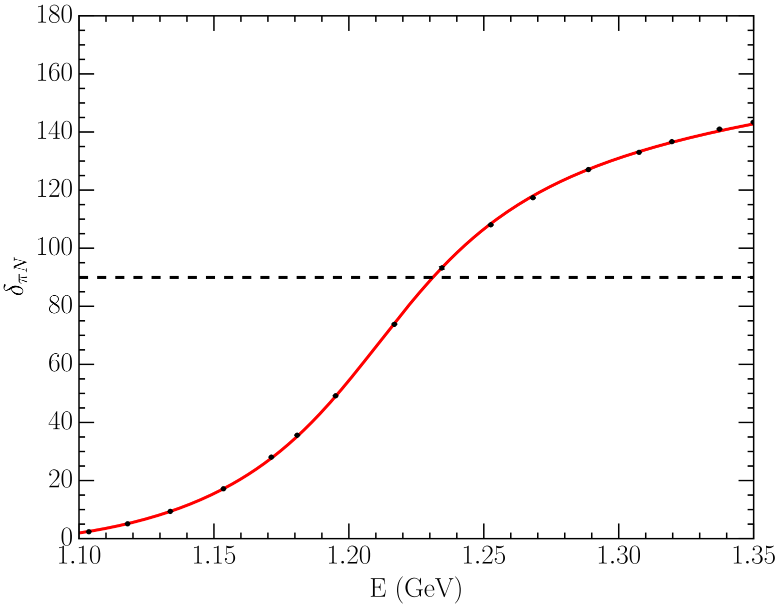

Figure 3.1: P-wave πN phase shifts for a system with a bare state, where the solid points are experimental data obtained from Ref. [54, 55], the solid line is the fit using HEFT to the data, and the dashed line represents a phase shift of 90 degrees. The parameter set producing this curve is provided in Table 3.1, and results in a χ^2/d.o.f. of 18.22.

to 1.3 GeV. If we take a similar approach, a χ^2/d.o.f. of 0.07 is found for an uncertainty of 3%. An uncertainty of 1% is required to bring the χ^2/d.o.f. above 1.0, and as such with this method of comparison this fit may be considered more than comparable. This fit also has excellent visual agreement with Ref. [58] and Ref. [59], which do not quote χ^2.

Considering the parameters in Table 3.1, we find a bare mass of $m_{\Delta_0} = 1.359$ GeV. For a physical mass given by $M = m_{\Delta_0} - \Sigma_{\pi N \pi N}(M)$, this implies that there is approximately a 130 MeV dressing on the bare basis state to produce the physical Δ baryon at $M = 1.232$ GeV. As can be seen in the phase shifts of Fig. 3.1, the phase shift curve indeed appears to pass through $90°$ at approximately 1.23 GeV, where a phase shift of $90°$ corresponds with a peak in the cross-section, and therefore a resonance. The coupling $g^{\Delta}_{\pi N}$ may be compared to the value predicted by χEFT. In Ref. [60], and using the notation of this thesis, the potential $G^{\Delta}_{\pi N}(k)$ is written as

$$G^{\Delta}_{\pi N}(k)^2 = \chi_\Delta \, \frac{2}{\pi} \, \frac{k^2 \, u(k)^2}{\omega_\pi(k)} \, , \tag{3.18}$$

where the coupling constant has the form

$$\chi_\Delta = \frac{3}{32\pi f_\pi^2} \, \frac{2}{9} \mathcal{C}^2 \, . \tag{3.19}$$

This coupling is written in terms of the pion decay constant, $f_\pi = 92.4$ MeV, and $\mathcal{C} = -1.52$, derived from SU(3) flavour relations. Evaluating $\sqrt{2\chi_\Delta/\pi}$ with these values, and normalising by a factor of $1/m_\pi$ to make the coupling dimensionless, gives a value

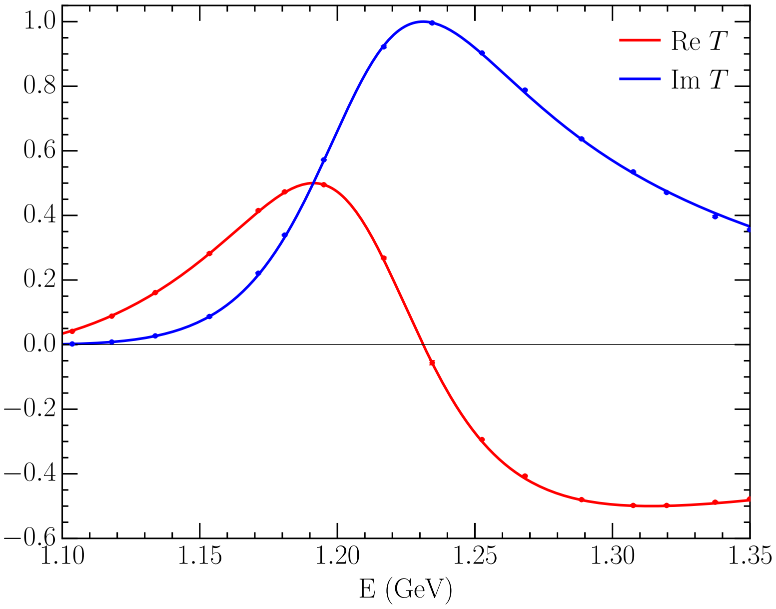

Figure 3.2: T-matrix components for the single bare state system, where the solid points are the SAID WI08 solution [54, 55]. The red and blue solid curves correspond with the real and imaginary components of the T-matrix calculating using the parameter set in Table 3.1.

of $g^{\Delta}_{\pi N}\big|_{\chi\text{EFT}} \approx 0.148$. Therefore the HEFT coupling of $g^{\Delta}_{\pi N}\big|_{\text{HEFT}} = 0.1762$ is very comparable to the χEFT value, with some renormalisation as described in Sec. 2.2.2.

Additionally, we are able to search for a pole in the T-matrix, found for the complex energy E_{pole} such that

$$A(E_{\text{pole}})^{-1} = E_{\text{pole}} - m_{\Delta_0} - \Sigma_{\pi N}(E_{\text{pole}}) - \Sigma^{\text{I}}_{\pi N}(E_{\text{pole}}) = 0\,. \tag{3.20}$$

By searching on the second Riemann sheet, with a complex momentum rotation of $k \to k\,e^{-i\pi/3}$, we find a single pole at a position of $E_{\text{pole}} = 1.211 - 0.049i$ GeV. Given that the imaginary component of a pole is related to the width of the resonance, labelled Γ_{Δ}, according to $\Gamma_{\Delta} = -2\,\text{Im}\,E_{\text{pole}}$, this implies a resonance width of approximately 100 MeV. Comparing the position of this pole to the PDG value of $1.210(1) - 0.050(1)i$ GeV [3], we observe excellent agreement. This agreement is particularly manifest in Fig. 3.2, where a comparison between the T-matrix as predicted by HEFT and the T-matrix predicted by the WI08 data is presented.

Given a parameter set which has excellent agreement with both data for the P_{33} scattering phase shifts and the PDG pole position, we are able to use the constrained Hamiltonian to make predictions about the finite-volume behaviour of this system.

3.1.2 Finite-Volume Energy Spectrum

Given our choice of a dipole form factor for the finite-range regulator, we are able to solve for the maximum allowed momentum in the system, and therefore the size of the Hamiltonian matrix.

As discussed in Sec. 2.4.2, we choose some u_{min} such that the computational time is minimised, but the Hamiltonian being large enough such that decreasing u_{min} further does not alter the eigenvalues of the Hamiltonian. Solving for the maximum momentum this corresponds to for the dipole form factor from Eq. (3.5), we find

$$k_{\text{max}} = \Lambda \sqrt{u_{\text{min}}^{-\frac{1}{2}} - 1} \,. \tag{3.21}$$

For $u_{\text{min}} = 0.01$, and a regulator parameter of 0.8 GeV, this therefore corresponds with a maximum momentum of $k_{\text{max}} = 2.4$ GeV.

Given this maximum allowed momentum for this system, the free Hamiltonian is written as

$$H_0^{\text{fin}} = \text{diag}\left(m_{\Delta_0},\, \omega_{\pi N}(k_1),\, \omega_{\pi N}(k_2),\, \cdots,\, \omega_{\pi N}(k_{\text{max}})\right) . \tag{3.22}$$

Modifying the potentials in Eq. (3.2) and Eq. (3.3) to include the finite-volume factors, the interaction Hamiltonian has the matrix form

$$H_{\text{I}}^{\text{fin}} = \begin{pmatrix} 0 & \overline{G}_{\pi N}^{\Delta}(k_1) & \overline{G}_{\pi N}^{\Delta}(k_2) & \cdots & \overline{G}_{\pi N}^{\Delta}(k_{\text{max}}) \\ \overline{G}_{\pi N}^{\Delta}(k_1) & \overline{V}_{\pi N \pi N}(k_1, k_1) & \overline{V}_{\pi N \pi N}(k_1, k_2) & \cdots & \overline{V}_{\pi N \pi N}(k_1, k_{\text{max}}) \\ \overline{G}_{\pi N}^{\Delta}(k_2) & \overline{V}_{\pi N \pi N}(k_2, k_1) & \overline{V}_{\pi N \pi N}(k_2, k_2) & \cdots & \overline{V}_{\pi N \pi N}(k_2, k_{\text{max}}) \\ \vdots & \vdots & \vdots & \ddots & \vdots \\ \overline{G}_{\pi N}^{\Delta}(k_{\text{max}}) & \overline{V}_{\pi N \pi N}(k_{\text{max}}, k_1) & \overline{V}_{\pi N \pi N}(k_{\text{max}}, k_2) & \cdots & \overline{V}_{\pi N \pi N}(k_{\text{max}}, k_{\text{max}}) \end{pmatrix} . \tag{3.23}$$

Therefore the full Hamiltonian may be constructed as $H^{\text{fin}} = H_0^{\text{fin}} + H_{\text{I}}^{\text{fin}}$.

With the finite Hamiltonian constructed, we obtain the energy eigenvalues by solving the eigenvalue equation $\left|H^{\text{fin}} - E\,\mathbb{I}\right| = 0$. It is worth noting that in the simplest case, where $v_{\pi N \pi N} = 0$, this eigenvalue equation can be written in a simple form, giving eigenvalues as solutions of

$$E_i = m_{\Delta_0} - \sum_{n=1}^{n_{\text{max}}} \frac{\overline{G}_{\pi N}^{\Delta}(k_n)^2}{\omega_{\pi N}(k_n) - E_i} \,. \tag{3.24}$$

Taking the infinite volume limit, where L, $n_{\text{max}} \to \infty$, and associating the energy E with the physical, renormalised mass m_Δ, this eigenvalue equation recovers the expression for the one-loop correction to the Δ mass from χEFT,

$$m_\Delta = m_{\Delta_0} - \left(\frac{g_{\pi N}^{\Delta}}{m_\pi}\right)^2 \int dk \, \frac{k^4\, u(k)^2}{\omega_\pi(k)\left[m_\Delta - \omega_{\pi N}(k) + i\varepsilon\right]} \,. \tag{3.25}$$

In order to investigate the effects of the lattice size L on the system, which is manifest in the momentum discretisation $k_n = 2\pi n/L$, we can solve the eigenvalue equation for a

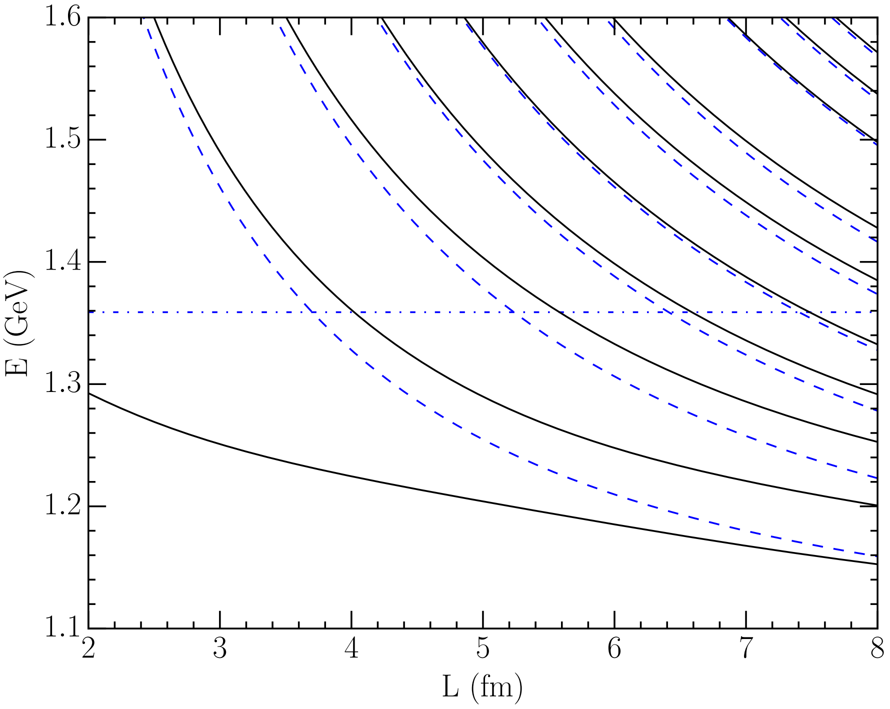

Figure 3.3: Dependence of the energy eigenvalues of the Hamiltonian on the (spatial) lattice size. The solid lines represent the energy eigenvalues following from the parameter set in Table 3.1. The (blue) horizontal dot-dashed line is the bare mass and the (blue) curved dashed lines are the non-interacting πN basis states at $k = 2\pi/L, 2\sqrt{2}\pi/L, \ldots$

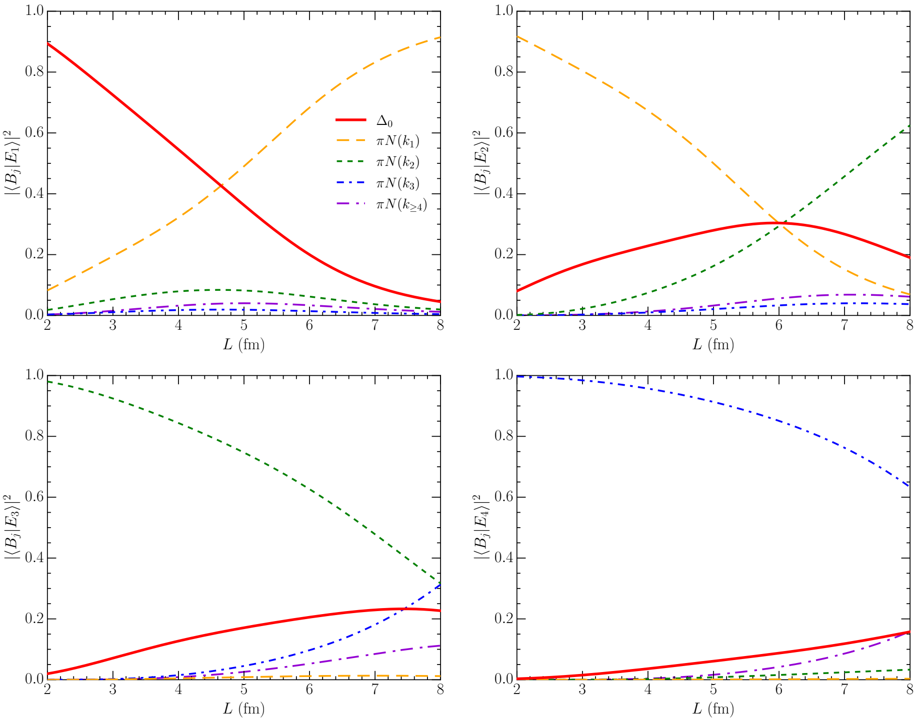

Figure 3.4: Dependence of the eigenvector components for the low-lying energy-eigenstates on the lattice size L. The solid (red) line corresponds with the contribution from the bare basis state, while the dashed lines are the eigenvector components for πN scattering states. The purple dashed line labelled $\pi N(k_{\geq 4})$ sums all contributions from higher momentum scattering states.

range of L. Typical baryon spectroscopy studies in lattice QCD require a lattice size of $L \sim 2$ fm or higher, and as such the finite-volume energy spectrum from $L = 2$ fm to $L = 8$ fm is illustrated in Fig. 3.3. Here, it can be seen how the interactions between the bare basis state, and the two-particle states result in a significant shift away from the non-interacting energies. Initially, for $L \sim 2$ fm, this shift is of the order several hundred MeV. As the lattice size increases, and the density of states also increases, this shift significantly decreases to around 10-20 MeV.

To gain better insight into the structure of these eigenstates, we are able to also calculate the eigenvectors $\langle B_j|E_i\rangle$, where $|B_j\rangle$ are the basis states of the system. Considering the first four states, the eigenvector composition as a function of the lattice size L are illustrated in Fig. 3.4. Here, it can be seen that over the range of lattice sizes considered, the majority of the contribution from the bare basis state (coloured red) is concentrated in the first four eigenstates. For $L \sim 2$ fm, the majority of the bare state contribution is concentrated in the ground state. As the lattice size increases however, this contribution is spread out among the nearby states, and the eigenstate with the largest bare state component begins to move to a higher energy in the spectrum. The πN scattering states have a similar behaviour, where a majority of the eigenvector components corresponding with them is concentrated on a single eigenstate initially, before spreading throughout nearby eigenstates for large L.

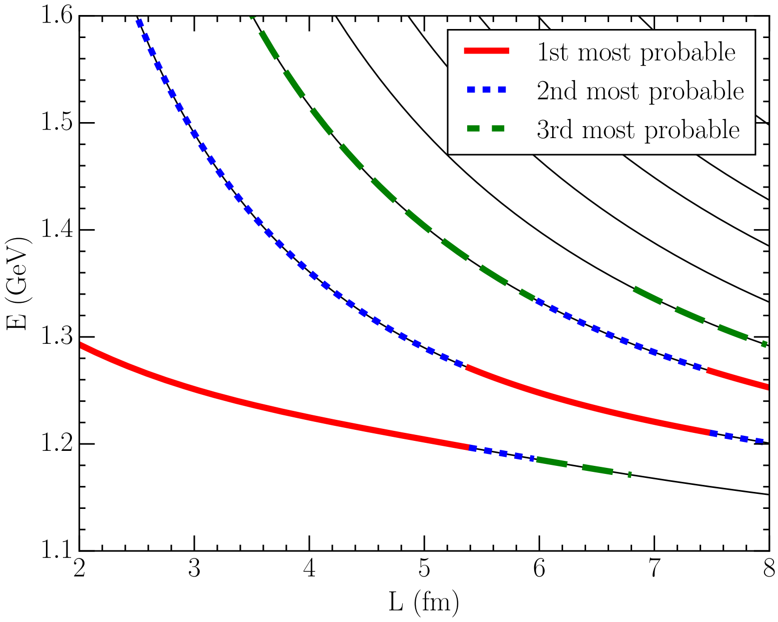

Figure 3.5: Lattice volume dependence of the energy eigenvalues of the Hamiltonian with parameters given in Table 3.1. The solid (red), short-dashed (blue) and long-dashed (green) highlights on the eigenvalues correspond to the states with the largest, second-largest and third-largest contribution from the bare basis state $|\Delta_0\rangle$ respectively.

As we associate the eigenstate with the largest bare basis state component with a state constructed from three-quark interpolating fields in lattice QCD, it is convenient to illustrate the states in the energy spectrum with the highest bare state contribution. This can be seen in Fig. 3.5, where the eigenstates with first, second, and third largest bare state component in their eigenvectors have been highlighted. These have been labelled as first, second, and third most probable states, as they are the most probable states to be observed in lattice QCD studies using three-quark operators. It can be seen in this illustration that the energy eigenvalue with largest bare state contribution is concentrated around the physical mass of the Δ, at 1.232 GeV. Interestingly, in the finite-volume spectrum the bare basis state eigenvector components are also spread over eigenstates within a range of approximately 100 MeV, which corresponds with the width of the Δ resonance.

In order to make a connection with available lattice QCD data for the Δ, we are required to extrapolate the finite-volume energy spectrum to unphysical pion, and therefore hadron masses. To do so we take the mass of the nucleon to vary in m_π^2 according to

$$m_N(m_\pi^2) = m_N|_{\text{phys}} + \alpha_N \left(m_\pi^2 - m_\pi^2|_{\text{phys}} \right) , \tag{3.26}$$

where the mass slope for the nucleon is $\alpha_N = 1.435$ GeV^{-1}. This value was found by fitting the functional form of Eq. (3.26) to lattice QCD calculations of the ground state nucleon mass at various pion masses. To calculate the mass slope of the bare basis state, we consider lattice QCD calculations for the ground state Δ, such as those from Ref. [47]. By calculating the finite-volume energy spectrum at the pion masses corresponding with the

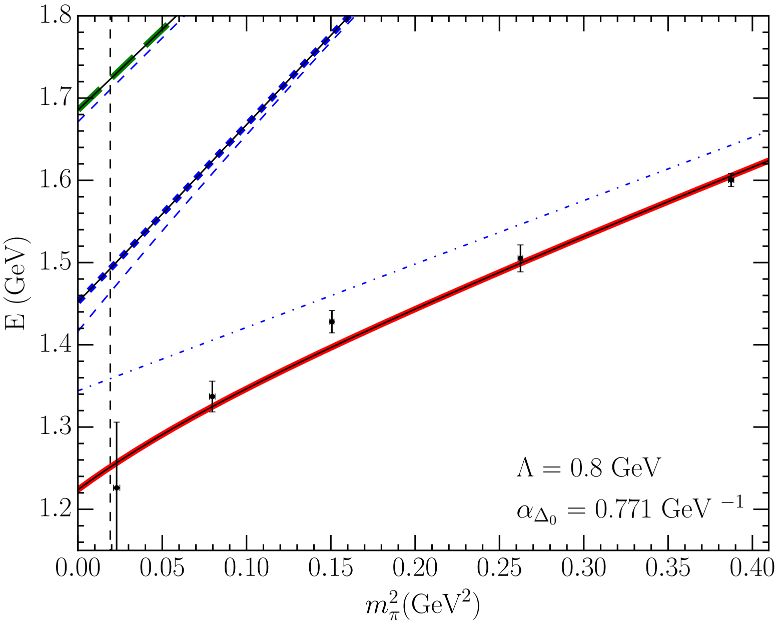

Figure 3.6: Pion mass dependence of the finite-volume HEFT eigenvalues at L = 2.99 fm for the parameter set given in Table 3.1. The solid black curves illustrate the finite-volume energy levels predicted by HEFT from fits to experimental phase shifts. These lines are dressed by solid (red), short-dashed (blue) and long-dashed (green) highlights indicating states with the largest, second-largest and third-largest contribution from the bare basis state $|\Delta_0\rangle$ respectively. Lattice QCD results for lowest-lying Δ masses, denoted by the (black) points, are from the PACS-CS collaboration [47]. As these lattice results follow from local three-quark operators, they are expected to lie on a solid (red) energy eigenstate. The vertical dashed (black) line illustrates the physical pion mass, while the thin (blue) dashed lines denote the bare mass and scattering basis states.

lattice QCD data, we are able to vary the bare mass slope such that the HEFT eigenvalue dominated by bare state contributions corresponds with the lattice QCD masses.

Taking the mass of the bare state, given by m_{Δ_0} to vary with pion mass as the simple residual series expansion

$$m^2_{\Delta_0}(m^2_\pi) = m_{\Delta_0}|_{\text{phys}} + \alpha_{\Delta_0}\left(m^2_\pi - m^2_\pi|_{\text{phys}}\right) , \tag{3.27}$$

where $m_{\Delta_0}|_{\text{phys}}$ is the mass of the bare state at the physical point, we find a bare mass slope of $\alpha_{\Delta_0} = 0.771$ GeV^{-1} is best able to describe the lattice QCD data obtained from Ref. [47]. The finite-volume energy spectrum for this mass slope is illustrated in Fig. 3.6. In this figure, which uses the same method of colouring eigenstates to indicate the bare basis state composition, we see that for all pion masses the largest component of the bare basis state is contained in the ground state. Using this simple bass mass expansion, we do observe some difficulty in describing the state at the third-lightest pion mass however. At larger pion masses, the first and second excited states are predominantly composed of πN scattering states, with little contribution from the bare basis state.

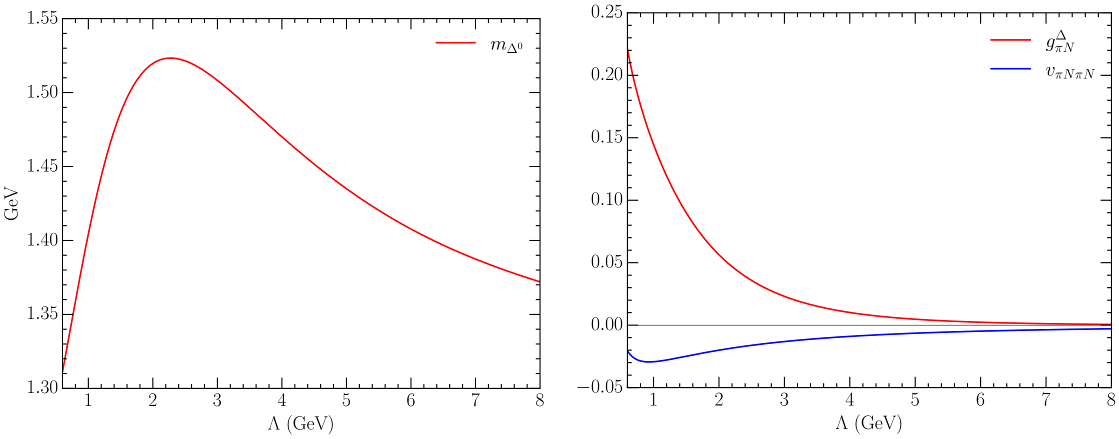

Figure 3.7: Dependence of the parameters used to constrain the Hamiltonian on the regulator parameter Λ. The left plot displays the Λ-dependence of the bare mass, while the right plot considers the Λ-dependence of the two coupling strengths.

3.1.3 Dipole Regulator Dependence

As Lüscher's method is embedded in Hamiltonian Effective Field Theory, it is expected that any parameter set which is able to describe the experimental data should produce an equivalent finite-volume energy spectrum at the physical point. It is less clear how changing the regulator parameter, and finding a new parameter set to describe the experimental data would manifest in the eigenvalues outside of the fit region. Different parameter sets may also affect the eigenvectors of the Hamiltonian, which are not physical observables, as well as the extrapolation of energy eigenvalues to unphysical pion masses.

To do so, we consider fitting the experimental data with Λ from 0.6 to 8.0 GeV, continuing to use a dipole form factor. $\Lambda = 8.0$ GeV was chosen as the upper bound, as this is the smallest value of Λ required to get a good description of the experimental data without a bare basis state, as will be explored in the following text. It is found that the full range of Λ considered is able to describe the experimental data up to $E = 1.35$ GeV, and the dependence of the bare mass, and two coupling strengths are presented in Fig. 3.7. Here, it can be seen that as Λ increases up to approximately 2 GeV, the bare mass is also increasing. As Λ increases, the self-energy also increases, as more short-distance physics is included. Therefore to formulate the physical Δ mass, the bare mass is required to increase proportionally. Above $\Lambda \approx 3$ GeV, we find that self-energy terms are becoming increasingly dominated by interactions between scattering states, where the T-matrix has a larger contribution from the coupling strength $v_{\pi N \pi N}$ compared to from $g^{\Delta}_{\pi N}$. As such, for $\Lambda = 8.0$ GeV, we find that a bare basis state is no longer required to produce a resonance corresponding with the $\Delta(1232)$.

Removing the bare Δ_0, and constructing a Hamiltonian with only πN scattering states leaves only a single free parameter, $v_{\pi N \pi N}$. By solving the scattering equations for this system using a dipole regulator with $\Lambda = 8.0$ GeV, we find that it is possible to describe

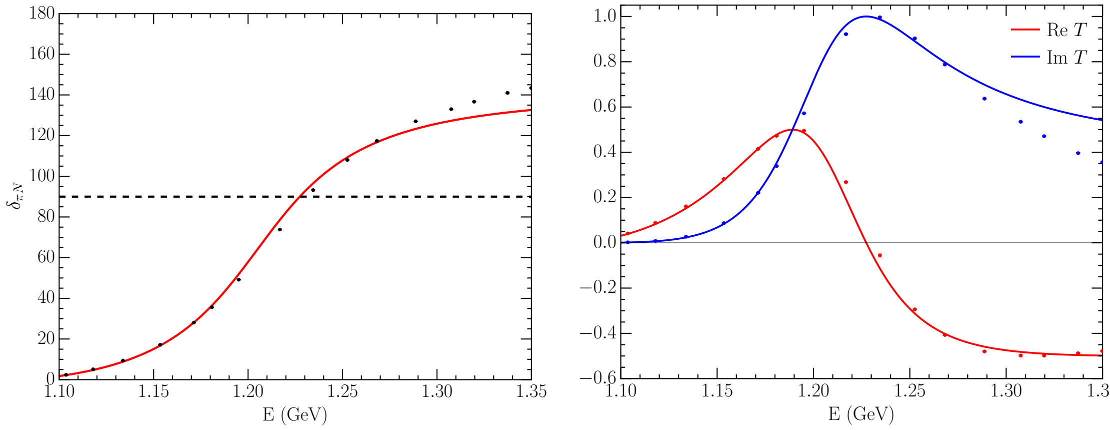

Figure 3.8: P-wave πN phase shifts and T-matrix components for a system with no bare state, where the solid points are experimental data obtained from Ref. [54, 55]. The solid lines are the fit using HEFT to the data, and the dashed line represents a phase shift of 90 degrees. The parameter set producing these curves is given by Fit IV of Table 3.2, with $\Lambda = 8.0$ GeV.

the experimental data in the region of the Δ resonance. This results in a coupling strength of $v_{\pi N \pi N} = -0.0029$. Considering a larger value of Λ found no substantial increase in the ability to describe the experimental data. A comparison of the phase shift and T-matrix from HEFT with the experimental data is presented in Fig. 3.8. As can be seen, while this system is able to produce a resonance in the correct region, it struggles to reproduce the scattering properties for higher energies. By searching for a pole in the T-matrix, as described in Eq. (2.50) for a system with no bare states, a pole was found for $E_{\text{pole}} = 1.205 - 0.045i$ GeV. While this is a worse description of the pole compared to the system containing a bare state, it is still close to the PDG value of $1.210(1) - 0.050(1)i$ GeV.

As both systems are capable of describing the experimental data in the resonance region, it is desirable to see how this manifests in a finite-volume, and more generally how the regulator parameter affects finite-volume quantities.

By constructing the Hamiltonian for this system in a finite volume for each parameter set, we are able to solve the eigenvalue equation to test the model-independence of the energy eigenvalues. The results of this are shown in Fig. 3.9 Here it can be seen that all energy eigenvalues which lie within the fit region of $E \leq 1.35$ GeV are independent of the regulator parameter Λ. Within this region, the fit parameters are described by experimental data, and therefore by the Lüscher mechanism embedded in HEFT all fit parameters should produce the same finite-volume energy spectrum. Above $E \approx 1.35$ GeV, the Hamiltonian is not constrained to experimental data, and the regulator has taken on the role of a model for the higher energy eigenstates. Despite the Λ-dependence observed in the higher energy eigenvalues of Fig. 3.9, when considering a small Λ region of 0.6 GeV to 1.0 GeV where a typical study would focus there is little variance observed in the energy eigenvalues.

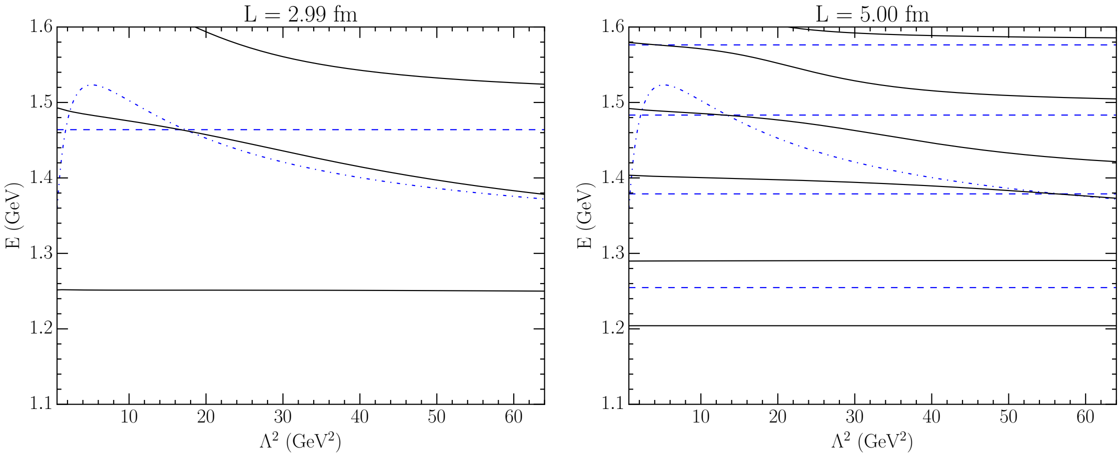

Figure 3.9: Dependence of the lowest lying eigenvalues of the finite-volume Hamiltonian on the regulator parameter Λ for two different lattice sizes, where Λ is varying from 0.6 to 8.0 GeV. The solid (black) lines are the eigenvalues, the horizontal dashed (blue) lines are πN basis states, and the curved dot-dashed (blue) line is the mass of the bare Δ_0 . The Hamiltonian was constrained to experimental data with $E \leq 1350$ MeV.

While the eigenvalues are Λ-independent within the region constrained by experiment, it is less clear how the eigenvectors behave as Λ is varied. Significant Λ-dependence in the eigenvectors can have impact on the interpretation of the structure of states of interest, and in particular may affect the position of the eigenstate dominated by bare state contributions. For an $L = 3$ fm volume, the dependence of the Hamiltonian eigenvectors are illustrated in Fig. 3.10. Here, it can be seen that as Λ increases, the concentration of the bare basis state in the ground level drops rapidly. Instead, the majority of the bare state contribution moves to the first excited state. As the bare state eigenvector component in the ground state decreases, it instead becomes a mix of higher scattering states, implying that the ground state is perhaps representing a dynamically generated Δ for the case of very large Λ.

Similar behaviour is observed for larger lattice sizes, where the eigenstates within the vicinity of the renormalised Δ mass gain strong contributions from many higher scattering states for large Λ. This can be seen in Fig. 3.11, where the eigenvectors for the first four energy eigenvalues are displayed. Here, it becomes clear that as Λ increases, and as the coupling $g^{\Delta}_{\pi N}$ reduces proportionally, the majority of the contribution from the bare Δ becomes concentrated in the nearest eigenstate. At this point, the second excited state has effectively become a non-interacting bare basis state, further indicating the Δ has become dynamically generated by a very short-range interaction.

It appears that the full range of Λ considered, both with and without a bare basis state, is able to provide a description of the Δ resonance in both infinite-volume and finite-volume formulations. One strength of HEFT however, is the ability to extend the formalism beyond the physical point, and compare with lattice QCD. This has the ability to provide additional insight into the Λ-dependence of these states, and possibly give direction into which picture best represents the Δ resonance.

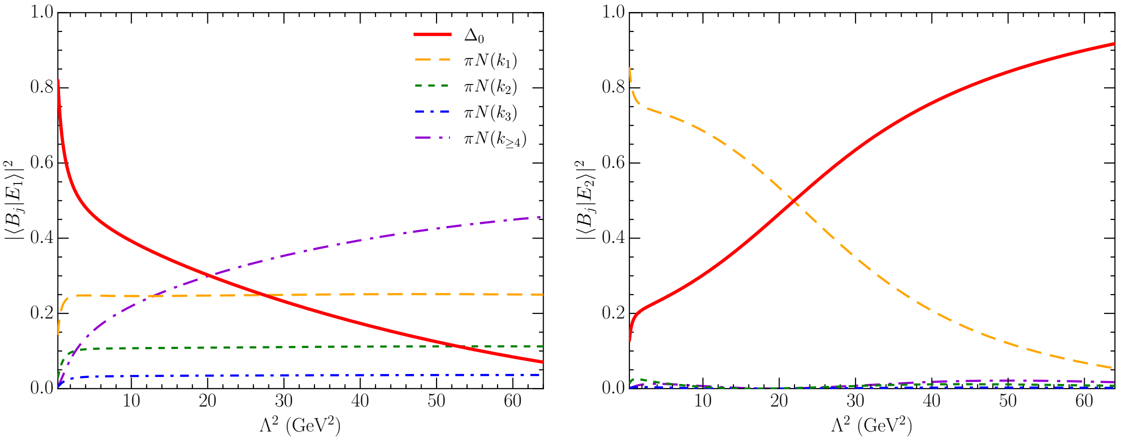

Figure 3.10: Dependence of the energy-eigenstate basis-state structure on the regulator parameter Λ, where Λ is varying from 0.6 to 8.0 GeV, for a lattice size of $L = 2.99$ fm. The two lowest-lying eigenstates are shown, to best illustrate the behaviour of the eigenvector component for the bare basis state.

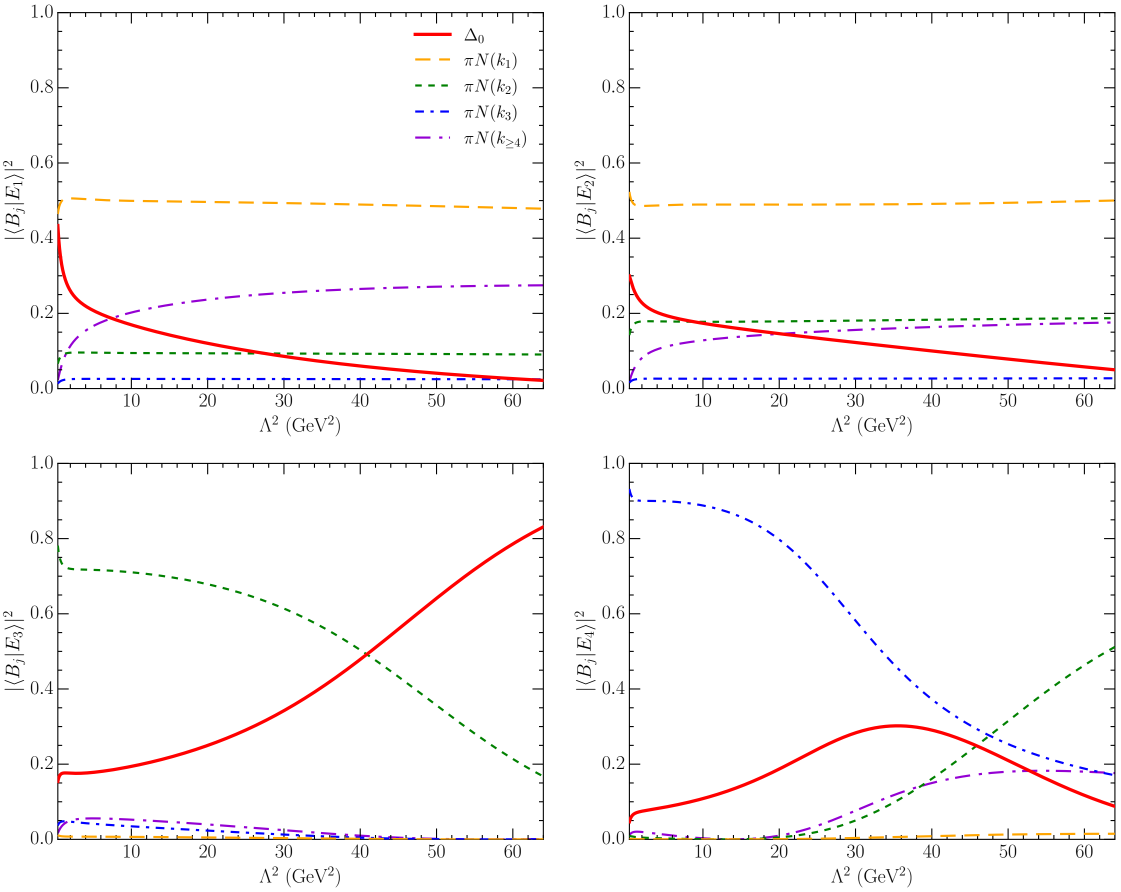

Figure 3.11: Dependence of the energy-eigenstate basis-state structure on the regulator parameter Λ, where Λ is varying from 0.6 to 8.0 GeV, for a lattice size of $L = 5.00$ fm. The first four eigenstates are illustrated.

Table 3.2: Single-channel fit parameters constrained to the WI08 solution of the P_{33} πN scattering data [54, 55]. Fits I-III contain a single-particle basis state $|\Delta_0\rangle$, while Fit IV does not.

	With $\vert\Delta_0\rangle$			No $\vert\Delta_0\rangle$
Parameter	Fit I	Fit II	Fit III	Fit IV
m_{Δ_0}/ GeV	1.311	1.497	1.470	-
$g^{\Delta}_{\pi N}$	0.2210	0.0818	0.0101	-
$v_{\pi N,\pi N}$	-0.0205	-0.0238	-0.0090	-0.0029
Λ/ GeV	0.6000	1.6000	4.0000	8.0000
d.o.f.	13	13	13	15
χ^2	75.86	230.85	194.68	24373.42
χ^2/d.o.f.	5.84	17.76	14.98	1624.90
α_{Δ_0}/ GeV^{-1}	0.855	0.566	0.516	-
$\alpha_{\Delta_0,2}$/ GeV^{-1}	1.264	0.655	0.370	-
$\alpha_{\Delta_0,4}$/ GeV^{-3}	-1.061	-0.231	0.375	-
Pole / GeV	$1.210 - 0.050i$	$1.210 - 0.049i$	$1.209 - 0.049i$	$1.205 - 0.045i$

As described in Sec. 3.1.2, we are able to fit the bare mass slope for a given parameter set to lattice QCD data at a variety of pion masses. In order to investigate the Λ-dependence at unphysical pion masses, we will consider four sets of fit parameters, each with a different Λ. These four sets of fit parameters are presented in Table 3.2, and labelled Fit I through to Fit IV, where Fit IV does not contain a bare basis state. As can be seen in this table, the bare mass slope, given by α_{Δ_0}, has a general trend of decreasing as the regulator parameter increases. As for $\Lambda = 8.0$ GeV, a bare state is no longer required to describe the experimental data, where the parameters for this system are presented in Fit IV.

The finite-volume energy spectra as a function of the pion mass, and utilising these bare mass slopes, are presented in Fig. 3.12. Here, it can be seen that for a regulator parameter of 0.6 GeV, the smallest considered, there is minimal curvature in the ground state eigenvalue, due to the small bare mass. As a result, it is difficult to describe all of the lattice QCD data, which exhibits a clear non-linear behaviour for small pion masses. While a regulator parameter in the range of 1.6 GeV and above is able to give a good description of the lattice QCD data, we find that at $\Lambda = 4.0$ GeV the first excited state becomes the state dominated by bare basis state contributions, and as a result is not consistent with the lightest lattice QCD mass. For the system with no bare state, and $\Lambda = 8.0$ GeV, the Hamiltonian is completely unable to describe the data at any but the lightest point. Here, the strength of this approach is demonstrated, where without considering lattice QCD data in addition to experimental data, we would be unable to definitively judge the appropriateness of each system. This conclusion of being unable to describe the properties of the Δ without a bare mass is also in agreement with Ref. [61].

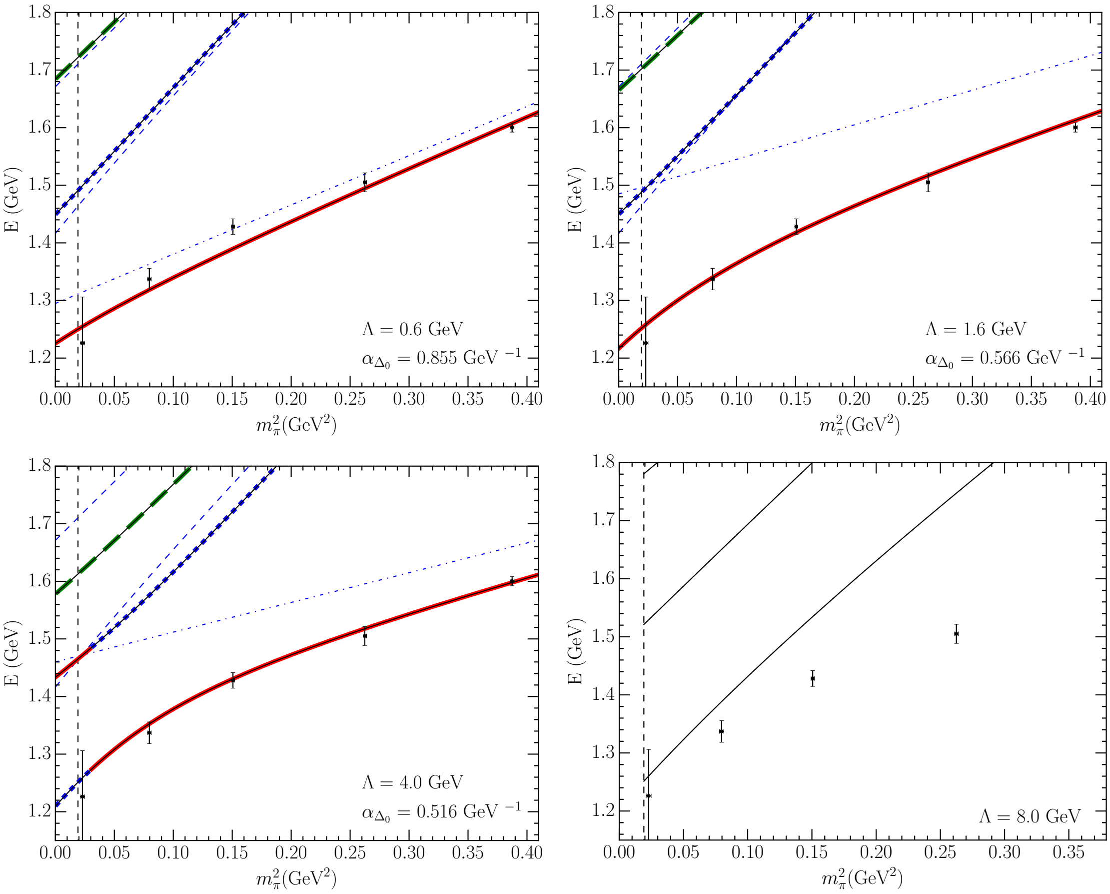

Figure 3.12: Pion mass dependence of the finite-volume HEFT eigenvalues at L = 2.99 fm for increasing values of the regulator parameter Λ . No bare basis state is present for $\Lambda = 8.0$ GeV. All other Λ values have a bare state mass expansion given by Eq. (3.27). The parameters for these fits are given by their corresponding entries in Table 3.2. The solid black curves illustrate the finite-volume energy levels predicted by HEFT from fits to experimental phase shifts. These lines are dressed by solid (red), short-dashed (blue) and long-dashed (green) highlights indicating states with the largest, second-largest and third-largest contribution from the bare basis state $|\Delta_0\rangle$ respectively. Lattice QCD results for lowest-lying Δ masses, denoted by the (black) points, are from the PACS-CS collaboration [47]. The vertical dashed (black) line illustrates the physical pion mass.

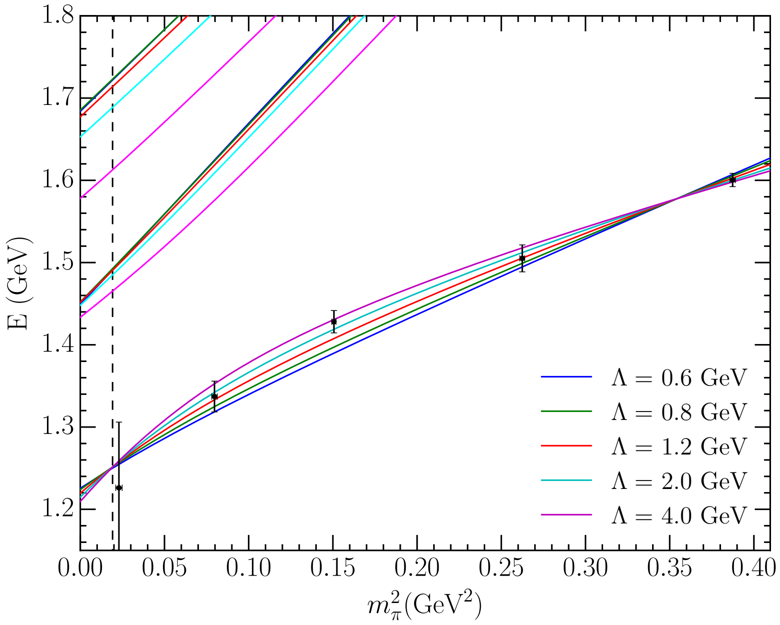

Figure 3.13: Pion mass dependence of the lowest-lying finite-volume HEFT eigenvalue at $L = 2.99$ fm using a dipole regulator, where the data points are the PACS-CS data. Several parameter sets corresponding with each value of Λ are overlapped, each with a corresponding bare mass expansion fit to the PACS-CS data. The bare state mass expansion for each value of Λ is constrained to Eq. (3.27).

While the $\Lambda = 1.6$ GeV system is able to describe the lattice QCD data, we find that the experimental data has a lower χ^2 for smaller regulator parameters. In addition, we observe more Λ-dependence in the first excited state, and the second excited state varies in position by as much as 100 MeV as Λ increases.

In order to better observe this Λ-dependence, Fig. 3.13 superimposes the finite-volume eigenvalues for a variety of Λ. Here, it can be clearly seen how all sets of fit parameters are constrained at the physical point, where the ground state eigenvalue is completely model-independent. As the pion mass increases, we quickly observe a spread of energy eigenvalues in the ground state. The first and second eigenstates have an even larger degree of Λ-dependence. As an attempt to remove this Λ-dependence, we propose adding an additional term to the residual series expansion of the bare mass, giving

$$m_{\Delta_0}(m_\pi^2) = m_{\Delta_0}\big|_{\text{phys}} + \alpha_{\Delta_0,2}\left(m_\pi^2 - m_\pi^2\big|_{\text{phys}}\right) + \alpha_{\Delta_0,4}\left(m_\pi^4 - m_\pi^4\big|_{\text{phys}}\right) . \tag{3.28}$$

This also introduces an additional mass slope parameter. In order to differentiate the slope parameters for the $\mathcal{O}(m_\pi^4)$ expansion, we label the two mass slopes as $\alpha_{\Delta_0,2}$ and $\alpha_{\Delta_0,4}$ for the m_π^2 and m_π^4 terms respectively. This additional degree of freedom may allow for a better description of the lattice QCD data, and remove Λ-dependence.

Utilising this new pion mass extrapolation for the bare state, we perform a similar fitting procedure as before, where the bare mass slopes are varied such that the ground state is able to describe the lattice QCD data. The new mass slopes are presented in Table 3.2,

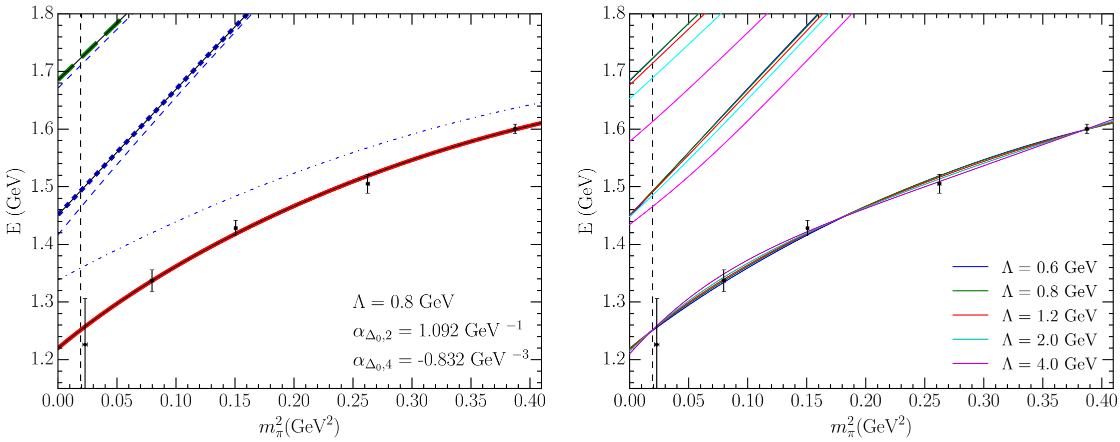

Figure 3.14: Pion mass dependence of the lowest-lying finite-volume HEFT eigenvalue at $L = 2.99$ fm using a dipole regulator, where the data points are the PACS-CS data. The left plot displays the eigenstate with largest bare basis state eigenvector component in red, with the dashed blue and long-dashed green lines having the second and third largest bare state component respectively. For the right plot, several parameter sets corresponding with each value of Λ are overlapped, each with a corresponding bare mass expansion fit to the PACS-CS data. The bare mass expansion is taken to $\mathcal{O}(m_\pi^4)$, with a form given by Eq. (3.28).

where it can be seen that a significant deviation from a linear form is found. The pion mass dependence of the finite-volume energy spectra are illustrated in Fig. 3.14, where both a single spectrum using a $\Lambda = 0.8$ GeV regulator parameter, and a superimposition of several Λ values are presented. As can be seen in the energy spectrum of the $\Lambda = 0.8$ GeV system, we observe a significant improvement in the ability to describe the lattice QCD data compared to Fig. 3.6. Considering many values of Λ, we also observe a significant reduction in Λ-dependence for the ground state, where all parameter sets are now able to describe the lattice QCD data equally well. The excited states of the system see little to no impact from the additional bare mass term, likely due to their composition primarily consisting of two-particle basis states.

As this system now has no preference for a particular value of Λ in the pion mass extrapolation, we are free to use other criteria for a choice of Λ. In the description of the scattering data, a smaller Λ of order 1 GeV seems to be preferred according to the χ^2 test. As such, a choice of $\Lambda = 0.8$ GeV seems particularly reasonable, as this also corresponds with a typical value chosen in other models, such as the cloudy bag model [41, 62].

3.1.4 Gaussian Regulator Dependence

While we have investigated the effects of varying the regulator parameter Λ in the previous section, this was only for a dipole regulator. To further extend this, we consider a similar

Table 3.3: Single-channel fit parameters constrained to the WI08 solution of the P_{33} πN scattering data [54, 55] for a Guassian regulator.

Parameter	Fit Value
m_{Δ_0}/ GeV	1.3851
$g^{\Delta}_{\pi N}$	0.1406
$v_{\pi N,\pi N}$	-0.0307
Λ/ GeV	0.8000
d.o.f	13
χ^2	244.74
χ^2/d.o.f.	18.83

study for a Gaussian regulator of the form

$$u(k,\Lambda) = \exp\left(-\frac{k^2}{\Lambda^2}\right) . \tag{3.29}$$

The range of regulator parameters considered for the dipole form factor was roughly based on a phenomenological lower-bound of around 0.8 GeV, and an upper-bound of 8 GeV, motivated by the ability to describe the experimental data without a bare state for $\Lambda = 8.0$ GeV. It is less obvious what range of parameters should be considered for the Gaussian regulator, and therefore we will briefly consider the relationship between the Gaussian and dipole regulator parameters. To do so, consider finding the dipole and Gaussian regulator parameters Λ_{D} and Λ_{G} respectively, such that the integrals over all momentum for each form factor are equal, giving

$$\int_0^\infty dk \left(1 + \frac{k^2}{\Lambda_{\mathrm{D}}^2}\right)^{-2} = \int_0^\infty dk \, \exp\left(-\frac{k^2}{\Lambda_{\mathrm{G}}^2}\right) . \tag{3.30}$$

These integrals may be evaluated algebraically, revealing the relationship

$$\Lambda_{\mathrm{G}} = \frac{\sqrt{\pi}}{2}\Lambda_{\mathrm{D}} . \tag{3.31}$$

As $\sqrt{\pi}/2 \approx 0.9$, it is reasonable to consider a similar range of regulator parameters for the Gaussian regulator.

Initially considering $\Lambda = 0.8$ GeV, as in Sec. 3.1.3, we are able to obtain set of fit parameters with a comparable χ^2/d.o.f. of 18.83, where the parameter set is given in Table 3.3. The associated πN phase shifts, and T-matrix values for this regulator form is given in Fig. 3.15

Similarly to the dipole form factor, a Gaussian regulator is able to provide a description of the experimental data for a large range of Λ values, though it appears to have a greater difficulty fitting the data for large Λ. As an example, for $\Lambda = 4.0$ GeV, a parameter set with $\chi^2/\text{d.o.f.} = 39.16$ was found, approximately three times higher than the $\Lambda = 4.0$

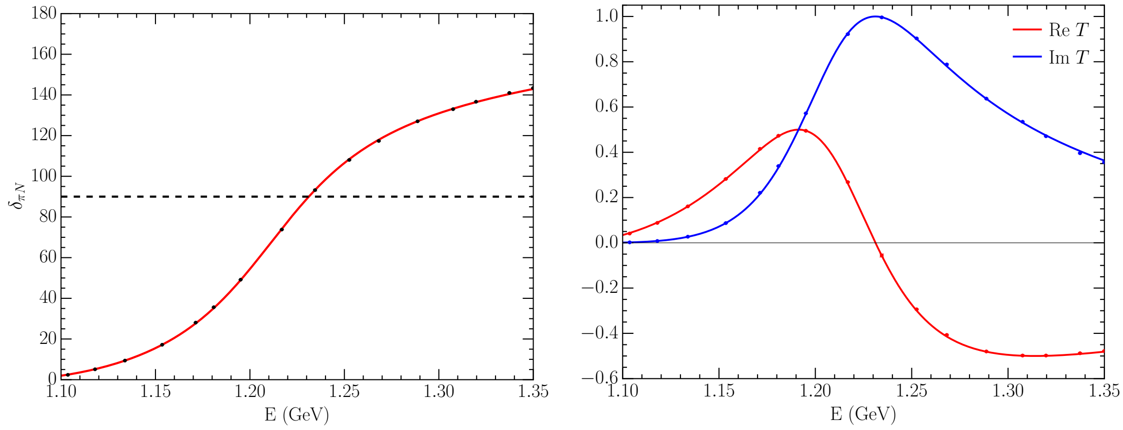

Figure 3.15: P-wave πN phase shifts and T-matrix components for a system with a single bare state and a Gaussian regulator, where the data points are experimental data obtained from Ref. [54, 55]. The solid lines are the fit using HEFT to the data, and the dashed line represents a phase shift of 90 degrees. The parameter set producing these curves is given by Fit IV of Table 3.3.

GeV fit for a dipole. Interestingly however, a Gaussian regulator is unable to produce a resonance without a bare basis state at all until values of $\Lambda \approx 12$ GeV. In order to generate a resonance at the correct mass however, $\Lambda \approx 16$ GeV is required. As such, this section will consider the range of $\Lambda = 0.6$ to $\Lambda = 4.0$ GeV, a range in which the Hamiltonian is able to provide a good description of the scattering data.

In a finite-volume, we may take a similar procedure to the dipole case where the dependence of the finite-volume eigenvalues on Λ is presented. Solving the eigenvalue equation for the Hamiltonian with each Λ value at both $L = 2.99$ fm and $L = 5.00$ fm, this dependence is illustrated in Fig. 3.16. Here, we observe a similar level of Λ-independence as in the dipole case for eigenvalues below the experimental data threshold of 1.35 GeV. Additionally, the model-dependence of the higher eigenvalues has a similar behaviour, though the Gaussian system is considered over a small range of Λ values.

Finally, by extending the formalism to unphysical pion masses, we are able to both compare the finite-volume spectrum with lattice QCD data, and investigate the model-dependence of the eigenvalues at unphysical pion masses. Taking the $\mathcal{O}(m_\pi^4)$ bare mass extrapolation as defined in Eq. (3.28), the results are presented in Fig. 3.17. We observe a similar level of model-independence in the ground state energy for the Gaussian regulator, as we do for the dipole. Considering the excited states however, there appears to be a larger degree of model-dependence, where the second excited state varies by as much as 150 MeV between the regulator values considered, in comparison to the 100 MeV difference in the dipole case.

As both the dipole and Gaussian regulators have a similar level of model-independence in the fit range, and the dipole form factor appears to have marginally better performance both outside of the fit range, and at unphysical pion masses, the remainder of this analysis will focus on a dipole regulator.

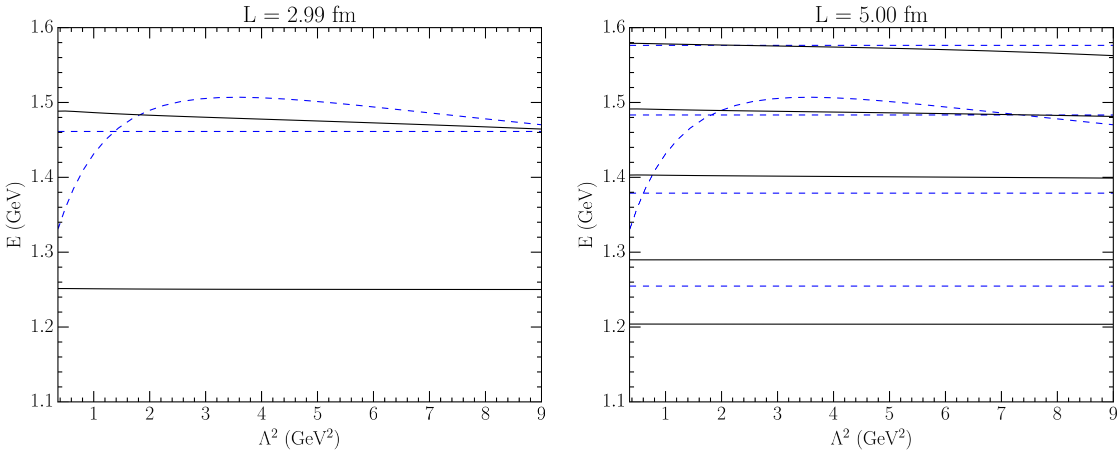

Figure 3.16: Dependence of the lowest lying eigenvalues of the finite-volume Hamiltonian on Λ for a Gaussian regulator at $L = 2.99$ fm and $L = 5.00$ fm. The solid (black) lines are the eigenvalues, the horizontal dashed (blue) lines are the πN scattering basis states, and the curved dot-dashed (blue) line is the mass of the bare Δ_0 . The Hamiltonian was constrained to experimental data with $E \leq 1350$ MeV.

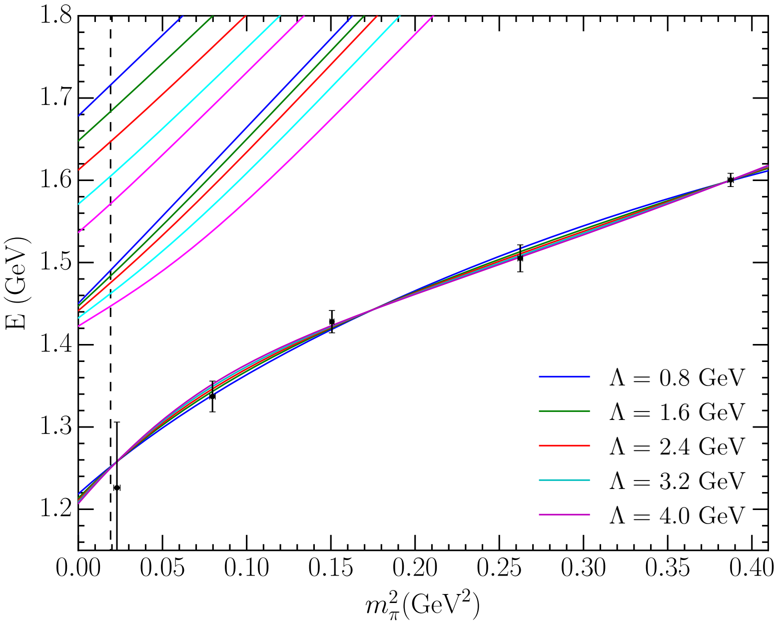

Figure 3.17: Pion mass dependence of the lowest-lying finite-volume HEFT eigenvalue at $L = 2.99$ fm using a Gaussian regulator, where the data points are the PACS-CS data. Five parameter sets corresponding to each value of Λ are overlapped, each with a corresponding $\mathcal{O}(m_\pi^4)$ bare mass expansion fit to the PACS-CS data.

3.2 Two Channel Analysis

While the effects of both the regulator form factor, and regulator parameter Λ have been considered for a wide range of systems, this is only for the simplest possible system, with a single scattering channel. In order to better understand these effects in a more broadly applicable case, as well as attempt to widen the range of scattering data which is used to constrain the Hamiltonian, we will consider the effects of adding a P-wave $\pi\Delta$ scattering channel to the Hamiltonian, and how regulator dependence may manifest in a more complex system.

3.2.1 Fitting Experimental Data

With the addition of a $\pi\Delta$ scattering channel, we are also able to significantly extend the range of scattering data which the Hamiltonian can describe. As such, this analysis will consider scattering data up $E = 1.65$ GeV. While this energy range does include contributions from the next positive parity Δ excitation, the $\Delta(1600)$, the study of this resonance is not the focus of this analysis. Above this energy range, there is an increasing contribution from F-wave $\pi\Delta$ scattering states, and as such in the interest of maintaining a limited degree of complexity in this study, we limit the energy range such that F-wave $\pi\Delta$ contributions are negligible.

The introduction of a second channel also introduces an additional three free coupling strengths to be constrained. These are the coupling between a $\pi\Delta$ scattering state and the bare basis state, given by $g^{\Delta}_{\pi\Delta}$, and the interaction strengths between scattering states. These are given by $v_{\pi\Delta\pi\Delta}$ and $v_{\pi N\pi\Delta}$, which describe the $\pi\Delta \to \pi\Delta$ and $\pi\Delta \to \pi N$ transitions respectively. The interactions associated with the $\pi\Delta$ channel are taken to have the same form as for the πN channel, as described in Sec. 3.1. Allowing α and β to represent these two scattering channels, the interaction between the bare basis state and a two-particle state generalises to

$$G^{\Delta}_{\alpha}(k) = \frac{g^{\Delta}_{\alpha}}{m_{\pi}^{\text{phys}}} \frac{k}{\sqrt{\omega_{\pi}(k)}} u(k,\Lambda) \,, \tag{3.32}$$

while the interaction between two scattering states generalises to

$$V_{\alpha\beta}(k,k') = \frac{v_{\alpha\beta}}{(m_{\pi}^{\text{phys}})^2} \frac{k}{\omega_{\pi}(k)} \frac{k'}{\omega_{\pi}(k')} u(k,\Lambda)\, u(k',\Lambda) \,. \tag{3.33}$$

Finally, the energy of a $\pi\Delta$ state with back-to-back momentum k is given by

$$\omega_{\pi\Delta}(k) = \sqrt{k^2 + m_{\pi}^2} + \sqrt{k^2 + m_{\Delta}^2} \,, \tag{3.34}$$

where m_{Δ} is the renormalised Δ mass of 1.232 GeV.

In order to constrain this extended set of parameters, we define the scattering equations for this system, giving

$$T_{\alpha\beta}(k,k';E) = \tilde{V}_{\alpha\beta}(k,k',E) + \sum_{\gamma} \int dq\, q^2 \, \frac{\tilde{V}_{\alpha\gamma}(k,q,E)\, T_{\gamma\beta}(q,k';E)}{E - \omega_\gamma + i\varepsilon} \,, \tag{3.35}$$

where α, β, and γ represent the πN and $\pi\Delta$ scattering states. As the Hamiltonian now contains two scattering channels, we are unable to use many of the simplifications described in Sec. 3.1.1, and instead rely on the full process of solving for the T-matrix as described in Sec. 2.3.1. Therefore the T-matrix may be decomposed into a contribution purely from background interactions, and a contribution from the bare state, giving $T_{\alpha\beta}(k,k';E) = t_{\alpha\beta}(k,k';E) + t^{\Delta}_{\alpha\beta}(k,k';E)$. In solving for the components of the T-matrix, the process is largely the same as the single channel case. The key difference is in the calculation of the integrals required. Consider $M_\alpha(E)$ as defined in Eq. (2.30). In calculating the contribution due to the $\pi\Delta$ channel, this integral is given by

$$M_{\pi\Delta}(E) = \int dq\, q^2 \, \frac{f_{\pi\Delta}(q)^2}{E - \omega_{\pi\Delta}(q) + i\varepsilon} \,, \tag{3.36}$$

where $f_{\pi\Delta}(q)$ has the form given in Eq. (3.4). In the single-channel case, this integral must be solved using a principle-value integral. When including the $\pi\Delta$ channel, while $\omega_{\pi\Delta}(q)$ is below the $\pi\Delta$ threshold of $E = m_\pi + m_\Delta$ this integral contains no singularity, and as such may be directly calculated by standard numerical techniques without the need of a principle value integral. The integrals $g_{f,\pi\Delta,\Delta_0}(E)$ and $\Sigma_{\pi\Delta,\Delta_0}(E)$ also have this behaviour. Considering this, the process to obtain the T-matrix and therefore the S-matrix is as performed for the single-channel system.

With the addition of a second scattering channel, and therefore a matrix representation of the S-matrix, we parameterise the S-matrix by both phase shifts and an inelasticity, η, both of which are used to constrain the Hamiltonian. Therefore given the S-matrix, we obtain these scattering observables as

$$\begin{aligned} \delta_{\pi N}(E) &= \frac{1}{2}\,\mathrm{atan}\left\{\frac{\mathrm{Im}\, S_{\pi N\pi N}(E)}{\mathrm{Re}\, S_{\pi N\pi N}(E)}\right\} \,, \\ \eta(E) &= |S_{\pi N\pi N}(E)| \,. \end{aligned} \tag{3.37}$$

While in principle the $\pi\Delta$ phase shifts may also be extracted from the S-matrix, in the absence of $\pi\Delta$ scattering data these will be model-dependent.

By comparing the phase shifts and inelasticity as found in HEFT with experimental data up to a centre-of-mass energy of $E = 1.65$ GeV, we are able to constrain the free parameters of the Hamiltonian for regulator parameters in the range $\Lambda = 0.8$ to $\Lambda = 1.2$ GeV. The scattering data used for comparison is the WI08 solution for single-energy P_{33} pion-nucleon scattering, available from Refs. [54] and [55]. As in the single-channel case, Powell's method [56] was used to minimise a χ^2 calculated between the HEFT scattering observables and experimental data. This was performed using 33 data points, and given

Table 3.4: Two-channel fit parameters constrained to the WI08 solution of the P_{33} πN scattering data [54, 55], for two values of the regulator parameter Λ.

Parameter	Fit V	Fit VI
m_{Δ_0}/ GeV	1.384	1.441
$g^{\Delta}_{\pi N}$	0.1286	0.1041
$g^{\Delta}_{\pi\Delta}$	0.1324	0.0171
$v_{\pi N,\pi N}$	-0.0103	-0.0233
$v_{\pi N,\pi\Delta}$	-0.0811	-0.0220
$v_{\pi\Delta,\pi\Delta}$	-0.0015	-0.0645
Λ/ GeV	0.8000	1.2000
d.o.f.	27	27
χ^2	304.29	377.67
χ^2/ d.o.f.	11.27	13.99
α_2/ GeV^{-1}	0.893	0.636
α_4/ GeV^{-3}	-0.481	-0.089
Pole 1 / GeV	$1.210 - 0.049i$	$1.211 - 0.049i$
Pole 2 / GeV	$1.434 - 0.207i$	$1.449 - 0.053i$

six free parameters, results in 27 degrees of freedom. The parameter sets for these fits are presented in Table 3.4, where comparable χ^2/d.o.f.s to the single-channel system were found.

It is notable that the range of regulator parameters at which we are able to describe the scattering data is considerably smaller than in the single channel case. As Λ is increased beyond 1.2 GeV, it becomes increasingly difficult to describe the inelasticity above the $\pi\Delta$ threshold. This difficult manifests to some degree in the $\Lambda = 1.2$ GeV case, where for $E \sim 1.6$ GeV, the HEFT inelasticity is trending away from the experimental inelasticity. This trend becomes more drastic for higher values of Λ, and therefore we limit our consideration to $\Lambda = 1.2$ GeV. This is illustrated in Fig. 3.18, where the phase shift, inelasticity, and T-matrix for each of the two fits is shown.

By performing a complex momentum rotation $k \to k\, e^{-i\pi/3}$, we are able to find two poles in the T-matrix for each of the parameter sets, both of which are provided in Table 3.4. For both parameter sets, the first pole corresponds with the physical Δ, and is comparable with the PDG pole position of $1.210(1) - 0.050(1)i$ GeV. The position of the second pole however seems to have a degree of model-dependence, and both the real and imaginary components vary with Λ. As the PDG quotes a pole position for the $\Delta(1600)$ at $1.510(50) - 0.135(35)i$ GeV, it is possible that this second pole does correspond with the $\Delta(1600)$, and the presence of this pole without a second bare state may indicate that the $\Delta(1600)$ is dynamically generated. The introduction of additional $\pi\pi N$ dynamics, in the form of an F-wave $\pi\Delta$ channel, or a P-wave $\pi N^*(1440)$ channel may be able to improve the position of the second pole. This however is outside the scope of this analysis, and will be left for future study.

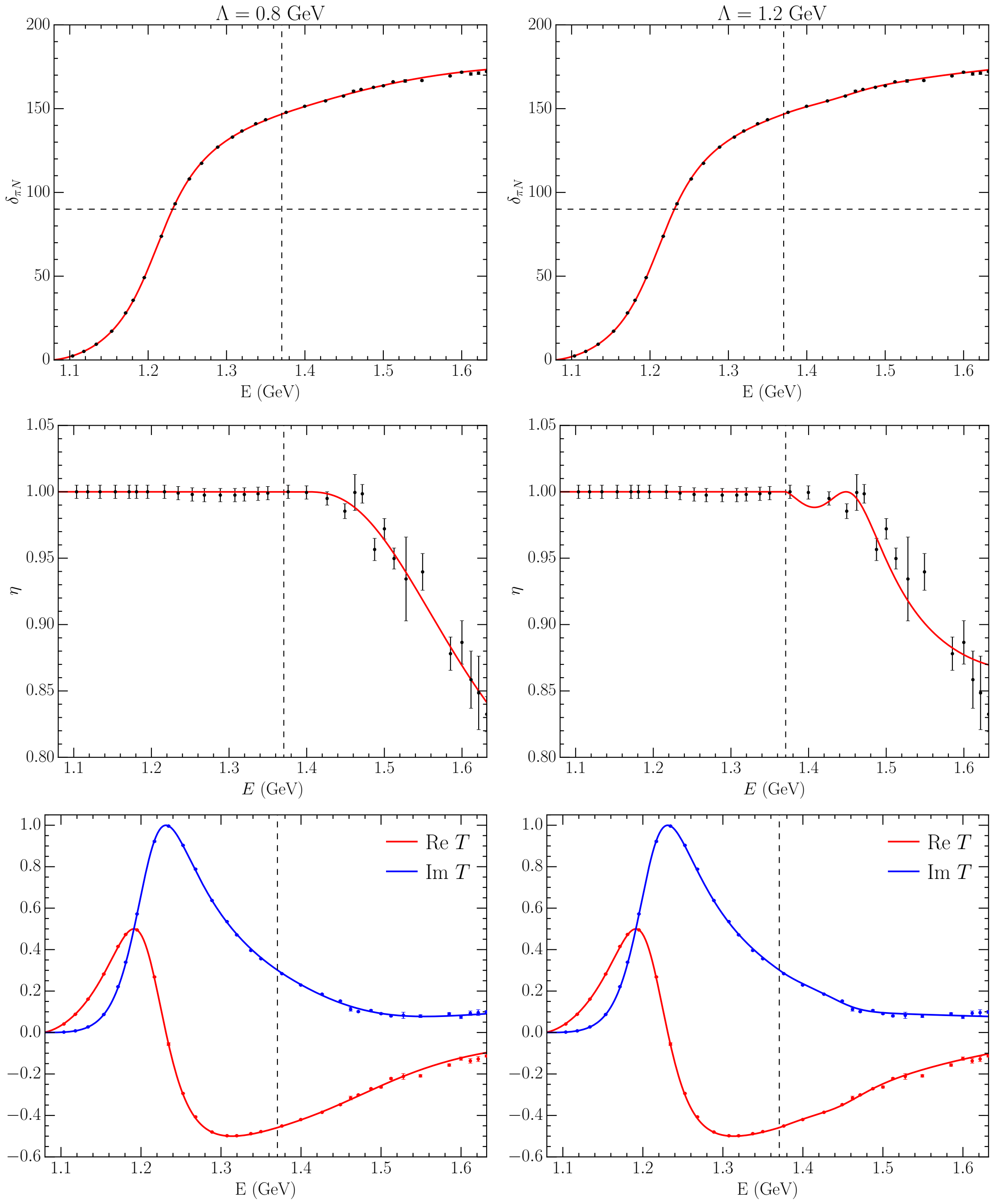

Figure 3.18: P-wave πN phase shifts and T-matrix components for a two-channel system with a single bare state and a dipole regulator, where the data points are experimental data obtained from Refs. [54] and [55]. The left plots have a regulator parameter of 0.8 GeV, while the right plots have a regulator parameter of 1.2 GeV. The solid lines are the fit using HEFT to the data, the vertical dashed lines represent the $\pi\Delta$ threshold, and the horizontal dashed line corresponds with a phase shift of 90 degrees. The parameter sets producing these curves are given by Fit IV and Fit V of Table 3.4.

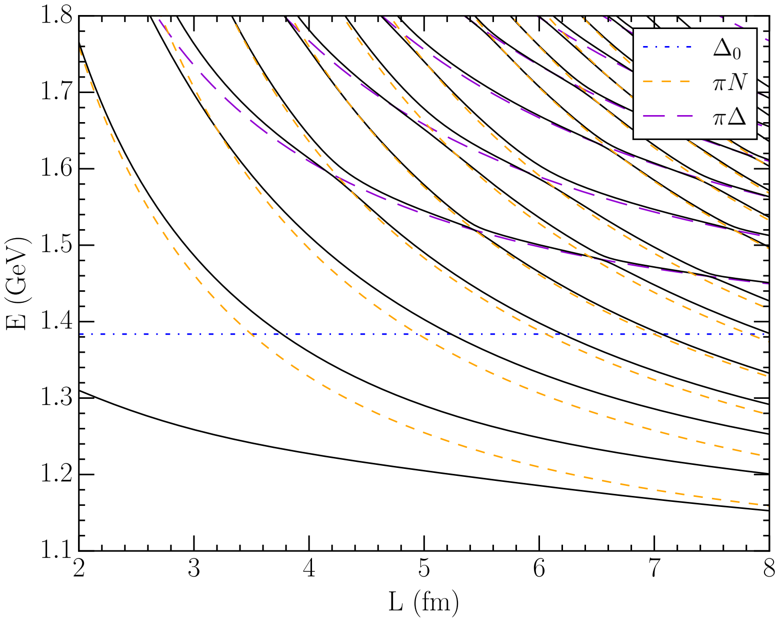

Figure 3.19: Dependence of the energy eigenvalues of the Hamiltonian on the (spatial) lattice size. The solid lines represent the energy eigenvalues following from Fit I of Table 3.1. The (blue) horizontal dot-dashed line is the bare mass. πN scattering states are indicated by dashed orange lines, while long-dashed purple lines are $\pi\Delta$ scattering states.

3.2.2 Finite-Volume Energy Spectrum

Moving to a finite volume, adding a second channel to the matrix Hamiltonian manifests as a additional row and column in the matrix for each allowed momentum. The non-interacting Hamiltonian therefore has the form

$$H_0^{\text{fin}} = \text{diag}\left(m_{\Delta_0},\, \omega_{\pi N}(k_1),\, \omega_{\pi\Delta}(k_1),\, \omega_{\pi N}(k_2),\, \omega_{\pi\Delta}(k_2),\, \ldots,\, \omega_{\pi\Delta}(k_{\text{max}})\right) . \tag{3.38}$$

Similarly, the interaction Hamiltonian for this two-channel system has the matrix form

$$H_{\text{I}}^{\text{fin}} = \begin{pmatrix} 0 & \bar{G}^{\Delta}_{\pi N}(k_1) & \bar{G}^{\Delta}_{\pi\Delta}(k_1) & \bar{G}^{\Delta}_{\pi N}(k_2) & \cdots & \bar{G}^{\Delta}_{\pi\Delta}(k_{\text{max}}) \\ \bar{G}^{\Delta}_{\pi N}(k_1) & \bar{V}_{\pi N\pi N}(k_1,k_1) & \bar{V}_{\pi\Delta\pi N}(k_1,k_1) & \bar{V}_{\pi N\pi N}(k_1,k_2) & \cdots & \bar{V}_{\pi\Delta\pi N}(k_1,k_{\text{max}}) \\ \bar{G}^{\Delta}_{\pi\Delta}(k_1) & \bar{V}_{\pi N\pi\Delta}(k_1,k_1) & \bar{V}_{\pi\Delta\pi\Delta}(k_1,k_1) & \bar{V}_{\pi N\pi\Delta}(k_1,k_2) & \cdots & \bar{V}_{\pi\Delta\pi\Delta}(k_1,k_{\text{max}}) \\ \bar{G}^{\Delta}_{\pi N}(k_2) & \bar{V}_{\pi N\pi N}(k_2,k_1) & \bar{V}_{\pi\Delta\pi N}(k_2,k_1) & \bar{V}_{\pi N\pi N}(k_2,k_2) & \cdots & \bar{V}_{\pi\Delta\pi N}(k_2,k_{\text{max}}) \\ \vdots & \vdots & \vdots & \vdots & \ddots & \vdots \\ \bar{G}^{\Delta}_{\pi N}(k_{\text{max}}) & \bar{V}_{\pi N\pi N}(k_{\text{max}},k_1) & \bar{V}_{\pi\Delta\pi N}(k_{\text{max}},k_1) & \bar{V}_{\pi N\pi N}(k_{\text{max}},k_2) & \cdots & \bar{V}_{\pi\Delta\pi N}(k_{\text{max}},k_{\text{max}}) \\ \bar{G}^{\Delta}_{\pi\Delta}(k_{\text{max}}) & \bar{V}_{\pi N\pi\Delta}(k_{\text{max}},k_1) & \bar{V}_{\pi\Delta\pi\Delta}(k_{\text{max}},k_1) & \bar{V}_{\pi N\pi\Delta}(k_{\text{max}},k_2) & \cdots & \bar{V}_{\pi\Delta\pi\Delta}(k_{\text{max}},k_{\text{max}}) \end{pmatrix} . \tag{3.39}$$

The full finite Hamiltonian is therefore given as $H^{\text{fin}} = H_0^{\text{fin}} + H_{\text{I}}^{\text{fin}}$.

By solving the eigenvalue equation for the finite Hamiltonian at a variety of lattice sizes L, we are able to generate the finite-volume energy spectrum for this system. This is illustrated in Fig. 3.19. As can be seen, below the $\pi\Delta$ threshold, the spectrum is equivalent to the single-channel energy spectrum from Fig. 3.3. Above this threshold, avoided level crossings have become significantly more dramatic, as a result of mixing between πN and $\pi\Delta$ scattering states.

In order to understand how the addition of a $\pi\Delta$ state affects the composition of these eigenstates, we consider the eigenvector composition of the first six eigenvalues in Fig. 3.20. Here, the contributions from all πN are summed into a single curve, where the curve labelled πN for eigenvector $|E_i\rangle$ is given by $\sum_j \langle \pi N(k_j)|E_i\rangle$. The curve labelled $\pi\Delta$ is calculated similarly. As can be seen, the majority of the contributions from $\pi\Delta$ states only apply to the second excited state and higher. This is to be expected, as these eigenstates were well-described by the single-channel system without a $\pi\Delta$ channel. As the density of states increases with L, the number of states below the $\pi\Delta$ threshold is large at $L = 8$ fm. As a result, the majority of the $\pi\Delta$ contributions are focused in the higher excited states, where as an example the seventh excited state is has a 98% contribution from the $|\pi\Delta(k_1)\rangle$ state. For large lattice sizes, the bare basis state component is spread throughout many nearby states, and no one state contains a large majority of the contributions from the bare state.

In order to better view where the states with largest contribution from the bare state lie, in Fig. 3.21 the finite-volume energy spectrum is shown, with the state containing the largest $|\Delta_0\rangle$ component highlighted in red. Despite the large spread of the bare state contributions, the state with the largest bare state eigenvector component is still concentrated around the renormalised mass of the Δ.

As in the single-channel case, we may also extend this formalism to unphysical pion masses, allowing us to compare with lattice QCD results. Here, we take the pion mass extrapolation for the physical Δ in the non-interacting $|\pi\Delta\rangle$ two-particle basis state to be of the same form as for the nucleon, giving

$$m_\Delta(m_\pi^2) = m_\Delta|_{\text{phys}} + \alpha_\Delta \left(m_\pi^2 - m_\pi^2|_{\text{phys}} \right) . \tag{3.40}$$

The mass slope α_Δ is found by fitting this functional form to Δ masses at various pion masses as provided by PACS-CS [47], and fixing the Δ mass at the physical point to 1.232 GeV, giving $\alpha_\Delta = 1.080$ GeV^{-1}. As the mass of the bare basis state is affected by interactions with the $\pi\Delta$ channel, it is likely that the bare mass slope is similarly affected, and therefore we will refit the bare mass slopes, with the method for doing so as described in Sec. 3.1. The bare mass slopes for this system with a 0.8 GeV regulator parameter are given in Table 3.4.

The resultant finite-volume energy spectrum for a varying pion mass with $L = 3$ fm is illustrated in Fig. 3.22, where a comparison of the energy eigenvalues with the basis states is found in the left-most plot, while the spectrum with highlighted contributions from the bare basis state is presented in the right-most plot. Here, we see little variation from the single-channel spectrum, where the ground state contains the largest contribution from the bare basis state, and corresponds with the lattice QCD results for all pion masses.

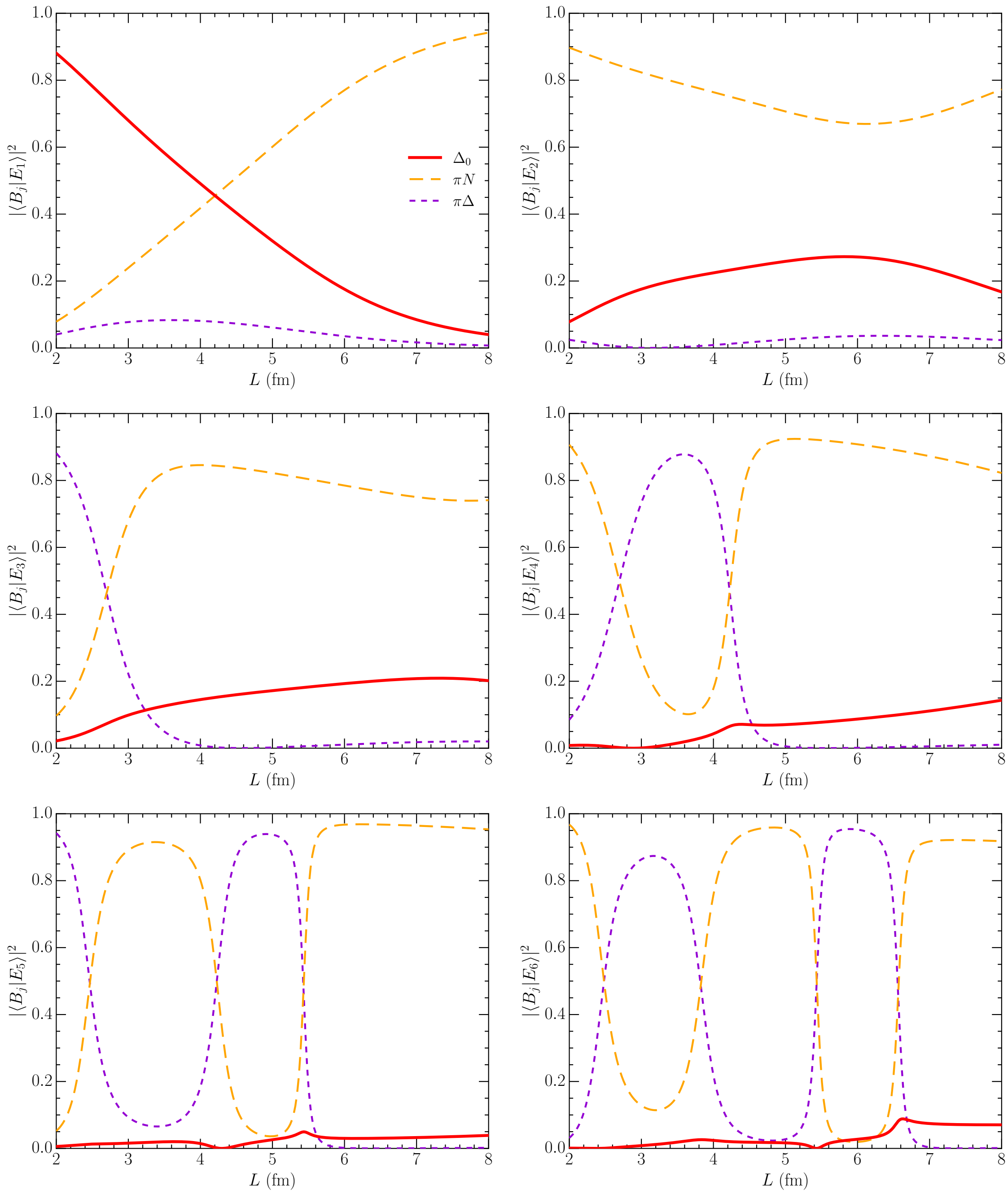

Figure 3.20: Dependence of the eigenvector components for the low-lying energy-eigenstates on the lattice size L. The solid (red) line corresponds with the contribution from the bare basis state. The dashed orange line represents a sum of all πN scattering state eigenvector components, while the long-dashed purple line is the sum of all $\pi\Delta$ scattering state contributions.

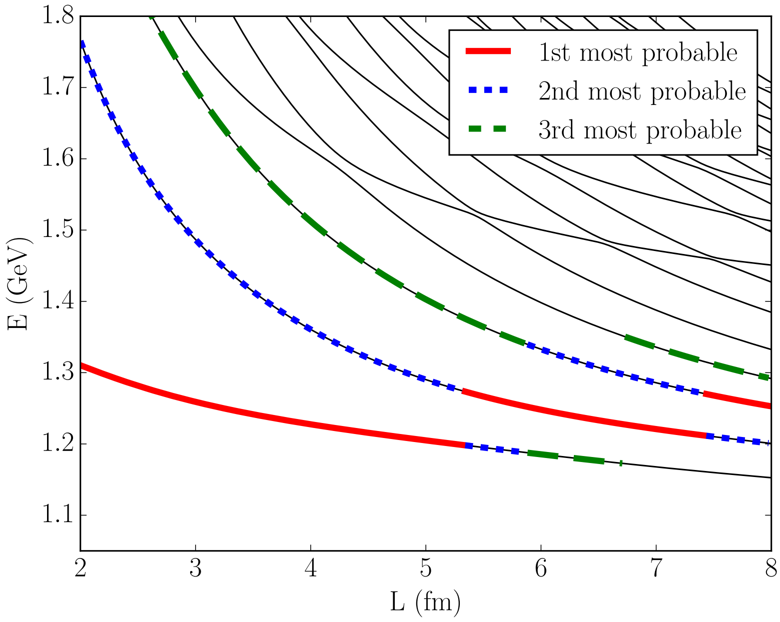

Figure 3.21: Lattice volume dependence of the energy eigenvalues of the Hamiltonian with parameters given by Fit V of Table 3.4. The solid (red), short-dashed (blue) and long-dashed (green) highlights on the eigenvalues correspond to the states with the largest, second-largest and third-largest contribution from the bare basis state $|\Delta_0\rangle$ respectively.

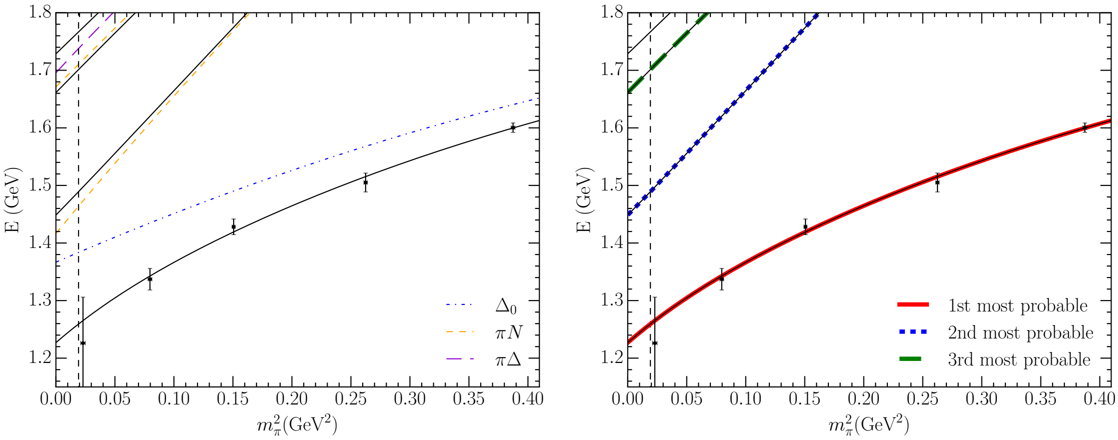

Figure 3.22: Pion mass dependence of the finite-volume HEFT eigenvalues at $L = 2.99$ fm for Fit V given in Table 3.1. The left plot illustrates the shift of the energy eigenvalues from the non-interacting basis states. The right plot is dressed by solid (red), short-dashed (blue) and long-dashed (green) highlights indicating states with the largest, second-largest and third-largest contribution from the bare basis state $|\Delta_0\rangle$ respectively. Lattice QCD results for lowest-lying Δ masses, denoted by the (black) points, are from the PACS-CS collaboration [47]. The vertical dashed (black) line illustrates the physical pion mass.

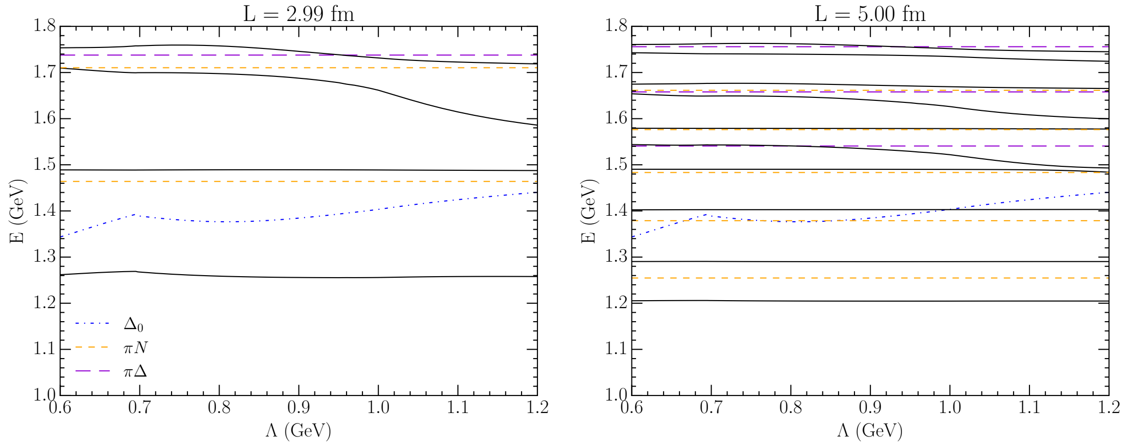

Figure 3.23: Dependence of the lowest lying eigenvalues of the finite-volume Hamiltonian on the regulator parameter Λ for two different lattice sizes, where Λ is varying from 0.6 to 1.2 GeV. The solid (black) lines are the eigenvalues, the horizontal dashed orange and violet lines are $\pi\Delta$ and $\pi\Delta$ basis states, and the curved dot-dashed (blue) line is the mass of the bare Δ_0. The Hamiltonian was constrained to experimental data with $E \leq 1650$ MeV.

3.2.3 Dipole Regulator Dependence

As in the single-channel analysis, we may consider the dependence of the system on the regulator parameter, though we consider a small range of Λ values for the two-channel analysis. As the single-channel analysis indicated that the system is best represented by a phenomenologically motivated value in the vicinity of $\Lambda = 0.8$ GeV, this is not an issue however.

By solving the eigenvalue equation for a range of Λ values between 0.6 and 1.2 GeV, the resultant energy eigenvalues are presented in Fig. 3.23. As can be seen, the two-channel system has considerably more difficulty maintaining model-independence in within the fit regime of $E \leq 1.65$ GeV. At both lattice sizes, there appears to be some Λ-dependence in eigenvalues above 1.5 GeV. In addition, the bare mass as a function of Λ is considerably less smooth than the single-channel system, which manifests in a small Λ-dependence around $\Lambda = 0.7$ GeV for the 3 fm lattice. This model-dependence is attributed to the lack of $\pi\Delta$ scattering data. As the Hamiltonian is constrained by scattering data, a lack of phase shifts associated with $\pi\Delta$ scattering results in a Hamiltonian which is not fully constrained, and therefore some model-dependence manifests. This becomes more clear by considering the Λ-dependence of the eigenvectors for the $L = 2$ fm system, as shown in Fig. 3.24. Considering the eigenvector composition of the ground state, we see that the eigenvector component corresponding with πN scattering states has a smooth regulator parameter dependence, and the feature associated with the Λ-dependence of the ground state near $\Lambda = 0.7$ GeV is not present. This feature is however present in the contributions from $\pi\Delta$ scattering states, and from the bare state, the mass of which is also

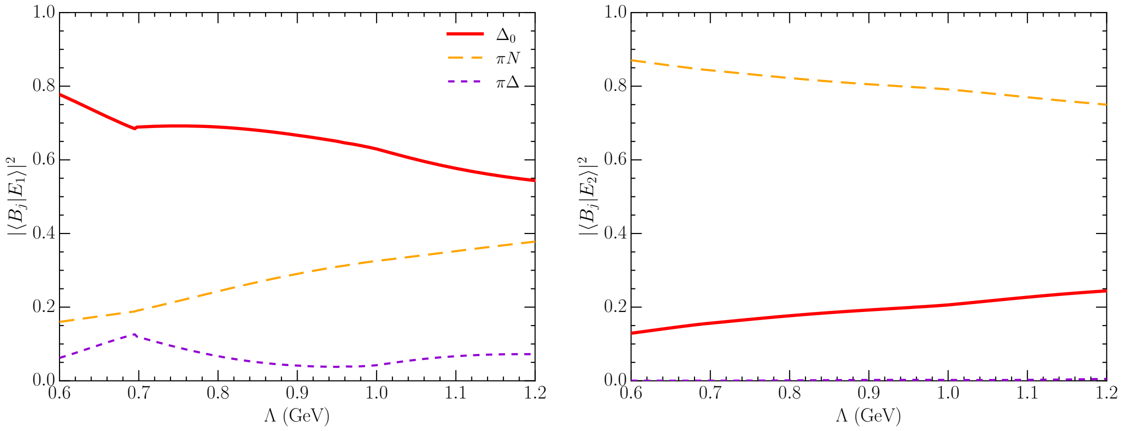

Figure 3.24: Dependence of the energy-eigenstate basis-state structure on the regulator parameter Λ, where Λ is varying from 0.6 to 1.2 GeV, for a lattice size of $L = 2.99$ fm. The two lowest-lying eigenstates are shown, to best illustrate the behaviour of the eigenvector component for the bare basis state.

dependent on $\pi\Delta$ interactions. As such it appears that the model-dependence is arising from the inability to fully constrain $\pi\Delta$ interactions due to the lack of phase shift data.

In principle, this model-dependence may be able to be removed, or minimised by comparing the finite-volume energy eigenvalues from HEFT with lattice QCD. By solving the eigenvalue equation for the Hamiltonian for five values of Λ, and taking a lattice size of $L = 2.99$ fm, the finite-volume energy spectrum as a function of pion mass is presented in Fig. 3.25. For each parameter set, the bare mass slopes have been fit to the PACS-CS data. As can be seen, for this range of Λ there is very little model-dependence in both the ground state, and first excited state, both of which are below the fit threshold of 1.65 GeV. The majority of the model-dependence appears to arise in the second excited state. As such, future high-quality lattice QCD studies which include the excited states of the spectrum may be able to be used to constrain the finite-volume spectrum, preferentially choosing a particular Λ. Only by considering both experimental and lattice QCD data, will one be able to uniquely constrain a Hamiltonian, and therefore find the unique set of eigenvectors which describe the composition of these eigenstates.

3.2.4 Comparison with Contemporary Lattice QCD Results

With both algorithmic advances and increasing computational power, lattice QCD studies of the Δ in the centre-of-mass frame are becoming increasingly accessible. These studies include the presence of momentum-projected five-quark interpolating fields, analogous to the two-particle scattering states from HEFT, and therefore should serve as an excellent source of comparison for HEFT. In particular, we are able to test the ability of the bare state's pion mass extrapolation to describe lattice QCD results on alternative sets of configurations and lattice sizes to PACS-CS. To do so, we consider the recent lattice QCD results from the CLS consortium [63–65].

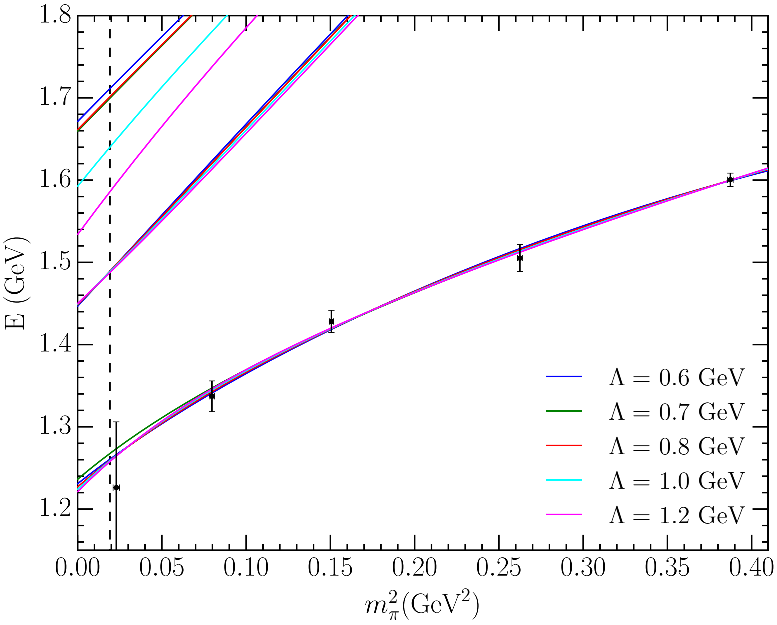

Figure 3.25: Pion mass dependence of the three lowest-lying finite-volume HEFT eigenvalues at $L = 2.99$ fm using a dipole regulator, where the data points are the PACS-CS data. Parameter sets corresponding with each value of Λ are overlaid, each with a corresponding bare mass expansion fit to the PACS-CS data. The four top-left curves correspond with the third eigenvalue for each Λ value. The bare mass expansion is taken to $\mathcal{O}(m_\pi^4)$.

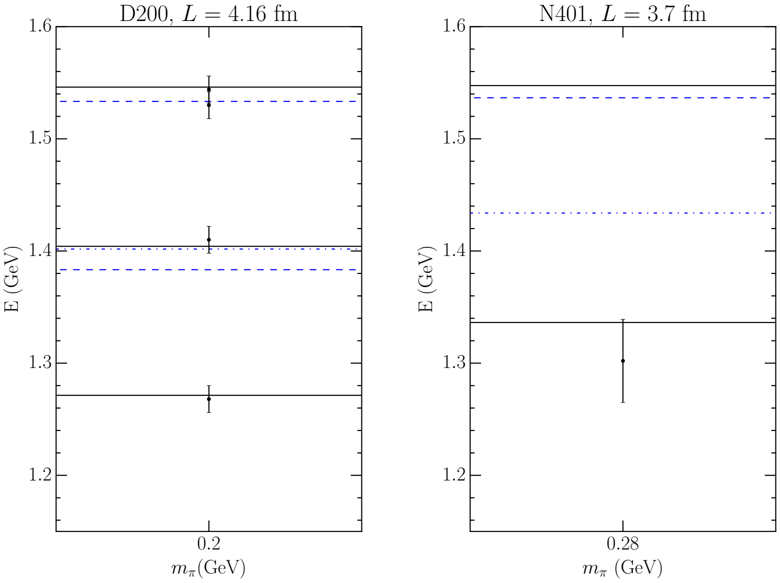

Figure 3.26: Comparison between the energy eigenvalues calculated in HEFT constrained by scattering data and the PACS-CS results for the quark-mass dependence (solid black lines) and lattice QCD data from the CLS consortium (data points) for ensembles D200 (left) [63, 64], and N401 (right) [65]. The dashed blue lines denote non-interacting basis states, while the dot-dashed blue line is the mass of the bare basis state.

The first ensemble, labelled D200, has a pion mass of $m_\pi = 0.2$ GeV and a lattice extent of $L = 4.16$ fm, and reports three low-lying states. Using the parameter set associated with the $\Lambda = 0.8$ GeV regulator parameter, HEFT predicts energy eigenvalues corresponding with each lattice QCD state within one standard deviation. In particular, this is using the pion mass extrapolation for the bare mass as constrained by the PACS-CS data, demonstrating the applicability of the residual series expansion to other ensembles. Considering the eigenvector composition of each of these three energy eigenvalues, the ground state is dominated by contributions from the bare basis state. Meanwhile, the first excited state is composed primarily of contributions from the $|\pi N(k_1)\rangle$ scattering state, which corresponds with the lattice QCD results, where this state couples strongly with the momentum-projected πN interpolating fields. The parameter set associated with $\Lambda = 1.2$ GeV was also compared to the lattice QCD states. As the three lowest-lying eigenstates are Λ-independent at this lattice size and pion mass however, this lattice QCD data is unable to further constrain the Hamiltonian.

Additionally, the CLS consortium also reports a single low-lying state in the ensemble labelled N401, with a pion mass of $m_\pi = 0.28$ GeV and a lattice size of $L = 3.7$ fm. HEFT also produces an energy eigenvalue consistent with this lattice QCD state, with an eigenvector dominated by the bare basis state component. While the lattice QCD data from these ensembles are unable to further constrain the Hamiltonian, they do serve as a demonstration for the ability of the bare state to be constrained by one set of lattice QCD data, and be able to describe other ensembles without additional fitting.

3.3 Conclusion

In this chapter, we have examined the role of finite-range regularisation in Hamiltonian Effective Field Theory, in the context of the single-channel and two-channel $\Delta(1232)$ systems.

In the case of a single πN scattering channel, we are able to use a range of regulator parameters from $\Lambda = 0.6$ to 8.0 GeV, for both dipole and Gaussian regulators, to find a Hamiltonian which is able to fully describe the P_{33} πN scattering data up to the $\pi\Delta$ threshold. This provided a robust demonstration of the model-independence of observables in HEFT, and of how the model-dependence of the eigenvectors of the finite-volume Hamiltonian manifests. Additionally, we were able to demonstrate how only by extending the analysis to unphysical pion masses, and comparing with results from lattice QCD, are we able to show that the $\Delta(1232)$ is not able to be represented by a purely dynamically generated interpretation.

By considering a second scattering channel in the form of a P-wave $\pi\Delta$ channel, we found that the scattering data is best described by phenomenologically motivated regulator parameter values associated with the induced pseudoscalar form factor of the nucleon. Due to the lack of $\pi\Delta$ scattering data to fully constrain the Hamiltonian, the regulator provides a model for the calculation of HEFT quantities above the $\pi\Delta$ threshold. We show that by comparing the finite-volume Hamiltonian predictions with lattice QCD results, we will be able to better constrain the Hamiltonian in the future with the addition of precision excited state lattice QCD results.

Future work investigating the positive-parity Δ spectrum, as well as the nucleon spectrum will require not only new, high-quality lattice QCD data, but also a Hamiltonian containing multiple bare basis states to represent the multitude of resonances in these spectra. As a result, we turn our attention to the investigation of the effects of introducing a second bare basis state to this system in Chapter 4.

4

MULTIPLE BARE STATE DYNAMICS

The content of this chapter served as the source of the publication: Curtis D. Abell, Derek B. Leinweber, Anthony W. Thomas, and Jia-Jun Wu. Effects of multiple single-particle basis states in scattering systems. arXiv:2305.18790[66].

In seeking to find a physical interpretation of the results of lattice QCD, we associate a bare state with a lattice QCD eigenstate which has been excited by a three-quark interpolating field. A particularly important feature of HEFT is the ability to extract the finite-volume eigenvectors of the Hamiltonian, which then provide insight into the structure of energy eigenstates on the lattice and the system as a whole.

Previous studies of baryon resonances utilising HEFT have been limited to Hamiltonians containing only a single bare basis state, and considering only a single resonance in the infinite-volume observables. This has seen considerable success in studies of the $\Delta(1232)$ [29, 34], the Roper $N^*(1440)$ [8, 9], the $\Lambda^*(1405)$ [10], and the $N^*(1535)$ [30]. On the other hand, the spectrum of baryon resonances is considerably more complicated than a single resonance in each partial wave channel, and future studies will require a multiple bare basis state formalism to fully explore the breadth of baryon structure.

In order to investigate the effects of a second bare basis state in both infinite-volume and finite-volume systems, we will consider a simple (”toy model”) extension of the $\Delta(1232)$ system considered in Chapter 3. By limiting the investigation to the extension of a well-studied system, we aim to gain intuition into the behaviour of the position of poles associated with these bare states in infinite volume, as well as the potential changes in the finite-volume energy spectrum.

In this Chapter, we will consider how the addition of a second bare basis state affects both the infinite-volume and finite-volume properties of the system. In Sec. 4.1, we begin with a brief outline of the Hamiltonian used in this chapter. Following that, in Sec. 4.2 we consider how the presence of a second bare state introduces an additional pole in the infinite-volume formalism, and how the original pole position is affected. Finally, Sec. 4.3 considers how the finite-volume energy spectrum changes as the coupling strength to the second bare state is increased. By considering these two situations, we are able to better understand how both finite-volume and infinite-volume systems are affected by a second bare basis state, and develop a unique intuition into the relationship between infinite-volume poles and finite-volume energy eigenstates.

4.1 Hamiltonian Framework

In Chapter 3, we begun by constructing a Hamiltonian with a single bare state, coupled to a single P-wave πN scattering channel. In order to concentrate on the effects of introducing a second bare basis state to the Hamiltonian, without complicated coupled-channel effects, we will utilise an extension of this Hamiltonian, which utilises a dipole regulator. The parameters of this Hamiltonian are given in Table 3.1.

In order to distinguish between the two bare basis states, we re-label the bare mass from the single bare state analysis as m_{Δ_1}, and introduce a second bare basis state with mass m_{Δ_2}. As a result, we may express the free Hamiltonian for this system as

$$H_0 = \sum_{i=1}^{2} |\Delta_i\rangle \, m_{\Delta_i} \, \langle\Delta_i| + \sum_{\alpha} \int d^3k \;\; |\alpha(\boldsymbol{k})\rangle \, \omega_\alpha(\boldsymbol{k}) \, \langle\alpha(\boldsymbol{k})| \, . \tag{4.1}$$

Similarly, the interaction Hamiltonian has the form

$$\begin{aligned} H_{\mathrm{I}} = & \sum_{i=1}^{2} \sum_{\alpha} \int d^3k \left\{ |\Delta_i\rangle \, G_\alpha^{\Delta_i}(\boldsymbol{k}) \, \langle\alpha(\boldsymbol{k})| + |\alpha(\boldsymbol{k})\rangle \, G_\alpha^{\Delta_i \dagger}(\boldsymbol{k}) \, \langle\Delta_i| \right\} \\ & + \sum_{\alpha,\beta} \int d^3k \int d^3k' \;\; |\alpha(\boldsymbol{k})\rangle \, V_{\alpha\beta}(\boldsymbol{k},\boldsymbol{k'}) \, \langle\beta(\boldsymbol{k'})| \, . \end{aligned} \tag{4.2}$$

The strength of the interaction $G_{\pi N}^{\Delta_2}(k)$ is governed by a dimensionless coupling constant, $g_{\pi N}^{\Delta_2}$. Varying the strength of this interaction will be a particular focus of this chapter. We also set the regulator parameter governing the range of this interaction to be equal to that of $G_{\pi N}^{\Delta_1}(k)$, giving $\Lambda_{\pi N}^{\Delta_2} = 0.8$ GeV. As in the single bare state case, this potential is given by

$$G_{\pi N}^{\Delta_i}(k) = \frac{g_{\pi N}^{\Delta_i}}{m_\pi^{\text{phys}}} \, \frac{k}{\sqrt{\omega_\pi(k)}} \, u(k) \, , \tag{4.3}$$

where $u(k)$ is the dipole form factor, and m_π^{phys} the physical pion mass. As the two-to-two background interaction is independent of the bare states, it has the identical form

$$V_{\pi N \pi N}(k,k') = \frac{v_{\pi N \pi N}}{\left(m_\pi^{\text{phys}}\right)^2} \, \frac{k}{\omega_\pi(k)} \, \frac{k'}{\omega_\pi(k')} \, u(k) \, u(k') \, . \tag{4.4}$$

4.2 Two Bare States in Infinite Volume

As we are utilising an extension of the Hamiltonian from Sec. 3.1, we do not require any additional extraction of the observables, as the Hamiltonian is already constrained at the point where $g_{\pi N}^{\Delta_2} = 0$. Of particular interest in this section however, is the how the addition of a second bare basis state affects the position of the original pole, and how a second pole manifests.

In order to extract the pole information, we consider the formalism in Sec. 2.3.2, where bare basis states manifest poles in the matrix propagator $A(E)$. In the two bare state case, this matrix takes the form

$$A(E)^{-1} = \begin{pmatrix} E - m_{\Delta_1} - \bar{\bar{\Sigma}}_{\Delta_1\Delta_1}(E) & -\bar{\bar{\Sigma}}_{\Delta_2\Delta_1}(E) \\ -\bar{\bar{\Sigma}}_{\Delta_1\Delta_2}(E) & E - m_{\Delta_2} - \bar{\bar{\Sigma}}_{\Delta_2\Delta_2}(E) \end{pmatrix} , \tag{4.5}$$

where $\bar{\bar{\Sigma}}_{\Delta_i\Delta_j}$ represents the sum of all self-energy terms involved in the transition from $\Delta_i \to \Delta_j$. In the single bare state case, we are able to find the pole position by searching for complex energy E such that $E - m_{\Delta_1} - \Sigma_{\Delta_1\Delta_1}(E) = 0$. As the propagator for a two bare state system is expressed as an inverse of a 2×2 matrix, we find that the poles in this propagator manifest for complex energies E_i such that $\det\{A(E_i)^{-1}\} = 0$. In the case where $g^{\Delta_2}_{\pi N} = 0$, this matrix reduces to

$$A(E)^{-1} = \begin{pmatrix} E - m_{\Delta_1} - \bar{\bar{\Sigma}}_{\Delta_1\Delta_1}(E) & 0 \\ 0 & E - m_{\Delta_2} \end{pmatrix} . \tag{4.6}$$

Calculating the determinant of this matrix, we obtain a pole at the original single bare state position, $E_{\text{pole}} = 1.211 - 0.049\,i$ GeV, and a second pole at $E = m_{\Delta_2}$. As this does not provide any insightful information, we are interested in the case where $g^{\Delta_2}_{\pi N} \neq 0$. By smoothly turning on the coupling $g^{\Delta_2}_{\pi N}$, while holding all other parameters fixed, we are able to observe how the system is affected, and in particular how the position of the poles is affected. While this process does move away from the physical description of the $\Delta(1232)$ and we no longer have a good description of the scattering data, this instead allows us analyse exactly how the system is affected through the introduction of a second bare state.

In doing, so we consider two situations. In the first, we introduce a second bare state with a larger bare mass. This is likely to be the most common situation, where now we attempt to introduce bare basis states to represent excited states with a possible three-quark core. In the second situation, we introduce a second bare basis state with a mass lower than the first bare state. This may prove useful for studies of systems such as the Roper resonance, where a previous HEFT study found that a bare mass of 2.0 GeV was required to describe the finite-volume energy spectrum [9]. It is possible that this analysis may be improved by the addition of a lower mass bare basis state representing the bare nucleon.

4.2.1 Large Second Bare Mass

Considering this first system, we introduce a second bare state with a mass $m_{\Delta_2} = 1.6$ GeV. Initially, the presence of this bare state with no coupling simply introduces a pole in the T-matrix on the real axis, at 1.6 GeV. As the coupling $g^{\Delta_2}_{\pi N}$ is turned on, this non-

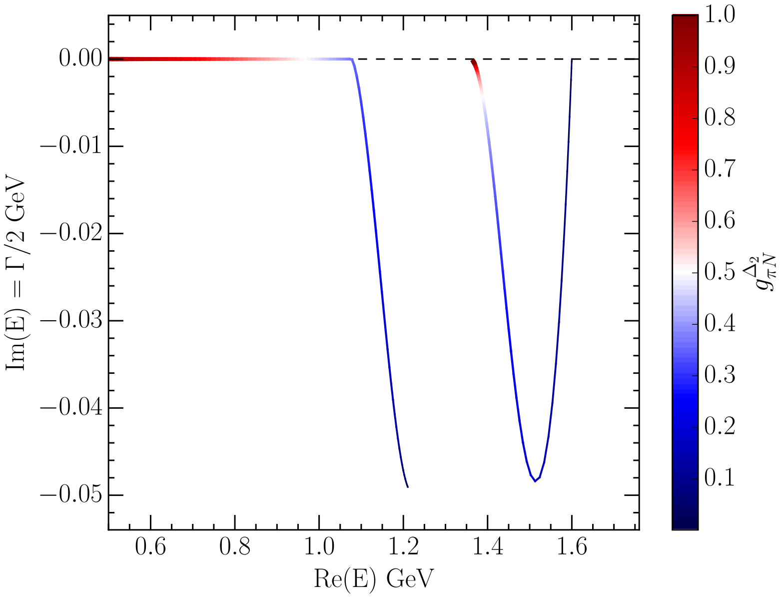

Figure 4.1: Variation of the T-matrix poles as the coupling, $g_{\pi N}^{\Delta_2}$, of a second bare basis state to πN scattering states is increased. The thin (blue) points represent the pole positions in the complex place for small $g_{\pi N}^{\Delta_2}$, moving to thicker (red) points for a larger coupling. Here, the mass of the second bare basis state, Δ_2, is 1.6 GeV, relative to Δ_1 at 1.359 GeV.

interacting bound state gains a negative imaginary component, becoming a resonance as it decays to πN. This process is demonstrated in Fig. 4.1, where we are smoothly increasing $g_{\pi N}^{\Delta_2}$ up to a value of 1.0, showing the movement of the new pole we have introduced, as well as the movement of the original pole representing the physical $\Delta(1232)$.

While initially located near the position of the physical Δ baryon, as $g_{\pi N}^{\Delta_2}$ increases the original pole rapidly tends to the real axis, while the second pole initially develops a larger imaginary component. In the regime where $g_{\pi N}^{\Delta_1}$ and $g_{\pi N}^{\Delta_2}$ are of similar order, the two poles are both distinct and have reasonable widths. Interestingly, the turning point in the position of the second pole occurs when $g_{\pi N}^{\Delta_1} = g_{\pi N}^{\Delta_2}$. As the coupling of the second bare state begins moving to a value larger than that of the first, both poles tend towards the real axis.

Once the coupling of the second bare state has become approximately double that of the first, we find that the initial pole drops to a mass below the πN threshold, becoming a bound state. As this occurs, the pole corresponding to the second bare state also continues its trajectory towards the real axis. Unlike the first pole however, as the second coupling increases, this pole only approaches the real axis, never becoming a bound state. As the imaginary component of this pole approaches zero, the real component approaches the mass of the first bare state, at 1.359 GeV. This intriguing result hints at an exchange in the composition of the physical states. For small coupling, Δ_2 is associated with the second pole, but at large coupling it is associated with the first pole, leaving the second pole to be governed by Δ_1.

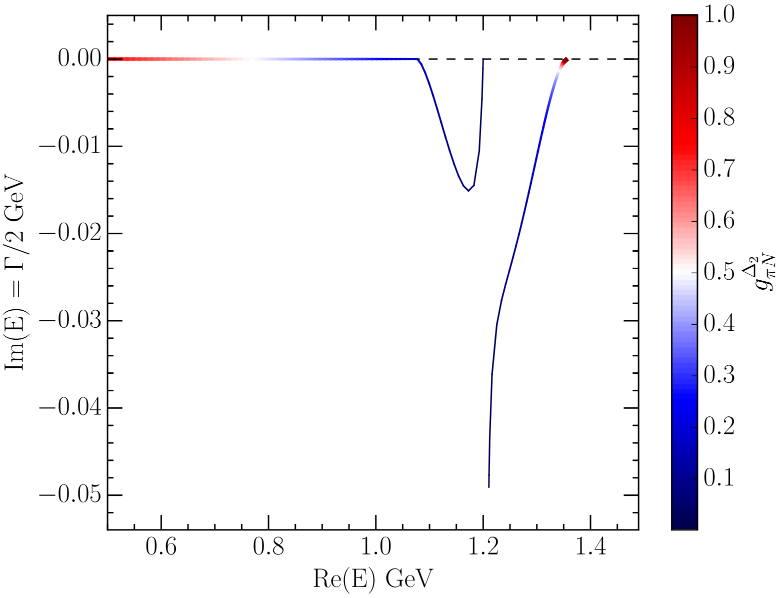

Figure 4.2: Variation of the T-matrix poles as the coupling, $g_{\pi N}^{\Delta_2}$, of a second bare state to πN scattering states is increased. The thin (blue) points represent the pole positions in the complex place for small $g_{\pi N}^{\Delta_2}$, moving to thicker (red) points for a larger coupling. Here, the mass of the second bare basis state, Δ_2, is 1.2 GeV, relative to Δ_1 at 1.359 GeV.

For studies involving multiple bare states, this pole movement implies that couplings between each bare state and scattering states, such as $g_{\pi N}^{\Delta_1}$ and $g_{\pi N}^{\Delta_2}$, should be of similar order to avoid the generation of unphysical poles and bound states. It is only in this regime that the widths of each resonance correspond with typical particle widths observed in physical resonances. In this final state, where $g_{\pi N}^{\Delta_2}$ is an order of magnitude larger than $g_{\pi N}^{\Delta_1}$, the system is completely dominated by $|\Delta_2\rangle$, and our system is unable to give a good description of resonance physics.

4.2.2 Small Second Bare Mass

As a second scenario we consider the addition of a second bare state with a mass lower than the original $m_{\Delta_1} = 1.359$ GeV. In particular, we choose this mass to be $m_{\Delta_2} = 1.2$ GeV, as this lies approximately half way between the first bare mass and the πN threshold, giving the clearest demonstration of novel behaviour. While the introduction of a second bare state at $m_{\Delta_2} = 1.6$ GeV caused the original pole to move towards a bound state below the πN threshold, introducing a second bare state with a mass less than the first has the opposite effect, as seen in Fig. 4.2. In this system, the initial behaviour is the same as the previous case, where we have a pole at the physical $\Delta(1232)$ position, and a second pole bound at $m_{\Delta_2} = 1.2$ GeV. As $g_{\pi N}^{\Delta_2}$ increases in the same manner as Sec. 4.2.1, where all other couplings are held fixed, the second pole initially behaves in the same manner, moving away from the real axis as it decays to πN. The turning point occurs at

$g_{\pi N}^{\Delta_1} = g_{\pi N}^{\Delta_2}$. From here, however, it is the new second pole which continues to the πN threshold, before becoming bound below this threshold. The initial pole, which starts at the position of the physical $\Delta(1232)$, instead tends towards the real axis, at the position of the original bare state at $m_{\Delta_1} = 1.359$ GeV.

For large coupling of Δ_2 to the πN scattering states, the system consists of a bound state below the πN threshold, and a long-lived state at the position of the original bare mass While the large-coupling behaviour of the two poles is the same regardless of the second bare state's mass, the path taken is reversed for the two situations considered. This highlights the complexity of a system with multiple bare states, and the difficulty in identifying the origin of poles emerging from the interactions between multiple bare states.

While initially we have a pole which is identified as the physical $\Delta(1232)$ baryon, the introduction of a second bare state introduces a degree of ambiguity as to the origin and composition of the resultant poles, depending on the mass of the second bare state. In order to gain a better understanding of the structure of these poles, as well as the behaviour of the system as the second bare state is introduced, we now turn our attention to finite-volume physics.

4.3 Two Bare States in a Finite Volume

Considering finite-volume physics allows one to gain additional insight into the behaviour and composition of the scattering states, through analysis of the Hamiltonian eigenvalues and eigenvectors respectively. Using the same systems as in Sec. 4.2, we consider how the finite-volume spectrum is affected by the introduction of a second bare state. Initially, with the second bare state turned off, the finite-volume energy spectrum is equivalent to the single-channel analysis in Sec. 3.1.2, as well as with finite-volume energies calculated from Lüscher's method. For this study, we choose to concentrate on a lattice extent of $L = 3$ fm, giving a sufficient density of states to demonstrate the behaviour of the spectrum.

With the addition of a second bare basis state, the discretisation of the free Hamiltonian from Eq. (4.1) and the interaction Hamiltonian from Eq. (4.2) results in a simple addition of a row and column to the finite-volume Hamiltonian matrix. As a result the free Hamiltonian has the finite form

$$H_0^{\text{fin}} = \text{diag}\left(m_{\Delta_1},\, m_{\Delta_2},\, \omega_{\pi N}(k_1),\, \omega_{\pi N}(k_2),\, \cdots ,\, \omega_{\pi N}(k_{\text{max}})\right) . \tag{4.7}$$

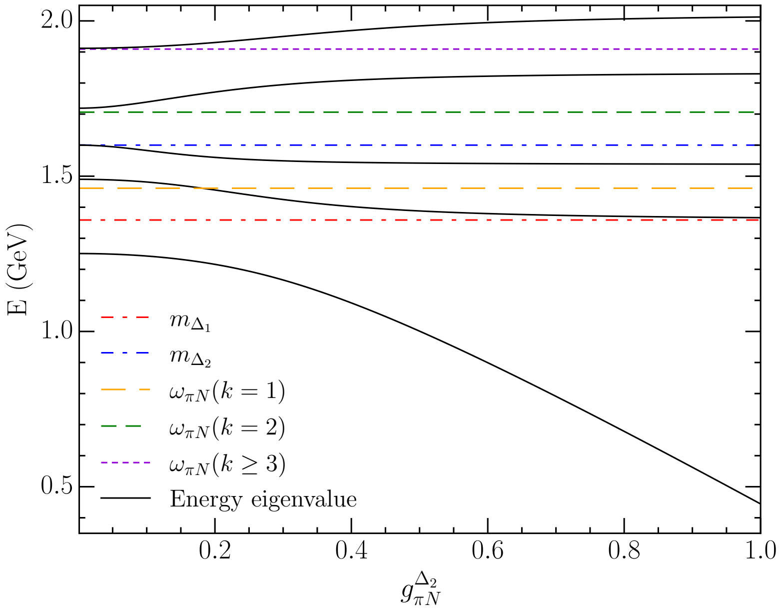

Figure 4.3: Dependence of the $L = 3$ fm finite-volume Hamiltonian energy eigenvalues on the coupling of the second bare basis state to πN scattering states, labelled $g_{\pi N}^{\Delta_2}$. Here, the mass of the second bare basis state, Δ_2, is 1.6 GeV, relative to Δ_1 at 1.359 GeV.

Similarly, the finite matrix form of the interaction Hamiltonian is written as

$$H_{\rm I}^{\rm fin} = \begin{pmatrix} 0 & 0 & \overline{G}_{\pi N}^{\Delta_1}(k_1) & \overline{G}_{\pi N}^{\Delta_1}(k_2) & \cdots \\ 0 & 0 & \overline{G}_{\pi N}^{\Delta_2}(k_1) & \overline{G}_{\pi N}^{\Delta_2}(k_2) & \cdots \\ \overline{G}_{\pi N}^{\Delta_1}(k_1) & \overline{G}_{\pi N}^{\Delta_2}(k_1) & \overline{V}_{\pi N \pi N}(k_1,k_1) & \overline{V}_{\pi N \pi N}(k_1,k_2) & \cdots \\ \overline{G}_{\pi N}^{\Delta_1}(k_2) & \overline{G}_{\pi N}^{\Delta_2}(k_2) & \overline{V}_{\pi N \pi N}(k_2,k_1) & \overline{V}_{\pi N \pi N}(k_2,k_2) & \cdots \\ \vdots & \vdots & \vdots & \vdots & \ddots \\ \overline{G}_{\pi N}^{\Delta_1}(k_{\rm max}) & \overline{G}_{\pi N}^{\Delta_2}(k_{\rm max}) & \overline{V}_{\pi N \pi N}(k_{\rm max},k_1) & \overline{V}_{\pi N \pi N}(k_{\rm max},k_2) & \cdots \end{pmatrix} . \tag{4.8}$$

Using standard eigenvalue equation numerical methods for the full Hamiltonian $H^{\rm fin} = H_0^{\rm fin} + H_{\rm I}^{\rm fin}$, we are able to obtain the energy eigenvalues, labelled E_i. Additionally, we obtain the eigenvectors, which we label $\langle B_j | E_i \rangle$. This represents the contribution from each basis state $|B_j\rangle$, to an energy eigenstate $|E_i\rangle$.

As in Sec. 4.2, we consider the two situations of a larger second bare mass, and a lighter second bare mass. By comparing the results of these finite-volume spectra to the infinite-volume poles, we are able to develop a unique intuition into the relationships between these two representations of the system.

4.3.1 Large Second Bare Mass

With the addition of a second bare basis state with mass $m_{\Delta_2} = 1.6$ GeV, the finite-volume spectrum shown in Fig. 4.3 displays similar behaviour to the poles in Fig. 4.1.

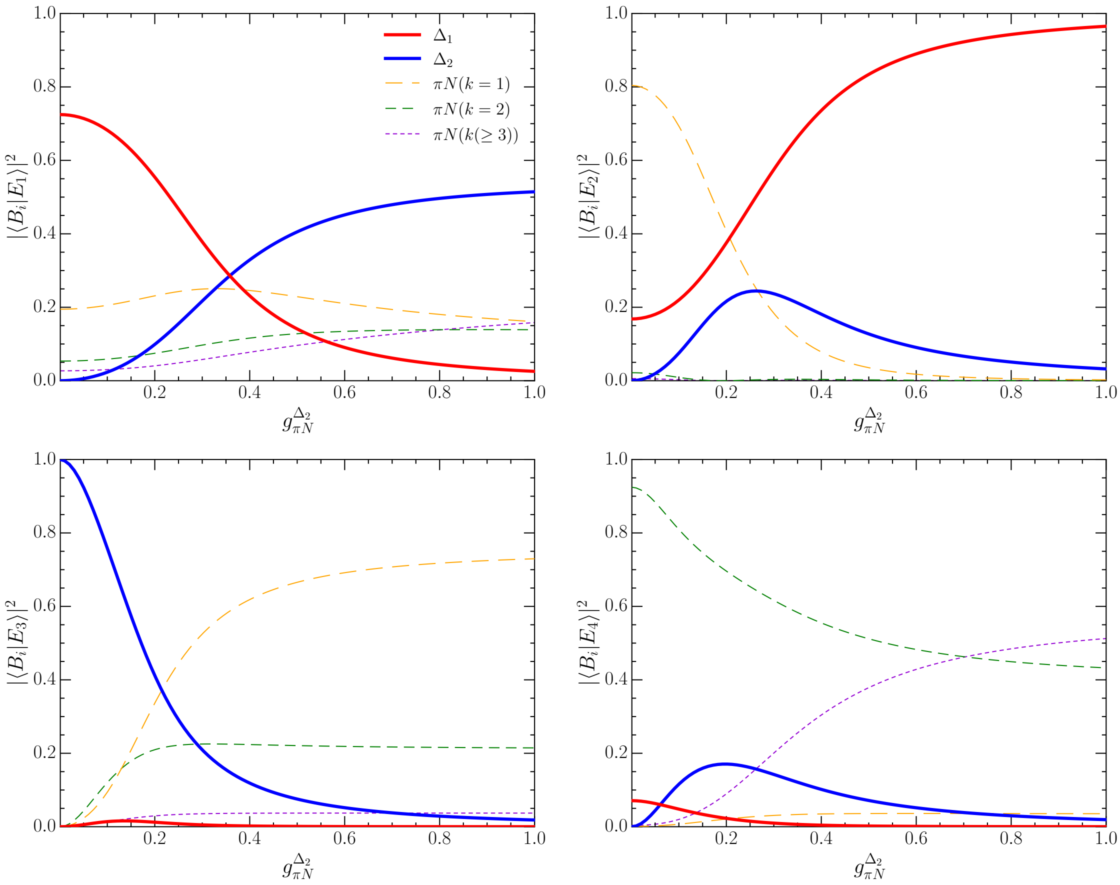

Figure 4.4: Dependence of the finite-volume energy-eigenstate basis state structure on the coupling $g_{\pi N}^{\Delta_2}$, for $L = 3$ fm, where $m_{\Delta_2} = 1.6$ GeV. The label $|\langle B_i|E_j\rangle|^2$ denotes the contribution from each basis state $|B_i\rangle$ to the energy eigenvalues $|E_j\rangle$ from Fig. 4.3. Eigenvector components from higher momentum scattering states are summed in $\pi N(k \geq 3)$.

Here, the third eigenvalue is initially identified at the position of the second bare mass, with no shift away from the non-interacting energy level. As the coupling $g_{\pi N}^{\Delta_2}$ is increased, this eigenvalue shifts away from the non-interacting bare state at 1.6 GeV, before encountering an avoided level crossing with the second eigenvalue. This movement trend then continues on with the second eigenvalue, approaching the value of the lower-lying bare mass at 1.359 GeV. Also similar to the pole movement in Fig. 4.1, the lowest-lying energy eigenvalue shifts from a state near the position of the physical $\Delta(1232)$, to a bound state with energy less than the πN threshold, at $m_\pi + m_N \approx 1.08$ GeV.

An advantage of HEFT is the ability to extract the eigenvectors of the Hamiltonian, and gain insight into the contribution from basis states towards each eigenstate. The dependence of the state composition on $g_{\pi N}^{\Delta_2}$ is shown in Fig. 4.4. Here we observe that, as the coupling to the second bare state increases, the interpretation of each eigenstate changes. Initially, the ground state is dominated by contributions from the first bare state, while the second bare state contributions dominate the third eigenstate located at the mass of the second bare state. As the coupling increases however, the state dominated by the

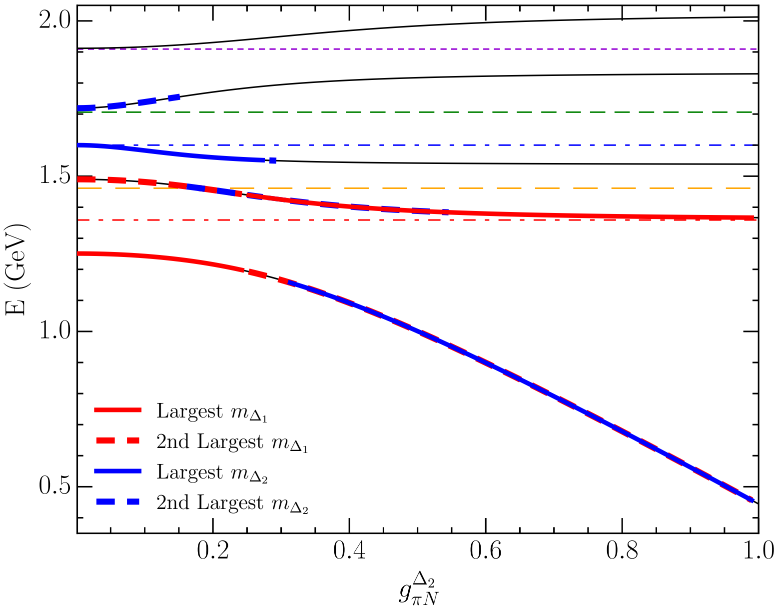

Figure 4.5: Dependence of the $L = 3$ fm finite-volume Hamiltonian energy eigenvalues on the coupling of the second bare basis state to πN scattering states, labelled $g^{\Delta_2}_{\pi N}$. Here, the mass of the second bare basis state, Δ_2, is 1.6 GeV, relative to Δ_1 at 1.359 GeV. Red and blue highlighting represents the states with largest eigenvector components from the first and second bare basis states respectively. Basis states are styled as in Fig. 4.3.

second bare state quickly moves to lower energy, moving to the ground state for a coupling of $g^{\Delta_2}_{\pi N} \sim 0.4$. It is only in the regime where $g^{\Delta_1}_{\pi N} = g^{\Delta_2}_{\pi N}$ that contributions from each bare state are spread through the tower of excited states. At all coupling strengths we are able to distinctly identify a state in which the majority of contribution from a bare state is present. Such a state is one which we expect to observe in the spectrum of lattice QCD generated by three-quark interpolating fields.

In order to better observe this distribution of contributions from each bare state, in Fig. 4.5 we display the spectrum from Fig. 4.3 with additional information from the eigenvectors plotted, where the states with the first and second largest contributions from each bare state have been highlighted. Using this scheme, it becomes clear how the position of the eigenstate dominated by each bare basis state moves as a function of $g^{\Delta_2}_{\pi N}$. In particular, we are able to gain additional insight that is not obvious in the infinite-volume analysis.

While the behaviour of the eigenvalues matches the behaviour of the poles in Sec. 4.2.1, the behaviour of the eigenvectors tells a new story. At small coupling, Δ_2 is associated with the third energy eigenstate. However we see that it is the ground state which possesses the majority of $|\Delta_2\rangle$ at large coupling. Thus Δ_2 generates the lower lying pole at large coupling. The exchange in the bare-state roles is made possible as Δ_1 becomes associated with the second energy eigenstate. At approximately $g^{\Delta_1}_{\pi N} = g^{\Delta_2}_{\pi N}$, the identities of the three energy eigenstates are shuffled.

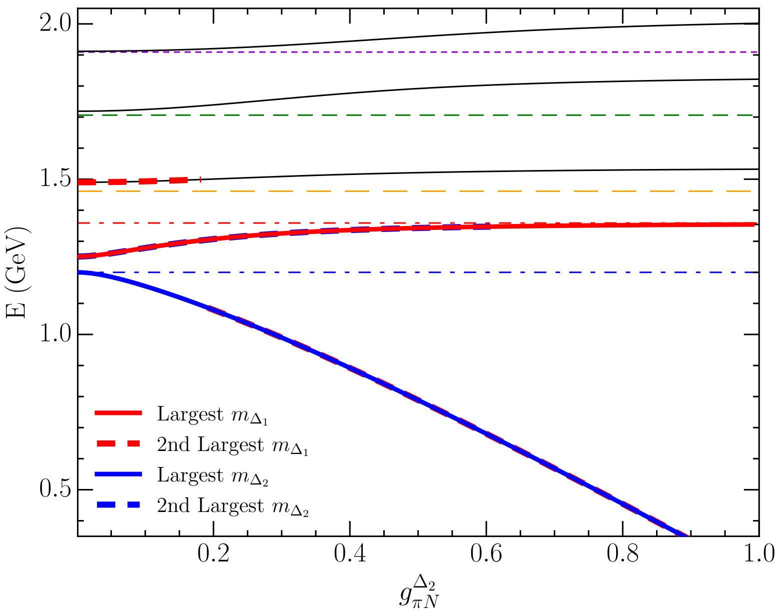

Figure 4.6: Dependence of the $L = 3$ fm finite-volume Hamiltonian energy eigenvalues on the coupling of the second bare basis state to πN scattering states, labelled $g_{\pi N}^{\Delta_2}$. Here, the mass of the second bare basis state, Δ_2, is 1.2 GeV, relative to Δ_1 at 1.359 GeV. Red and blue highlighting represents the states with largest eigenvector components from the first and second bare basis states respectively. Basis states are styled as in Fig. 4.3.

4.3.2 Small Second Bare Mass

By constructing a finite-volume Hamiltonian that includes a second bare mass with $m_{\Delta_2} = 1.2$ GeV, lying below $m_{\Delta_1} = 1.359$ GeV, we are able to investigate whether the behaviour of the finite-volume eigenstates corresponds with the behaviour of the poles associated with each bare state as seen in Sec. 4.2.2. The resultant finite-volume energy spectrum as a function of the coupling of the 1.2 GeV bare state to πN scattering states is illustrated in Fig. 4.6. In addition, the eigenstates with largest eigenvector components from each of the two bare states are highlighted in red and blue. The eigenvector composition of the four lowest-lying eigenstates as a function of $g_{\pi N}^{\Delta_2}$ are given in Fig. 4.7.

Considering the energy spectrum, we observe a similar behaviour to that corresponding to the pole movement discussed in Sec. 4.2.2. The state which initially describes the physical Δ, represented by a pole at $1.210 - 0.050\,i$ GeV in an infinite volume, and by a solid red line in the finite-volume spectrum, moves from its initial position to the position of the first bare mass, at 1.359 GeV. As this happens, the state becomes increasingly dominated by the contribution from the first bare state. At a coupling of $g_{\pi N}^{\Delta_2} = 1$, 97% of the eigenvector component for the first bare state resides in this eigenstate.

As this occurs, the ground state, which initially is the uncoupled light bare state, begins to mix with contributions from both πN scattering states and the original bare state. This rapidly reduces the value of the energy eigenvalue, corresponding with the movement of

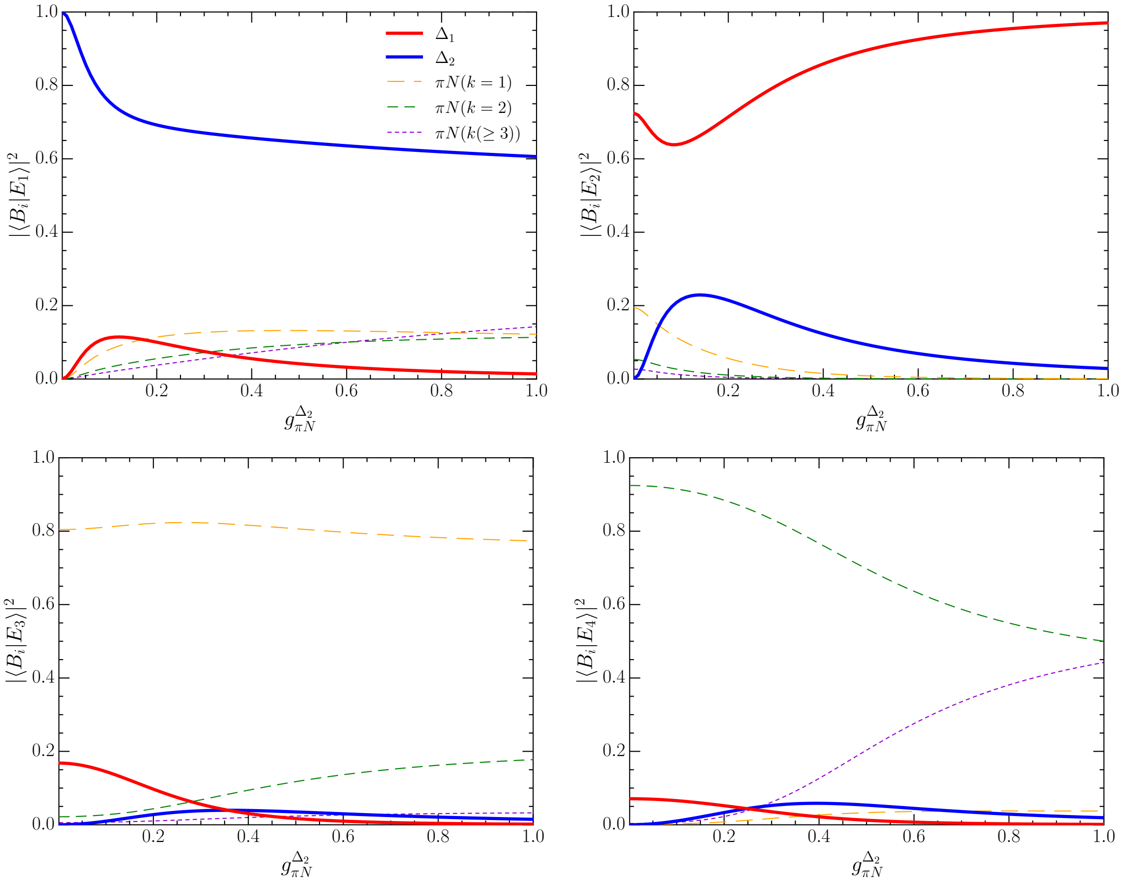

Figure 4.7: Dependence of the finite-volume energy-eigenstate basis state structure on the coupling $g_{\pi N}^{\Delta_2}$, for $L = 3$ fm, where $m_{\Delta_2} = 1.2$ GeV. The label $|\langle B_i|E_j\rangle|^2$ denotes the contribution from each basis state $|B_i\rangle$ to the energy eigenvalues $|E_j\rangle$ from Fig. 4.6. Eigenvector components from higher momentum scattering states are summed in $\pi N(k \geq 3)$.

the pole in an infinite-volume, where it rapidly drops below the πN threshold, becoming a bound state. Considering the eigenvector composition of this state however, this reducing energy appears to be due to an increasing contribution in higher-momentum πN scattering states.

Interestingly, the turning point observed in the pole movement, at $g_{\pi N}^{\Delta_1} = g_{\pi N}^{\Delta_2}$, is also observed in the eigenvectors for the two lowest-lying eigenstates for similarly sized values of $g_{\pi N}^{\Delta_2}$, further demonstrating the similar behaviour of the movement of poles in an infinite volume with the eigenvector composition of eigenstates in a finite volume.

4.4 Conclusion

In Chapter 4, we have introduced a second bare baryon basis state to the single-channel system from Chapter 3. By calculating the positions of poles in the S-matrix, we observed how the original pole positions are affected by the introduction of a second bare state, and found that large couplings result in the generation of unphysical bound states.

By investigating how the eigenvectors of the finite-volume Hamiltonian vary according to the introduction of a second bare state, we found that their behaviour follows that of the poles, providing unique insight into the relationship between finite-volume and infinite-volume physics.

Given the intuition this chapter has provided into the role of a second bare basis state in HEFT, we are well-equipped to consider a physical system which is of interest in contemporary physics. An excellent candidate system is that of the two low-lying odd-parity nucleon resonances, found in S_{11} πN scattering. Using the understanding developed in this study, we will consider this new system in Chapter 5.

5

ODD-PARITY NUCLEON RESONANCES

The content of this chapter served as the source of the publication: Curtis D. Abell, Derek B. Leinweber, Zhan-Wei Liu, Anthony W. Thomas, and Jia-Jun Wu. Low-lying odd-parity nucleon resonances as quark-model like states. arXiv:2306.00337[67].

An analysis of the nature of pion-nucleon resonances is a vital component of the quest to understand the nature of non-perturbative QCD. The low-lying odd-parity nucleon resonances, the $N^*(1535)$ and $N^*(1650)$, are a subject of particular interest, as the $N^*(1535)$ sits above the first positive-parity excitation of the nucleon, the $N^*(1440)$ (Roper resonance), contrary to simple quark-model predictions. However there is now evidence for the Roper resonance as primarily being dynamically generated by strong πN and $\pi\pi N$ rescattering, with only a small bare state contribution [8, 9, 68, 69]. The nature of the odd-parity nucleons however is less clear. Both interpretations as being dynamically generated [70, 71], and as being primarily a three-quark state dressed by πN and ηN interactions [30] have been argued.

Lattice QCD offers an alternate source of insight into the nature of these resonances, providing a first-principles approach to the nuances of hadron spectroscopy. In particular, a recent lattice QCD study [72] of the odd-parity nucleon states near these resonances found their magnetic moments resemble constituent-quark-model predictions. As such, a consideration of the $N^*(1535)$ and $N^*(1650)$ as single-particle three-quark states dressed by meson-baryon interactions is now well-motivated.

In this chapter, we will consider the case where the two low-lying odd-parity nucleon resonances may be represented by two bare basis states in the Hamiltonian formalism, $|N_1\rangle$ and $|N_2\rangle$, with masses m_{N_1} and m_{N_2} respectively. These two bare states will be allowed to couple with S-wave πN, ηN, and $K\Lambda$ scattering channels, and therefore we refer to this Hamiltonian as a two bare state, three channel (2b3c) system.

In Sec. 5.1, we will begin by constructing the infinite-volume Hamiltonian and solving the coupled-channel scattering equations, providing the phase shifts and inelasticities for this system. This will allow us to constrain the free parameters of the Hamiltonian to S_{11} scattering data, and predict the positions of poles in the scattering amplitude.

Sec. 5.2, makes a connection with lattice QCD at $L \sim 3$ fm, where the pion mass dependence of the bare basis states is constrained. This allows us to study the structure of energy eigenstates observed in lattice QCD calculations. By associating the lattice eigenstates with HEFT energy eigenstates, we are able to analyse their eigenvector composition and gain insight into their structure.

In Sec. 5.3, predictions are made for the finite-volume energy spectrum at $L \sim 2$ fm, using constraints from the $L \sim 3$ fm analysis. An eigenvector analysis is performed for the states to illustrate their composition. An analysis is performed for an $L \sim 4$ fm lattice in Sec. 5.4, where recent lattice QCD results from the CLS consortium [64] are compared with HEFT. Remarkably, the lattice QCD results are described with excellent precision.

Finally, Sec. 5.5 introduces a novel method for simulating the scattering state contaminations in lattice QCD correlation functions constructed with standard three-quark operators. The contamination functions are constructed with both HEFT eigenvectors, and lattice QCD correlation matrix eigenvectors, with remarkable agreement between them. We also consider the interplay between contamination due to two-particle scattering-state contributions and nearby eigenstates with significant single-particle components.

5.1 Infinite-Volume Scattering

In order to constrain the free parameters in the Hamiltonian, we consider the S_{11} pion-nucleon scattering data from the SAID WI08 solution [54, 55]. Following the previous HEFT study of the $N^*(1535)$ [30], we adopt a dipole form factor for our regulator, given by

$$u(k) = \left(1 + \frac{k^2}{\Lambda^2}\right)^{-2} , \tag{5.1}$$

where we allow Λ to take unique values for each scattering channel. In order to describe the scattering data, we require parametrisations of the two types of interactions considered in the Hamiltonian. Motivated from heavy-baryon χPT, the S-wave interaction between a bare state $|N_i\rangle$ and a scattering state $|\alpha(k)\rangle$ is given by

$$G_\alpha^{N_i}(k) = \frac{\sqrt{3}}{2\pi f_\pi}\, g_\alpha^{N_i}\, \sqrt{\omega_{\alpha_{\mathrm{M}}}(k)}\, u(k) , \tag{5.2}$$

where $f_\pi = 92.4$ MeV is the pion decay constant, and $g_\alpha^{N_i}$ is the dimensionless coupling strength for this interaction. Additionally, $\omega_{\alpha_{\mathrm{M}}}(k) = \sqrt{k^2 + m_{\alpha_{\mathrm{M}}}^2}$ is the mass-energy of the meson in channel $|\alpha\rangle$. Considering the two-to-two interaction, between scattering states $|\alpha(k)\rangle$ and $|\beta(k')\rangle$, we use the standard S-wave parametrisation

$$V_{\alpha\beta}(k, k') = \frac{3}{4\pi^2 f_\pi^2}\, v_{\alpha\beta}\, \tilde{u}(k)\, \tilde{u}(k') , \tag{5.3}$$

where $v_{\alpha\beta}$ is the dimensionless coupling strength between the two scattering channels. As in Ref. [30], we found considerable difficulty in describing the S-wave scattering data at low energies. As such, we also modify the regulator for the two-to-two potential to enhance the interaction strength at low energies. This modified form factor has the form

$$\tilde{u}(k) = \frac{\omega_\pi(k) + m_\pi^{\mathrm{phys}}}{\omega_\pi(k)}\, u(k) . \tag{5.4}$$

Table 5.1: HEFT fit parameters constrained by the WI08 solution [54, 55] for S_{11} scattering, up to 1.75 GeV.

Parameter	Value	Parameter	Value
m_{N_1} / GeV	1.6301	m_{N_2} / GeV	1.8612
$g^{N_1}_{\pi N}$	0.0898	$g^{N_2}_{\pi N}$	0.2181
$g^{N_1}_{\eta N}$	0.1525	$g^{N_2}_{\eta N}$	0.0009
$g^{N_1}_{K\Lambda}$	0.0000	$g^{N_2}_{K\Lambda}$	-0.2367
$\Lambda^{N_1}_{\pi N}$ / GeV	1.2335	$\Lambda^{N_2}_{\pi N}$ / GeV	1.4000
$\Lambda^{N_1}_{\eta N}$ / GeV	1.2642	$\Lambda^{N_2}_{\eta N}$ / GeV	0.9521
$\Lambda^{N_1}_{K\Lambda}$ / GeV	$\cdots$	$\Lambda^{N_2}_{K\Lambda}$ / GeV	0.7283
$v_{\pi N,\pi N}$	-0.0655	$v_{\eta N,\eta N}$	-0.0245
$v_{\pi N,\eta N}$	0.0388	$v_{\eta N,K\Lambda}$	0.0320
$v_{\pi N,K\Lambda}$	-0.0757	$v_{K\Lambda,K\Lambda}$	0.1371
$\Lambda_{v,\pi N}$ / GeV	0.6000	$\Lambda_{v,\eta N}$ / GeV	0.9036
$\Lambda_{v,K\Lambda}$ / GeV	0.6060		

Here, For $k \approx 0$, this expression results in $\tilde{u}(k) \approx 2\,u(k)$, enhancing the low-energy potential. As the momentum of the back-to-back states increases, this expression increasingly tends to the original regulator $u(k)$.

Utilising these potentials, we are able to solve the coupled-channel scattering equations through the process outlined in Sec. 2.3.1. For a given parameter set, we may solve for the S-matrix at each on-shell energy E to obtain an S-wave $\pi N \to \pi N$ phase shift, and an inelasticity, which are given by

$$\delta_{\pi N}(E) = \frac{1}{2}\,\mathrm{atan}\left(\frac{\mathrm{Im}\,S_{\pi N\pi N}(E)}{\mathrm{Re}\,S_{\pi N\pi N}(E)}\right) , \tag{5.5}$$

$$\eta(E) = |S_{\pi N\pi N}(E)| \,. \tag{5.6}$$

These may then be compared to the WI08 scattering data [54, 55], and using Powell's derivative-free optimisation procedure [73] to minimise the χ^2, we are able to constrain the free parameters in the Hamiltonian. As the $N^*(1535)$ lies approximately 100 MeV below the $K\Lambda$ threshold, the coupling $g^{N_1}_{K\Lambda}$ was held fixed at zero. With the remaining coupling strengths, bare state masses, and regulator parameters, there are a total of 21 free parameters present in this system. The resultant parameter set is presented in Table 5.1.

The resultant S_{11} phase shift and inelasticity are illustrated in Fig. 5.1, along with the corresponding T-matrix components. Using this parameter set, we are able to characterise the S_{11} phase shifts in the energy range considered. This fit results in a χ^2 of 604, and with $78 - 21 = 57$ degrees-of-freedom (d.o.f.s), a $\chi^2/\text{d.o.f.}$ of 10.6. While this $\chi^2/\text{d.o.f.}$ is large, it can be attributed to missing three-particle $\pi\pi N$ threshold effects, as can be seen in the tension in the inelasticity predictions near 1.4 GeV. Difficulties describing the inelasticities above the $N^*(1650)$ region may also be attributed to a sizeable contribution from $\pi\pi N$ states, or additional hyperon channels such as $K\Sigma$. Interestingly, the tension in

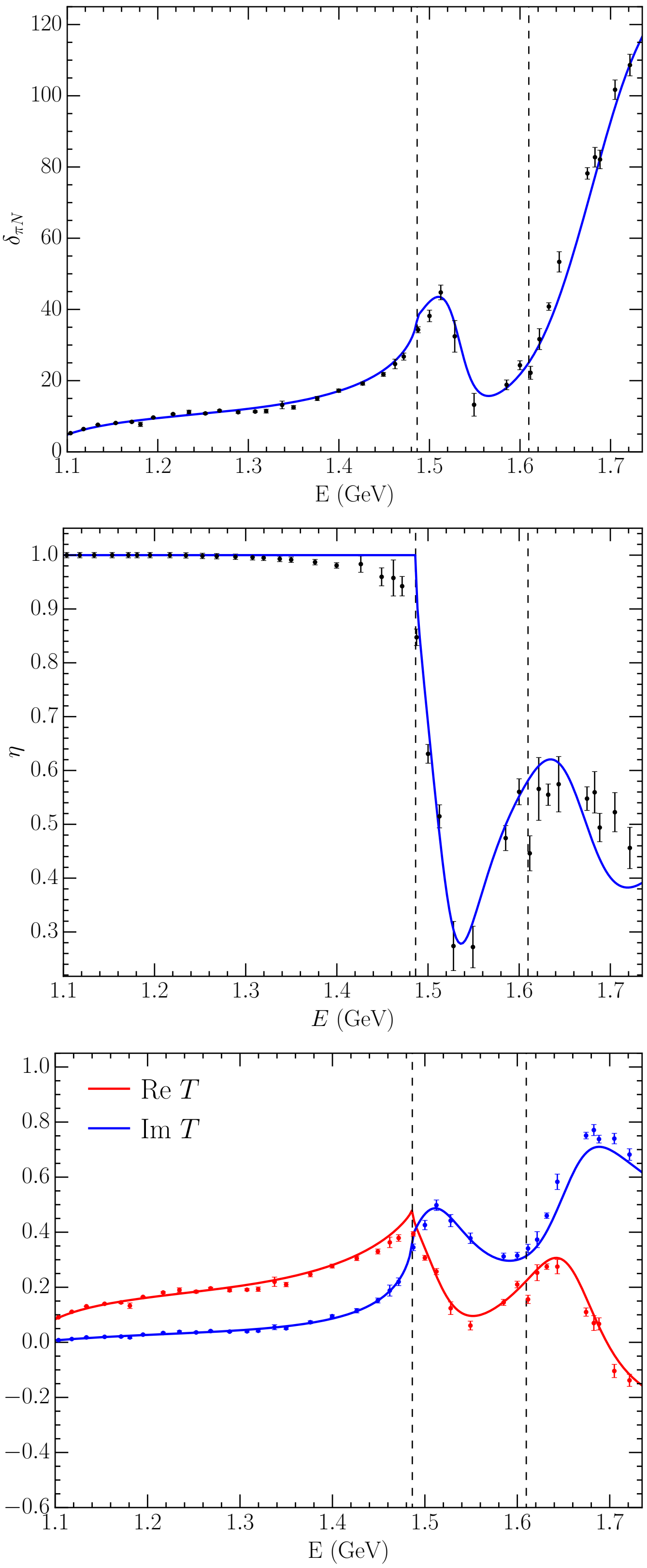

Figure 5.1: Phase shift and inelasticity for the parameters in Table 5.1 are illustrated in the two upper plots. The solid (blue) lines are the theoretical calculations from HEFT, while the data points are the SAID WI08 solution [54, 55]. The lower plot compares the real and imaginary T-matrix components from HEFT to the SAID data. The dashed vertical lines denote the ηN and $K\Lambda$ thresholds.

the inelasticity calculation appears to manifest primarily in the imaginary component of the T-matrix. While this $\chi^2/\text{d.o.f.}$ is not directly comparable with similar studies of S_{11} scattering [70] due to the use of the WI08 solution versus single-energy values, visually the fit of Ref. [70] and that presented here produce a similar quality of fit. Alternatively, quantities such as the positions of poles corresponding with the two odd-parity resonances may prove to be a better source of comparison.

As described in Sec. 2.3.2 and Sec. 4.2, for a system with two bare basis states we represent the propagator by a matrix of dressed states. For the Hamiltonian as described in this chapter, this matrix has the form

$$A(E)^{-1} = \begin{pmatrix} E - m_{N_1} - \bar{\Sigma}_{N_1 N_1}(E) & -\bar{\Sigma}_{N_2 N_1}(E) \\ -\bar{\Sigma}_{N_1 N_2}(E) & E - m_{N_2} - \bar{\Sigma}_{N_2 N_2}(E) \end{pmatrix} . \tag{5.7}$$

By solving for complex energies E_i such that $\det\{A(E_i)^{-1}\} = 0$, we are able to solve for the positions of any poles in the T-matrix. In the Particle Data Group (PDG) tables [3], the poles for the two low-lying odd-parity nucleon resonances are reported as

$$\begin{aligned} E_{N^*(1535)} &= 1510 \pm 10 - (65 \pm 10)i \text{ MeV} , \\ E_{N^*(1650)} &= 1655 \pm 15 - (67 \pm 18)i \text{ MeV} . \end{aligned} \tag{5.8}$$

With the set of parameters in Table 5.1, and searching in the second Riemann sheet, using HEFT two poles are found at energies

$$\begin{aligned} E_1 &= 1500 - 50i \text{ MeV} , \\ E_2 &= 1658 - 56i \text{ MeV} , \end{aligned} \tag{5.9}$$

in excellent agreement with the PDG pole positions.

By comparing phase shifts and inelasticities calculated in HEFT with those from resources such as SAID, and T-matrix poles with PDG values, it is clear that an interpretation of the low-lying odd-parity nucleon resonances as quark-model like states is consistent with experiment. By moving to a finite-volume and comparing with results from lattice QCD however, we are able to gain a larger degree of understanding, and further test this interpretation.

5.2 Finite-Volume HEFT at 3 fm

5.2.1 Pion Mass Dependence

By varying the pion mass m_π, and the lattice extent L, one can solve for the eigenvalues and eigenvectors of the Hamiltonian to obtain the finite-volume energy spectrum, the results of which can be compared with lattice QCD. As the pion mass is increased, the masses of the other hadrons are also increased proportionally, as to match the hadron masses calculated by PACS-CS [47]. As the pion-mass extrapolations for the bare states are unknown, we give them a simple expansion of the form

$$m_{N_i}(m_\pi^2) = m_{N_i}|_{\text{phys}} + \alpha_{N_i}\left(m_\pi^2 - m_\pi^2|_{\text{phys}}\right) , \tag{5.10}$$

where the mass-slopes α_{N_i} are varied to fit 10 lattice QCD data points at $L \sim 3$ fm, and a pion mass varying from 169 to 623 MeV in the Sommer scheme [47]. Additionally, $m_{N_i}|_{\text{phys}}$ is mass of each bare basis state at the physical point. It was found that as the bare mass slope only has an impact at significantly larger than physical pion masses, fitting to the lattice QCD energies at the lightest pion mass had little effect on the mass slope. As such, the fitting procedure focused on minimising the distance between the lattice QCD data at the three heaviest pion masses, and HEFT energy eigenvalues. While there is also precise data available at $L \sim 2$ fm which could also be used for the fitting procedure, it is desirable to confront the spectrum at 2 fm as a prediction from the 3 fm analysis. As the parameters of the Hamiltonian are constrained by experiment, the key input from the 3 fm analysis is the quark-mass slope of the bare masses, α_{N_1} and α_{N_2}.

The 3 fm fitting procedure gives mass slopes

$$\begin{aligned} \alpha_{N_1} &= 0.944\,\text{GeV}^{-1} , \\ \alpha_{N_2} &= 0.611\,\text{GeV}^{-1} . \end{aligned} \tag{5.11}$$

The differences in the slope parameters are in accord with quark model expectations. The lower state is dominated by hyperfine attraction in spin-1/2 components of the wave function. The strength of the hyperfine attraction is inversely proportional to the product of the constituent quark masses. Thus, as the constituent quark mass increases, the hyperfine attraction is lost and the baryon mass increases rapidly. On the other hand, the second state is dominated by spin-3/2 components contributing to hyperfine repulsion. For the second state, repulsion is lost as the constituent quark masses increase and thus the baryon mass rises more slowly.

5.2.2 Finite-Volume Energy Spectrum

We are now able to calculate the full finite-volume energy spectrum for this system. In the Sommer scheme, the physical volume varies with the quark mass. At the physical point, the lattice extent is 2.99 fm, corresponding with the lattice size at the lightest lattice QCD point. As the pion mass is increased, the lattice size is linearly interpolated between each lattice QCD point, giving a final lattice size of 3.27 fm. The results of this can be seen in Fig. 5.2, where the non-interacting basis states have been displayed as dashed lines, and the interacting energies displayed as solid lines. Here we observe a significant shift from the non-interacting states, as well as the presence of many avoided level crossings in the excited states of the spectrum, demonstrating the complexity of the system. The HEFT spectrum is compared to available lattice QCD results at approximately 3 fm.

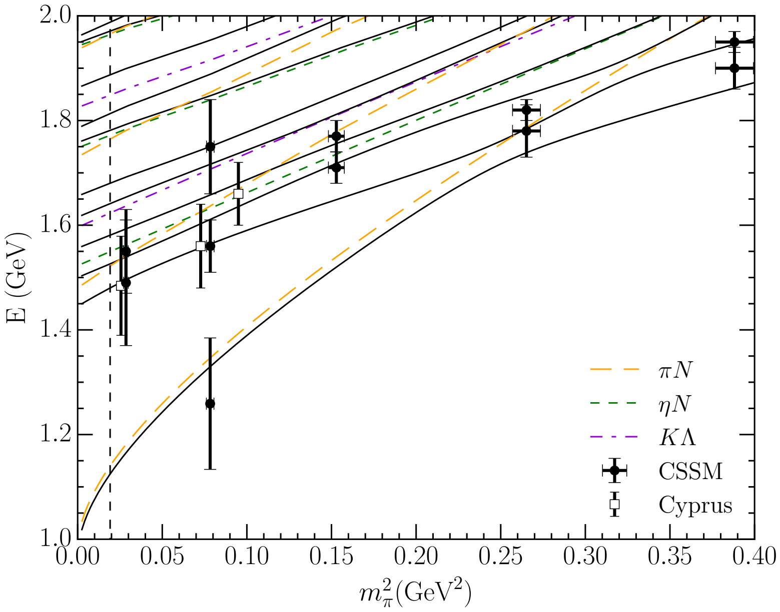

Figure 5.2: Finite-volume energy spectrum for $L \sim 3$ fm. The vertical dashed line represents the physical points, while the remaining dashed lines correspond with non-interacting basis states for each channel. The solid curves are the finite-volume eigenenergies calculated in HEFT. Lattice QCD data from CSSM [68, 72, 74] and the Cyprus collaboration [75] is overlaid for comparison.

One of the biggest advantages of HEFT however, is the ability to extract the eigenvectors of the Hamiltonian. The eigenvector $|\langle B_j|E_i\rangle|^2$ denotes the contribution from the basis state $|B_j\rangle$ to the eigenstate $|E_i\rangle$, the results of which are shown in Fig. 5.3 for the first six eigenvalues at $L \sim 3$ fm. Here it can be seen that initially at the physical point, it is difficult to interpret a single state as representing one of the odd-parity resonances. The contributions from the two bare states, denoted by red and blue lines respectively, are instead distributed over the second through to the sixth eigenstates. However the contributions from the bare states do seem to be concentrated around the masses of the bare states. At this point, it is only the lowest-lying state which can be definitively interpreted as a πN state.

As one moves away from the physical pion mass, contributions from the two bare states seem to become increasingly concentrated in the lower-lying eigenstates, and both the lowest-lying state and next state seem to each contain approximately equal amounts of each bare state. In other words, the bare states mix to form the energy eigenstates. The situation is similar to the mixing of the two spin-1/2 negative parity interpolators which mix to form the lattice eigenstates.

In order to better view how the contributions from the bare states are distributed, we overlay coloured lines on the energy spectrum in Fig. 5.2. Here, we display the state with the largest and second largest contributions from the first bare basis state as solid and dashed red lines respectively. The contributions from the second bare basis state are illustrated in the same manner but in blue. The results of this are illustrated in Fig. 5.4.

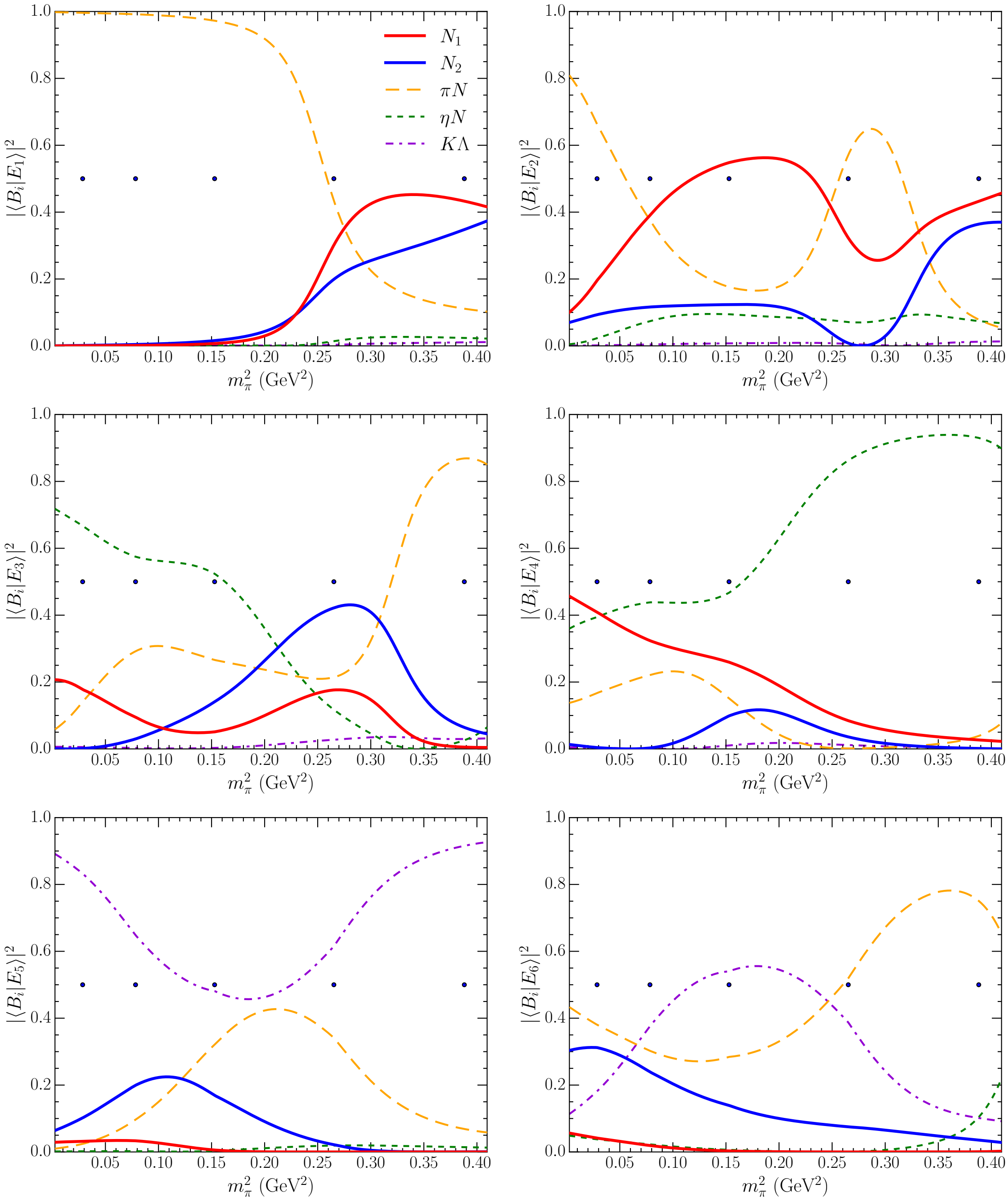

Figure 5.3: Pion mass dependence of the basis-state contributions for the six lowest eigenstates from the 3 fm spectrum shown in Fig. 5.2. Markers on each plot correspond with the five PACS-CS masses [47]. Contributions for the sum of all momentum states in the πN, ηN, and $K\Lambda$ channels are illustrated.

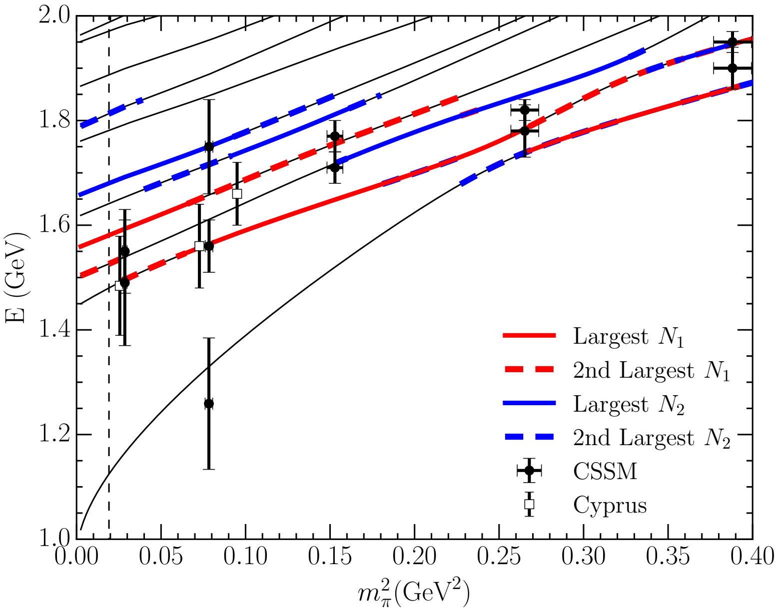

Figure 5.4: As in Fig. 5.2, with contributions from bare basis states $|N_1\rangle$ and $|N_2\rangle$. The solid and dashed red lines represent the states with the largest and second largest contributions from the lower bare basis state. Similarly the solid and dashed blue lines represent the contributions from the second bare basis state. Lattice QCD data from CSSM [68, 72, 74] and the Cyprus collaboration [75] is overlaid for comparison.

Utilising this method of identifying states with a large bare-basis state component, it becomes easier to understand which states are likely to be observed in the CSSM and Cyprus lattice QCD calculations. Because they used three-quark operators to form the basis of their correlation matrix, it follows that the states excited in their analysis will contain a large bare basis state component. Thus we expect each of their lattice QCD results to be associated with a coloured energy eigenstate from HEFT. The exception to this is the lowest lying CSSM state at $m_\pi^2 \sim 0.08$ GeV^2, which was obtained from a five-quark operator [68].

Of particular note, as we move to larger quark masses, the contributions from each bare state become primarily concentrated in only two eigenstates, which strongly correspond with the states from lattice QCD. This is in agreement with the results from Ref. [72], where the magnetic moments of the two resonances become more quark-model like as the pion mass increases. In addition, the three results from the Cyprus Collaboration [75] which were constructed using only three-quark operators, correspond with eigenstates dominated by contributions from the lower lying bare state.

One concludes that while the low lying states are quark-model like at heavy quark masses, one cannot make the same conclusion at light quark masses as the three-quark component of HEFT eigenstates corresponding to lattice QCD eigenstates is of the order 20% – 30%. As a result, one must regard these resonances as a mixture of three-quark, and rescattering contributions.

Of particular contemporary interest is the role of strange quarks in these low lying resonances. Here we can examine the contributions from the $K\Lambda$ channel at each HEFT eigenstate which corresponds with a lattice QCD mass. Here we see that the strange quark component of these states is at most 10% in the case of the lightest mass for the state corresponding with the first excited lattice QCD state, but is typically of order 1% and therefore a relatively small component.

5.3 Finite-Volume HEFT at 2 fm

Lattice QCD results are available for lattice sizes of approximately 2 fm from Lang & Verduci [76], as well as the Hadron Spectrum Collaboration (HSC) [77, 78]. As Lang & Verduci's correlation matrix analysis was not large enough to remove excited-state contaminations from their second and third states, we focus on their lowest-lying state obtained from a non-local momentum-projected pion-nucleon interpolating field. While in principle we could use this data for fitting the bare mass slopes, in Chapter 3 it was found that by calculating the bare mass slopes at only one lattice size, the lattice QCD data for other sizes was able to be described. As such, we continue to use the bare mass slopes from Eq. (5.11) for this $L \sim 2$ fm calculation, and thus make predictions for the finite-volume energy eigenvalues at various quark masses.

The HSC collaboration sets their lattice spacing in a scheme where the physical Ω^- baryon mass is taken to be independent of the sea-quark mass. As a result, the lattice spacing varies with quark mass. Here, an identical approach is taken to the 3 fm calculation in regards to the lattice size. At the physical point, the lattice extent is 1.95 fm, corresponding with the lattice size at the Lang & Verduci lattice QCD mass. As the pion mass is increased, the lattice size is linearly interpolated between each lattice QCD point, giving a final lattice size of 2.12 fm. The hadron masses are also varied as described in Eq. (5.10). The result for this process is illustrated in Fig. 5.5, where similarly to the $L \sim 3$ fm case, significant shifts in the energy eigenvalues from the non-interacting energies are observed. Comparing to the lattice QCD data from HSC and Lang & Verduci, we observe that all data points correspond with an energy eigenvalue, with the exception of a single point from HSC, which sits between the two lowest-lying states we predict. By investigating the eigenvector composition of these states, we are able to better analyse the consistency of this data with the two bare state analysis.

Due to the lower density of states, we only consider the eigenvector composition of the four lowest-lying states in Fig. 5.6, as opposed to the six eigenstates in Sec. 5.2. For the 2 fm spectrum, we observe a similar behaviour in the eigenvectors as in the 3 fm spectrum. Initially, the lowest-lying state consists almost purely of the πN basis state, while the two bare basis states are concentrated in the higher excited states. As the pion mass increases however, a significantly larger portion of the bare state eigenvector components become more concentrated in the lowest-lying state. As such, at larger pion masses we expect to see lattice QCD states constructed from three-quark operators to correspond with the lower-lying states in the spectrum.

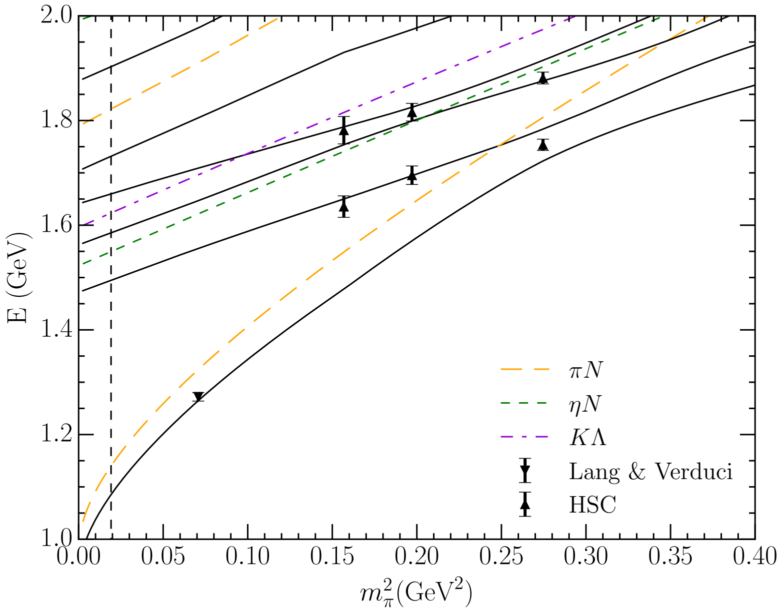

Figure 5.5: Finite-volume energy spectrum for $L \sim 2$ fm. The vertical dashed line represents the physical point, while the remaining dashed lines correspond with non-interacting basis states for each channel. Overlaid is lattice QCD results from Lang & Verduci [76] using momentum-projected meson-baryon operators, and the Hadron Spectrum Collaboration (HSC) [77, 78] using three-quark operators.

Returning to Fig. 5.5, it is immediately clear that the lowest lying high-precision point from Lang & Verduci is very well described by HEFT. Because this is a low-lying state in the spectrum, it is protected by the Lüscher relation embedded within the HEFT formalism. Moreover, because the point is calculated at a relatively small value of the pion mass, it is relatively insensitive to the quark mass interpolation. In short, this confrontation between lattice QCD and HEFT is also predominantly a confrontation between lattice QCD and experiment. While this state is composed primarily of the zero momentum πN basis state, the other basis state contributions are vital to generating the significant shift in the eigenstate energy down from the non interacting basis-state energy.

To better compare with lattice QCD, we overlay the contributions from these bare states onto the energy spectrum, which can be seen in Fig. 5.7. Considering the data from HSC, we observe their six points correspond with states consisting primarily of bare basis states. The lowest-lying points correspond with the lighter bare state, while their excited states correspond with the eigenstate dominated by the second bare basis state. This further supports the interpretation of the two odd-parity nucleon resonances as being quark-model like.

It is impressive that five of the six HSC results sit precisely on the HEFT states dominated by bare basis-state components. It is a testament to the precision of their lattice QCD analysis and the rigour with which HEFT can link different volumes and quark masses within a single formalism. The notable exception is the lowest-lying state at the largest quark mass where a nearby scattering-state provides a scattering-state contamina-

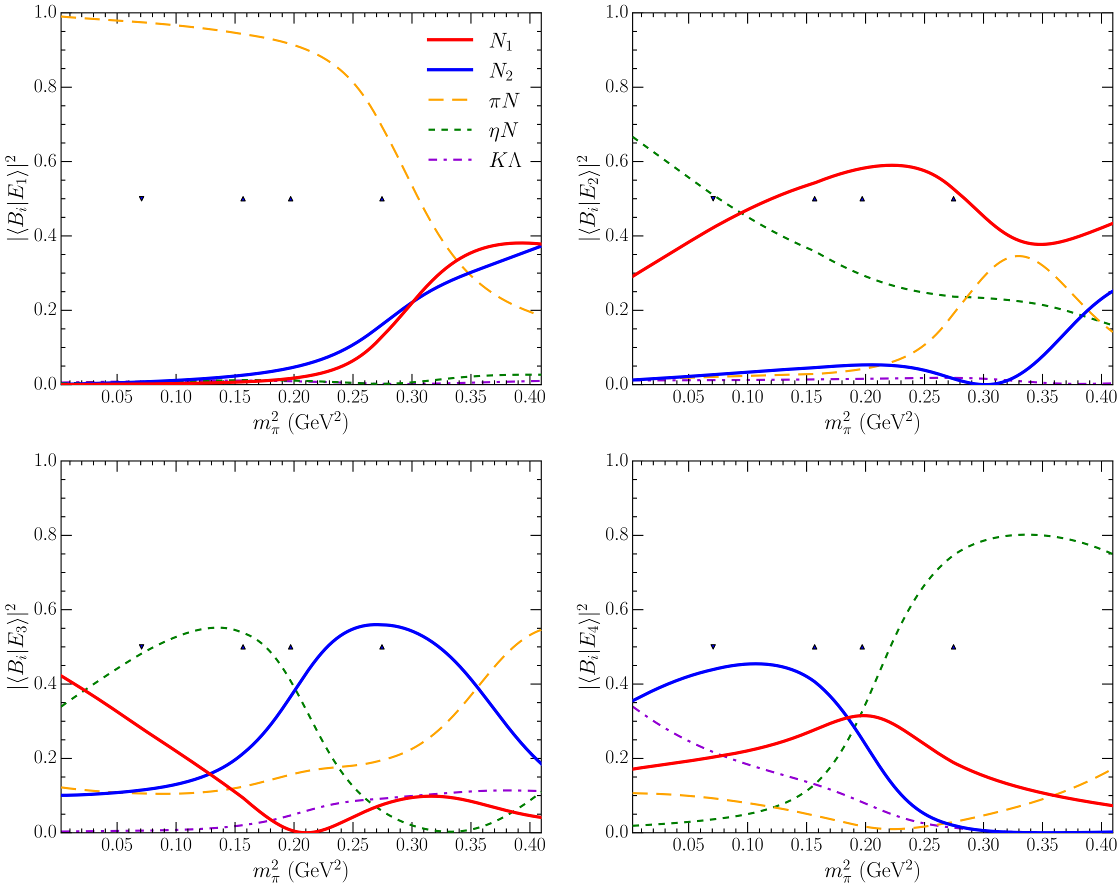

Figure 5.6: Pion mass dependence of the basis-state contributions for the four lowest eigenstates from the 2 fm spectrum shown in Fig. 5.5. Markers on each plot correspond with the single Lang & Verduci mass [76] and three HSC masses [77, 78]. Contributions for the sum of all momentum states in the πN, ηN, and $K\Lambda$ channels are illustrated.

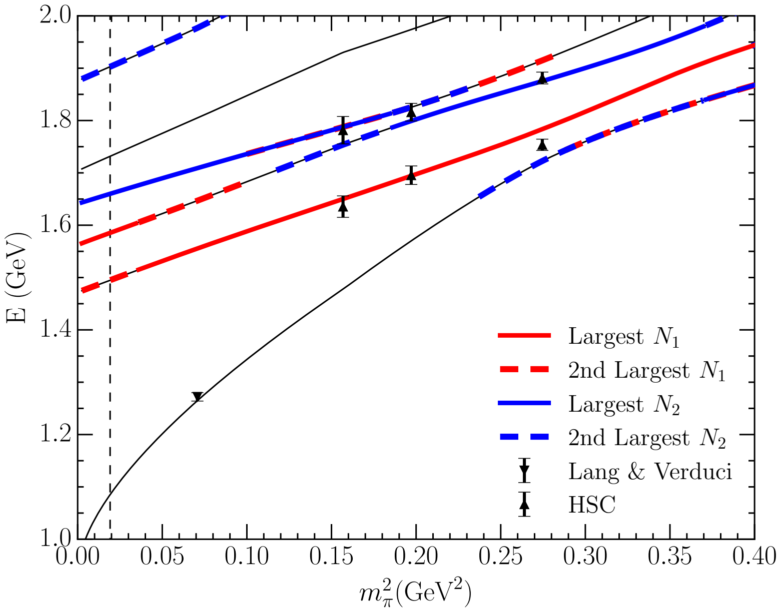

Figure 5.7: Finite-volume energy spectrum for $L \sim 2$ fm. The solid and dashed red lines represent the states with the largest and second largest contributions from the lower bare basis state. Similarly the solid and dashed blue lines represent the contributions from the second bare basis state. Lattice QCD results from Lang & Verduci [76] and the Hadron Spectrum Collaboration (HSC) [77, 78]. are overlaid for comparison.

tion in their correlation-matrix analysis. Of course the authors were completely aware of this possibility and discussed the importance of future calculations including both three-quark interpolators and a complete set of non-local momentum-projected multi-hadron operators. In Sec. 5.5, a novel HEFT formalism is introduced to quantify the extent of this scattering state contribution.

5.4 Finite-Volume HEFT at 4 fm

Recent lattice QCD calculations of πN scattering process were performed by the CLS consortium [64], and included momentum-projected two-particle interpolating fields. In particular, we are interested in the zero-momentum $I = 1/2$, $G_{1u}(0)$ results from Fig. 4a of Ref. [64]. These calculations were done for a pion mass of 200 MeV, with a spatial lattice extent of $L = 4.05$ fm. By altering the nucleon mass at $m_\pi = 200$ MeV in the HEFT formalism to $m_N = 0.959$ GeV, to match the non-interacting $\pi N(k = 0)$ state in Fig. 4a of Ref. [64], we are able to compare the eigenenergies from HEFT with the lattice QCD calculations from the CLS consortium.

Using the fit parameters from Table 5.1, and the bare basis state slopes from Sec. 5.2, this comparison is illustrated in Fig. 5.8. HEFT predicts a small amount of attraction in the scattering state energies relative to the non-interacting two-particle πN basis state

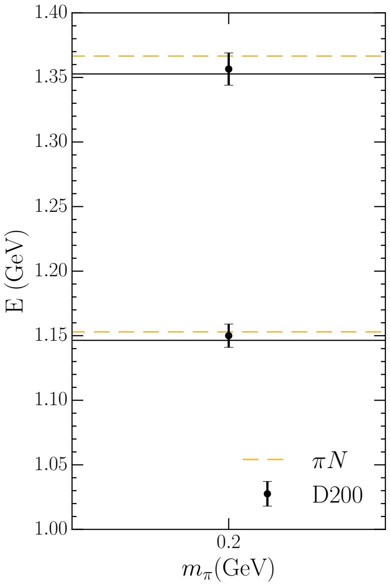

Figure 5.8: Comparison between the energy eigenvalues calculated in HEFT at a lattice size of $L = 4.05$ fm (solid black lines), and the lattice QCD calculations from the CLS consortium (data points) using the D200 ensemble [64]. Dashed lines indicate the non-interacting two-particle πN energies for $k = 0$ and $k = 1$.

energies for $k = 0$ and $k = 1$. The CLS results are in excellent agreement with these HEFT predictions, showing effects of a similar magnitude and direction. Considering the eigenvectors of these two eigenstates from HEFT, the ground state consists of 99.6% $\pi N(k = 0)$, resulting in the minimal shift away from the non-interacting state. Similarly, 96% of the first excited state is composed of the $\pi N(k = 1)$ state, with a majority of the remaining contributions coming from the two bare states. As the majority of the lower mass bare state is concentrated in the fourth excited state, the bare basis states have a limited impact on the eigenstates considered in this energy range. Nonetheless, it is useful to see that the HEFT formalism correctly extends to the $L = 4.05$ fm results from the CLS consortium, as in the $L \sim 2$ fm case in Sec. 5.3.

5.5 Scattering-State Contaminations

In Sec. 2.4.6, we introduced a novel HEFT formalism for estimating scattering-state contaminations in lattice QCD correlation functions constructed with standard three-quark operators, in a system with a single bare basis state. Recalling from Eq. (2.93), we construct a simulation of the lattice QCD correlation function from HEFT eigenvectors, with the form

$$G_{B_0}(t) = \sum_i |\langle B_0|E_i\rangle|^2 \, e^{-E_i t} \, . \tag{5.12}$$

By removing the contributions from the eigenstate with largest bare basis state eigenvector component, as in Eq. (2.94) we also define the two-particle scattering-state contamination function,

$$C_{B_0}(t) = \frac{1}{G_{B_0}(t)} \sum_{i \neq B_0} |\langle B_0 | E_i \rangle|^2 \, e^{-E_i t} \, . \tag{5.13}$$

We may extend these definitions to a system with two bare basis states. This time, states are excited from the vacuum with three-quark operators χ_1 and χ_2. For example, the odd-parity proton interpolators $\chi_1 = \varepsilon^{abc} \left(u^{Ta} \, C\gamma_5 \, d^b \right) \gamma_5 \, u^c$ and $\chi_2 = \varepsilon^{abc} \left(u^{Ta} \, C \, d^b \right) u^c$ are both $\mathcal{O}(p/E)$ in a nonrelativistic reduction and mix strongly in a correlation matrix analysis to isolate the eigenstates. Each of these interpolating fields acting on the QCD vacuum will create a bare basis state $|N_1\rangle$ and $|N_2\rangle$,

$$(\alpha^* \, \overline{\chi_1} + \beta^* \, \overline{\chi_2}) \, |\Omega\rangle = \alpha^* \, |N_1\rangle + \beta^* \, |N_2\rangle \ , \tag{5.14}$$

which are mixed in forming the energy eigenstates, $|E_i\rangle$. Where previously we had a single eigenstate with largest bare state contribution, labelled $|E_{B_0}\rangle$, in the two bare state system there will be a corresponding Hamiltonian eigenstate for each bare state. We label these states $|E_{N_1}\rangle$ and $|E_{N_2}\rangle$, representing the eigenstates with largest contributions from the bare basis states $|N_1\rangle$ and $|N_2\rangle$ respectively. As these eigenstates are a mixture of each bare state, they will be constructed for different combinations of α and β, given by α_j and β_j, where $j = 1, 2$ corresponds with N_1 and N_2 respectively. With this in mind, correlation functions optimised for these two eigenstates are constructed as

$$\begin{aligned} G_j(\boldsymbol{p}, t) = \sum_{\boldsymbol{x}} e^{-i\boldsymbol{p}\cdot\boldsymbol{x}} \, \langle \Omega | \, (\alpha_j \, \chi_1(\boldsymbol{x}, t) + \beta_j \, \chi_2(\boldsymbol{x}, t)) \\ \times \left(\alpha_j^* \, \bar{\chi}_1(0) + \beta_j^* \, \bar{\chi}_2(0) \right) |\Omega\rangle \ . \end{aligned} \tag{5.15}$$

Inserting a complete set of states, setting $\boldsymbol{p} = 0$, and applying Eq. (5.14),

$$\begin{aligned} G_j(t) &= \sum_i (\alpha_j \, \langle N_1 | + \beta_j \, \langle N_2 |) \, |E_i\rangle \, \langle E_i | \\ &\qquad \times \left(\alpha_j^* \, |N_1\rangle + \beta_j^* \, |N_2\rangle \right) \, e^{-E_i t} \, , \\ &= \sum_i |\alpha_j \, \langle N_1 | E_i \rangle + \beta_j \, \langle N_2 | E_i \rangle|^2 \, e^{-E_i t} \, . \end{aligned} \tag{5.16}$$

We note that α_j and β_j can be made real [79], and the eigenvector components $\langle N_j | E_i \rangle$ are real.

The mixing parameters for each of the two eigenstates, labelled α_j and β_j, may be obtained either through the eigenvectors of correlation matrices from lattice QCD, or through the Hamiltonian eigenvectors from HEFT. Importantly however, the lattice QCD correlation matrix eigenvectors must be normalised to $\mathcal{O}(1)$, as described in Ref. [74]. In the case of HEFT, the eigenvector components are $\mathcal{O}(1)$ via the standard normalisation with the sum of the squares of the components equal to one. Given that strength is localised within the spectrum, the values are insensitive to the size of the Hamiltonian matrix.

The scattering-state contamination to each of the eigenstate-optimised correlation functions of Eqs. (5.15) and (5.16) is obtained by removing the two energy eigenstates whose composition is dominated by the bare basis states (which recall are labelled $|E_{N_1}\rangle$ and $|E_{N_2}\rangle$). The idea is that the lattice correlation matrix will be effective in isolating two states which couple strongly to the three-quark operators, but lacks the additional information to isolate the scattering states. While the lattice QCD calculations of Ref. [74] isolate states in an 8×8 correlation matrix, appropriate orthogonality is evident in the optimised correlation function for each state, $G_i(t)$. For example, the contribution of $|E_{N_2}\rangle$ to the optimised correlator $G_1(t)$, governed by $\alpha_1 \langle N_1|E_{N_2}\rangle + \beta_1 \langle N_2|E_{N_2}\rangle$, is small. Similarly the contribution of E_{N_1} to the optimised correlator $G_2(t)$, governed by $\alpha_2 \langle N_1|E_{N_1}\rangle + \beta_2 \langle N_2|E_{N_1}\rangle$, is also small. At most, contributions from $|E_{N_1}\rangle$ and $|E_{N_2}\rangle$ to $G_1(t)$ and $G_2(t)$ respectively are of order 5%, though typically take values closer to 1%.

The optimised contamination functions for these two bare-dominated states are therefore written as

$$C_j(t) = \frac{1}{G_j(t)} \sum_{i \neq N_1, N_2} \left(\alpha_j \langle N_1|E_i\rangle + \beta_j \langle N_2|E_i\rangle\right)^2 e^{-E_i t} \,. \tag{5.17}$$

Here, the notation of $i \neq N_1, N_2$ denotes that we avoid summing over the energy eigenstates labelled $|E_{N_1}\rangle$ and $|E_{N_2}\rangle$.

5.5.1 Contamination Function at 3 fm

5.5.1.1 Two Particle Scattering-State Contamination

To determine the degree of scattering-state contamination in the lattice QCD correlation functions of Eq. (5.16), which have been optimised for the states $|E_{N_1}\rangle$ and $|E_{N_2}\rangle$, we consider the contamination functions as defined in Eq. (5.17), eliminating the contribution from the states which are identified as corresponding to the lattice QCD results.

As can be seen in Fig. 5.4, at each lattice QCD mass there is not necessarily only a single corresponding HEFT eigenstate. Taking the second heaviest mass from Fig. 5.4 as an example, we see that both the first and second states have approximately equal contributions from m_{N_1}. Indeed, there is no single eigenstate corresponding with the single-particle, three-quark core, but rather both eigenstates may be described as quark-model like, and corresponding with the lattice QCD state associated with the $N^*(1535)$. For the $L \sim 3$ fm analysis, this effect can be seen at all but the heaviest lattice QCD masses. As a result, to remove the bare basis state contributions from the correlation functions as described in the previous section, we must remove not only the contribution from the two eigenstates with largest bare basis state eigenvector components, but also the contribution from the two eigenstates with second largest bare basis state components. In the context of Fig. 5.4, we remove the contributions from all highlighted eigenstates from the correlation functions. This method will allow a proper determination of the level of two-particle dominated scattering-state contributions, having removed all significant sources of single-particle contributions.

In calculating these contamination functions, we compare two sources of values for α_j and β_j. From Ref. [74], the eigenvectors of the correlation matrix were calculated in lattice QCD for an 8×8 correlation matrix, with four sets of smearings at both the source and sink. Here, we consider the 100 sweep smearings from Fig. 11a of Ref. [74], which dominate the eigenvalue components. Coefficients for α_1 and α_2 are taken from the 100-sweep χ_1 (u_5) component of the eigenvectors for states 1 and 2 respectively. Similarly, β_1 and β_2 are taken from the 100-sweep χ_2 (u_6) component of the eigenvectors for states 1 and 2. We note the important sign change in β_i as one moves from state 1 to 2.

We compare these lattice QCD results for α_j and β_j with the corresponding quantities calculated from the eigenvectors of the Hamiltonian in HEFT. In this case, these mixing factors are given by

$$\begin{aligned} \alpha_1 &= \langle N_1 | E_{N_1} \rangle \,, \quad \beta_1 = \langle N_2 | E_{N_1} \rangle \,, \\ \alpha_2 &= \langle N_1 | E_{N_2} \rangle \,, \quad \beta_2 = \langle N_2 | E_{N_2} \rangle \,. \end{aligned} \tag{5.18}$$

The eigenstates $|E_{N_1}\rangle$ and $|E_{N_2}\rangle$ correspond with the states illustrated in Fig. 5.4 with solid red and solid blue lines respectively.

In Fig. 5.9, these two schemes for determining α_j and β_j are compared by calculating contamination functions as defined in Eq. (5.17) at each PACS-CS pion mass. As described above, we remove not only the contribution from the two eigenstates with largest bare basis state eigenvector component, but also the contribution from the eigenstates with second largest bare basis state component.

Broadly considering these two-particle contamination functions, we observe two situations. At lighter pion masses, where the bare-dominated states $|E_{N_1}\rangle$ and $|E_{N_2}\rangle$ sit above the lower-lying eigenstates, we observe a scattering-state contamination which has a minimum in the vicinity of $1-2$ fm. At the heavier pion masses, where these bare-dominated states are found in the lower-lying eigenstates, the contamination tends to zero as time increases, as all excited states become exponentially suppressed. There is a remarkable similarity between the contamination functions constructed from the correlation matrix eigenvectors from lattice QCD, and the Hamiltonian eigenvectors from HEFT.

Considering specific pion masses, at the two largest masses we observe a strong decay in the contamination, where all scattering state contaminations are at the 5-10% range at Euclidean times where you'd expect to observe an effective-mass plateau. At the third heaviest mass, we observe a minimum contamination in the plateau region of 6% for N_1, which is in line with the prediction from Ref. [72] of approximately 5%. As described in Ref. [72], we observe a larger degree of scattering-state contamination in the correlation function corresponding with N_2 for the second lightest mass. For the two lightest masses, some degree of scattering-state contamination is to be expected, as they fall near the ηN and $K\Lambda$ thresholds.

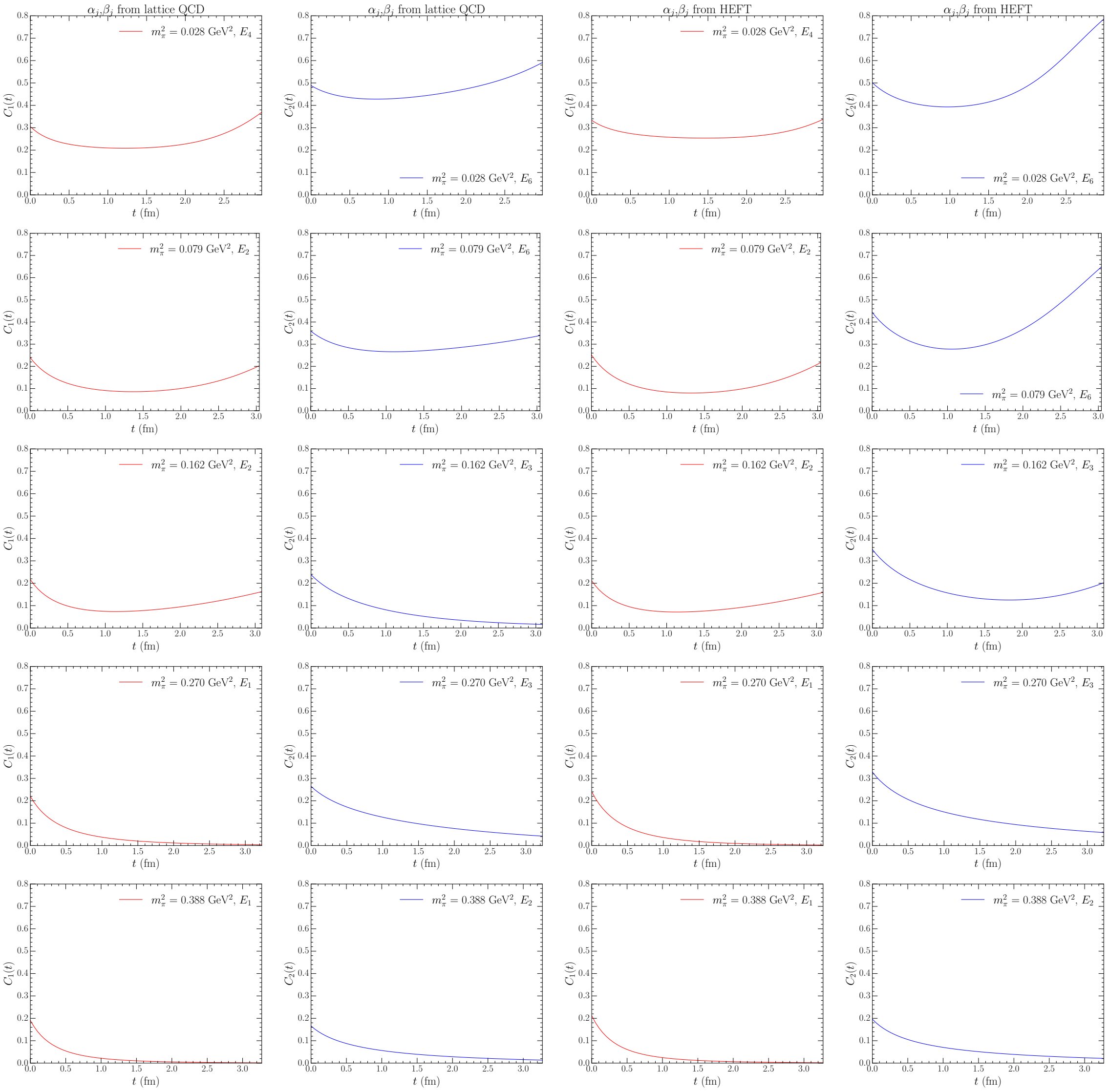

Figure 5.9: Contamination functions from Eq. (5.17) at the five pion masses considered by the PACS-CS collaboration [47], with a lattice size $L \sim 3$ fm, where the pion mass increases as one moves down the columns. Contributions from the two eigenstates with largest and second-largest single-particle component have been removed from the correlation functions (all highlighted eigenstates in Fig. 5.4). Values for α_j and β_j are taken from lattice QCD correlation matrix eigenvectors for the two left-most columns, and taken from HEFT eigenvectors as defined in Eq. (5.18) for the two right-most columns. The first and third columns (red lines) correspond with the eigenstates dominated by contributions from $|N_1\rangle$, while the second and fourth columns (blue lines) correspond with the eigenstates dominated by contributions from $|N_2\rangle$. The relevant eigenstate for each lattice QCD energy level is labelled by E_i.

5.5.1.2 Single-Particle and Two-Particle Contamination

In the previous section, we analysed the two-particle scattering-state contamination by removing contributions to the correlation functions from all eigenstates with a significant single-particle bare basis state eigenvector component. There the two-particle scattering state contaminations for the three heaviest quark masses considered were found to be typically small, the order of 10% in the Euclidean time range where masses and form factors are extracted.

Here we explore a different problem where the bare basis state becomes significantly associated with more than one energy eigenstate. The extent of this distribution over eigenstates is directly related to the volume of the lattice which governs the number of eigenstates within a given energy range, *i.e.* the density of energy eigenstates. As the volume increases, the density of eigenstates increases and the bare basis state becomes spread over several states.

However, lattice QCD aims to isolate a single energy eigenstate. In the absence of two-particle interpolating fields, this is done via Euclidean time evolution to allow the higher state to become become exponentially suppressed. At the same time, the uncertainties in the correlation function grow to the point that the behaviour of the correlator is consistent with a single propagating state. It is this mass that is reported, but one should remain concerned that there may be more than one state propagating in the correlator.

Drawing on the information available in the HEFT eigenvectors, we are able to quantify the contamination from both the two-particle scattering states and the distribution of significant single-particle strength across multiple energy eigenstates. This time only the two energy eigenstates having the dominant bare basis state components, $|N_1\rangle$ and $|N_2\rangle$, are eliminated. In cases where the strength is almost equal, the lower lying state is considered isolated by the Euclidean time suppression and eliminated from the contamination function.

Using Eq. (5.17) the scattering-state contaminations for the three heaviest PACS-CS masses are illustrated in Fig. 5.10. Here, the label E_i on each contamination function refers to the eigenstate associated with each lattice QCD energy level. In the case where a lattice QCD mass sits on an avoided level crossing, where two different eigenstates have approximately equally large bare basis state eigenvector components, the state with lower eigenenergy is chosen. Under Euclidean time evolution, excited states in the spectrum decay more quickly, and thus it is expected that the lower eigenenergy is isolated.

Comparing the contamination functions in Fig. 5.10 with those in the previous section, we observe a significantly higher degree of contamination. For the heaviest PACS-CS mass, we still observe a decaying contamination for large Euclidean time. As a vast majority of the bare basis state eigenvector components are concentrated in the two lowest-lying finite-volume eigenstates, we do not expect any scattering-state contamination following Euclidean time evolution. At the second and third heaviest masses however, we observe a significantly larger level of contamination.

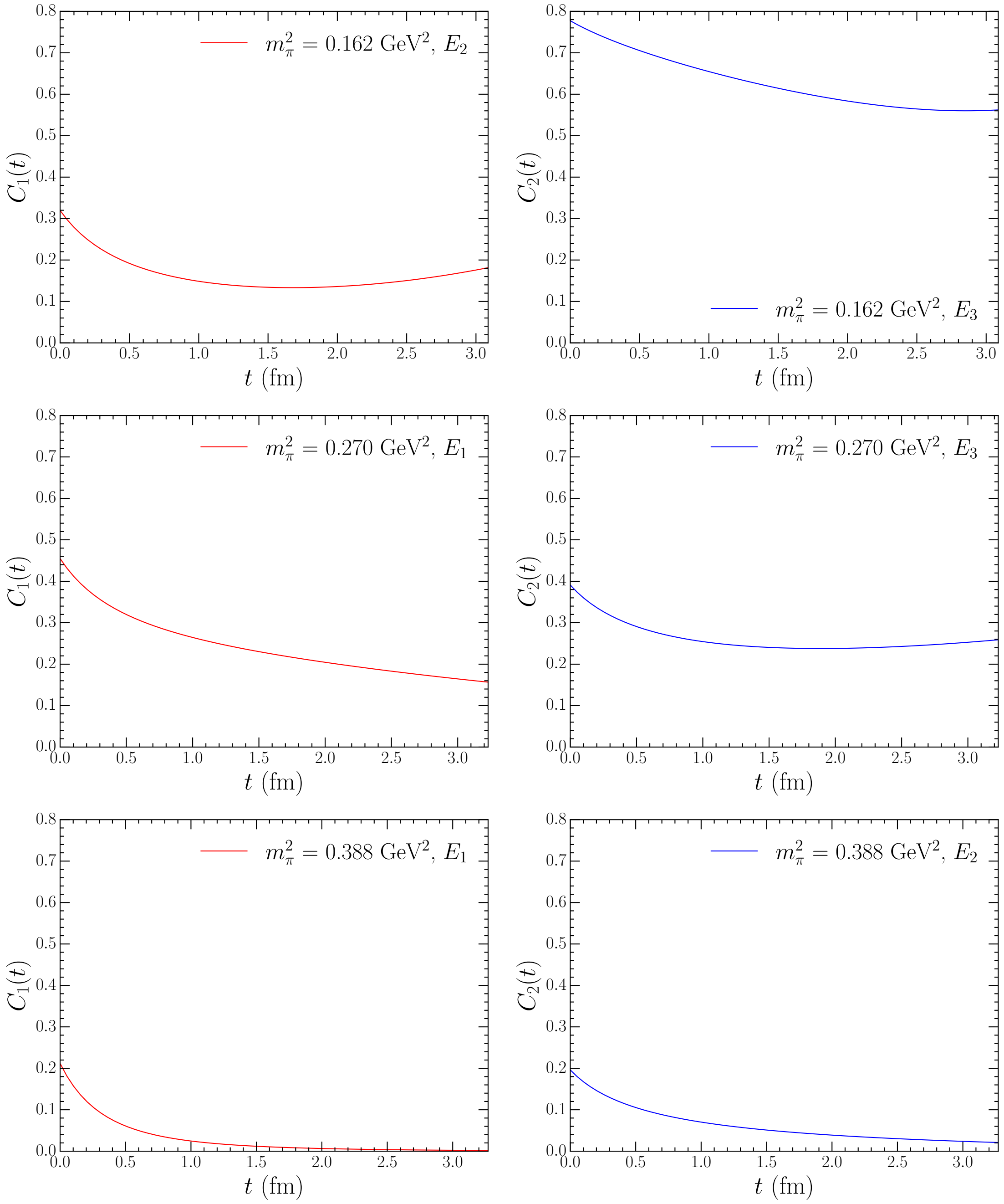

Figure 5.10: Contamination functions from Eq. (5.17) at the three heaviest pion masses considered by PACS-CS [47], with a lattice size $L \sim 3$ fm. The pion mass increases as one moves down the columns. Contributions from only the eigenstate with the largest eigenvector component for each bare basis state have been removed in calculating the contamination functions (solid highlighted state in Fig. 5.4). Values for α_i and β_i are taken from the HEFT eigenvectors as defined in Eq. (5.18). The relevant eigenstate for each lattice QCD energy state is labelled by E_i.

Consider the positions of the second and third heaviest masses on the finite-volume spectrum from Fig. 5.4. For the lower-lying lattice QCD mass at the second-heaviest pion mass, this sits directly on an avoided level crossing in the eigenvector component for N_1. As a result, whether E_1 or E_2 is chosen as the state corresponding with this lattice QCD mass, and removed from the correlation function, a significant single-particle component will remain in the correlation function. This effect is seen to a greater degree in the larger lattice QCD mass at the third heaviest pion mass. This mass sits at an avoided level crossing in $|N_2\rangle$, where the eigenvector component for $|N_2\rangle$ is significantly spread over four nearby eigenstates. In the context of Fig. 5.4, both the solid blue and dashed blue lines are moving between HEFT eigenstates at this position. At this position, the eigenstate with largest $|N_2\rangle$ component only contains approximately 15$\%$ of the contribution from $|N_2\rangle$. As such, removing only a single $|N_2\rangle$-dominated eigenstate from the correlation function will leave a significant degree of single-particle based contamination in the estimate of the scattering-state contamination. This effect is further exaggerated in the two lightest masses. Due to the high density of states at this point, the eigenvector components for the two bare basis states are further spread to nearby energy eigenstates.

In the context of exploratory lattice QCD calculations seeking to identify the nature of quark-model like states in the spectrum, the level of scattering-state contaminations illustrated in Fig. 5.10 is encouraging, in that for five of the six states considered the correlation functions are dominated by the state of interest at the level of 75$\%$ or better where the signal is extracted. Moreover, Fig. 5.9 illustrates the majority of the contamination comes from a nearby state in the spectrum having the same bare basis state.

On the other hand, it is clear that next generation lattice QCD calculations seeking quantitative comparison with experimental measurements will need to have a complete set of two-particle interpolating fields to complement the single-particle three-quark interpolating fields considered in the leading exploratory calculations. Only then can one couple to the complete set of energy eigenstates illustrated in Figs. 5.2 and 5.4 and isolate them in the solution to the generalised eigenvalue equation for the correlation matrix.

5.5.2 Contamination Functions at 2 fm

As for the 3 fm analysis, we can utilise the correlation functions as defined in Sec. 5.5 to calculate the degree of scattering-state contamination in the correlation functions corresponding with the lattice QCD results. Due to the lower density of states, we explore contamination functions calculated as defined in Eq. (5.17), where only the eigenstate with largest bare basis state eigenvector component is removed. In particular, we calculate contamination functions for the six lattice QCD results from the HSC [77, 78], as these are calculated using three-quark interpolating fields and correspond with bare-dominated states. As the eigenvectors from both the lattice QCD correlation matrix and the HEFT Hamiltonian were found to produce equivalent contamination functions in Sec. 5.5.1, we utilise the HEFT eigenvectors for this section.

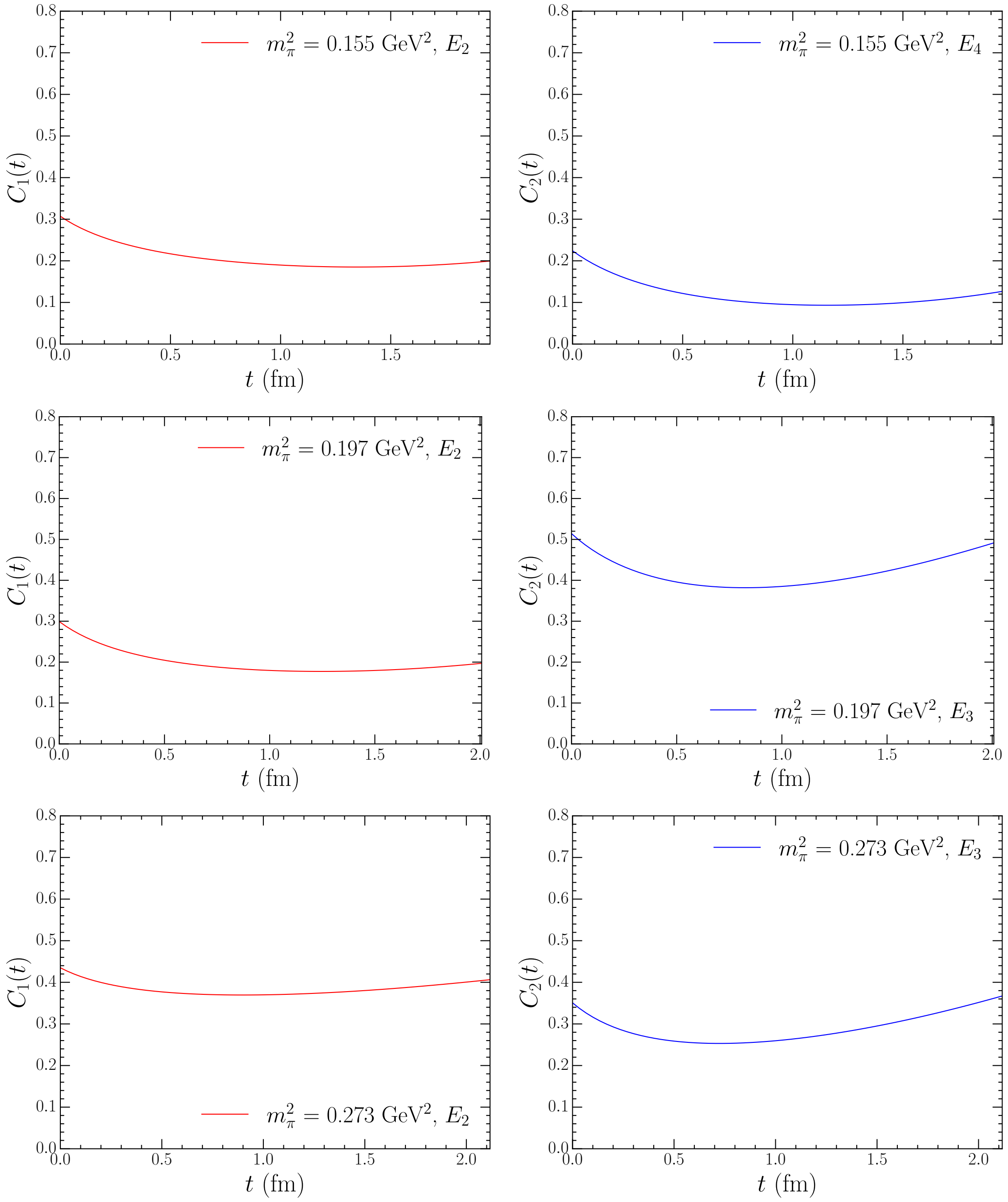

Figure 5.11: Contamination functions from Eq. (5.17) at the three pion masses considered by the HSC [77, 78], with a lattice size $L \sim 2$ fm. The pion mass increases as one moves down the columns. Contributions from the eigenstate with the largest eigenvector component for each bare basis state have been removed from the correlation functions (solid highlighted states in Fig. 5.4). Values for α_i and β_i are taken from the HEFT eigenvectors as defined in Eq. (5.18). The relevant eigenstate for each lattice QCD energy level is labelled by E_i.

In Fig. 5.11, results for the six contamination functions corresponding to the six lattice QCD results reported by the HSC are illustrated. These curves can be compared with the first two rows of Fig. 5.10 reporting results at similar pion masses on a 3 fm lattice.

While the large contamination reported in the top-right plot of Fig. 5.10 does not appear, broad improvement is not observed. The second state at the HSC middle mass and the first state at their heaviest mass both show scattering state contamination at 40%. As discussed in further detail below, both of these states sit in the midst of avoided level crossings.

Focusing first on the middle mass, the contributions from the second bare state are roughly equally spread between two eigenstates, making it difficult to conclusively comment on the eigenstate to which the lattice QCD energy corresponds. As only one of these states is removed in calculating the contamination function, there is still an eigenstate containing approximately 40% of the second bare state in the remaining correlation function.

Interestingly, the $C_1(t)$ contamination function for the heaviest pion mass in the lower-left plot of Fig. 5.11 is significantly greater than the contamination functions for the two lighter pion masses. This may provide an explanation for why the lower-energy HSC state sits at an energy lower than that predicted by HEFT. The HSC correlation function has a significant contamination from the lower-lying scattering state and the mass obtained in their analysis likely corresponds to a superposition of these two eigenstate energies.

5.6 Conclusion

In this final chapter, we have performed the first HEFT study of a system containing two bare baryon basis states, in the context of the $N^*(1535)$ and $N^*(1650)$ resonances. Here we found that the Hamiltonian for this system is able to provide an excellent description of infinite-volume physics, consistent with contemporary calculations of the pole positions for these resonances.

By comparing to recent lattice QCD results, we find that the two odd-parity nucleon resonances are best described by an interpretation of a three-quark core, with strong contributions from πN, ηN, and $K\Lambda$ rescattering. However, the contributions from rescattering processes decrease as the quark mass increases, resulting in a quark-model-like interpretation in-line with recent lattice QCD calculations of the magnetic moments for these two resonances.

In addition, we presented a novel method for simulating the contamination to lattice QCD correlation functions from scattering state contributions. Here we found a remarkable agreement between HEFT eigenvectors, and overlaps of the interpolating fields used to excite energy eigenstates in lattice QCD. These simulations also demonstrated the need for future high-quality lattice QCD studies containing five-quark momentum-projected meson-baryon interpolating fields, due to the large degree of scattering state contamination at lighter quark masses.

6

CONCLUDING REMARKS

In this dissertation, we have demonstrated a unique approach in the determination of baryon structure. Through a simultaneous consideration of both infinite-volume and finite-volume physics we are able to gain a descriptions of baryons that are consistent with both scattering data, and lattice QCD. This combination provides important constraints that facilitate an unambiguous determination of the structure of baryon resonances.

In Chapter 3, we examined the role of regularisation in baryon structure with the $\Delta(1232)$ as a case study. By considering a range of regulators and regularisation parameters, we demonstrated the degree to which model-dependence manifests in the HEFT eigenmodes. In the single-channel πN case, we were able to demonstrate the independence of the finite-volume eigenenergies over a very board range of regulator parameter. While the eigenvalues are insensitive to the regulator, the eigenvectors are dependent on choice of regulator, and the structure inferred is dependent on the regularisation of the theory. However, this model-dependence does reveal the interesting result, where for an unphysically large regulator parameter the $\Delta(1232)$ is able to be dynamically generated.

Upon introducing a second two-particle channel, $\pi\Delta$, the range of regulator parameter able to describe the experimental data becomes small, limited to phenomenologically-motivated values associated with the induced pseudoscalar form factor of the nucleon. The Hamiltonian becomes a model where the shape and extent of the form factors that regulate the interactions becomes important in describing the data. The outcome is that the Hamiltonian becomes constrained, though lattice QCD results can be used to further constrain the Hamiltonian. In particular, future excited state lattice QCD results will be able to better constrain the regulator parameter best able to describe the $\Delta(1232)$ system. With enough information, the Hamiltonian and its eigenvectors are determined such that the structure of the states is revealed. Comparison was also made with two additional sets of contemporary lattice QCD data, where further agreement between HEFT and lattice QCD was found.

Following this, Chapter 4 focuses on the introduction of a second bare basis state to a toy $\Delta(1232)$ system. By considering the lowest-energy resonance, we were able to gain unique insight into the role of a second bare state in both infinite-volume and finite-volume physics. We considered how the position of poles in the T-matrix are affected by a second bare state in two different cases, where the mass of the second bare basis state lies either above or below the mass of the first. Examining the effects of a second bare state on the finite-volume energy spectrum, we were able to gain new insight into the relationship between infinite-volume poles and finite-volume energy spectra.

Utilising the intuition and understanding obtained in the previous two chapters, in Chapter 5 we consider the two low-lying odd-parity nucleons. Motivated by recent lattice results showing the magnetic moments of lattice QCD states in the vicinity of the two low-lying odd-parity nucleon resonances agree with quark model predictions, we proceed to associate a bare basis state with each of the low-lying resonances. The idea is that the interactions with πN, ηN, and $K\Lambda$ will mix the bare basis states in forming the energy eigenstates. This HEFT description is consistent with both experimental data, and lattice QCD results. The consistency was found for lattice QCD results at three lattice volumes, with eigenvector analysis allowing for key insight into the structure of these eigenstates. Lattice QCD eigenstates which were excited by three-quark and five-quark operators both correspond with HEFT eigenstates with the appropriate eigenvector components. As a result, we conclude that both of the odd-parity nucleon resonances can be interpreted as three-quark cores dressed by πN, ηN, and $K\Lambda$ interactions.

To conclude Chapter 5, we presented a novel simulation of scattering state contaminations in lattice QCD correlation functions at 2 and 3 fm. These results demonstrate a need for multi-particle interpolating fields in next-generation simulations, in order to gain a better understanding of the complexities of the finite-volume spectrum. This becomes increasingly essential as contemporary lattice QCD studies are performed at or near the physical point.

Further work in HEFT should build upon these results, with a particular focus on systems with multiple bare basis states. In the positive-parity nucleon and Δ spectra, low-lying resonances appear to be a mixture of three-quark like, and dynamically generated through interactions between two-particle states. Future studies in these systems will therefore require the inclusion of two or more bare basis states to fully describe the spectrum, and lead to a better understanding of baryon structure.

A

BARE COMPONENT OF THE T-MATRIX

As outlined in Sec. 2.3.1, the T-matrix may be found as a solution of

$$T_{\alpha\beta}(k,k';E) = \tilde{V}_{\alpha\beta}(k,k';E) + \sum_{\gamma} \int dq\, q^2\, \frac{\tilde{V}_{\alpha\gamma}(k,q;E)\, T_{\gamma\beta}(q,k';E)}{E-\omega_\gamma + i\varepsilon}\,. \tag{A.1}$$

The solution of this equation may be written as

$$T_{\alpha\beta}(k,k';E) = t_{\alpha\beta}(k,k',E) + T^{\text{bare}}_{\alpha\beta}(k,k';E)\,, \tag{A.2}$$

where the background $t_{\alpha\beta}(k,k';E)$ is found by turning off the contributions from bare basis states, effectively setting the couplings $g^{B_0}_\alpha$ to zero.

To solve for $T^{\text{bare}}_{\alpha\beta}(k,k';E)$, we rewrite the T-matrix of Eq. (A.1) in a simple matrix notation, giving

$$T = V + \frac{g\, g^*}{E - m_{B_0}} + \left(V + \frac{G\, G^*}{E-m_{B_0}}\right) Q\, T\,. \tag{A.3}$$

Here, we have suppressed the function arguments for clarity, and have made the transformations

$$\begin{aligned} T_{\alpha\beta}(k,k';E) &\to T\,,\\ V_{\alpha\beta}(k,k') &\to V\,,\\ G^{B_0}_\alpha(k) &\to G\,,\\ q^2\,\Delta q &\to Q\,. \end{aligned} \tag{A.4}$$

Similarly, the background t-matrix from Eq. (2.24) has the matrix form

$$t = V + VQ\, t\,. \tag{A.5}$$

Due to the Hermicity of these matrices, this results in the identities

$$\begin{aligned} 1 + Q\, t &= (1 - Q\, V)^{-1}\,,\\ 1 + t\, Q &= (1 - VQ)^{-1}\,, \end{aligned} \tag{A.6}$$

which will be applied in the following text.

Rearranging Eq. (A.3), we find

$$\begin{aligned}
T - V Q T &= V + \frac{G\,G^*}{E - m_{B_0}} + \frac{G\,G^*}{E - m_{B_0}} Q\,T\,, \\
\implies (1 - VQ)\,T &= V + \frac{G\,G^*}{E - m_{B_0}} \left(1 + Q\,T\right)\,, \\
\implies T &= (1 - VQ)^{-1}\,V + (1 - VQ)^{-1}\,\frac{G\,G^*}{E - m_{B_0}} \left(1 + Q\,T\right)\,, \\
\implies T - t &= (1 + t\,Q)^{-1}\,\frac{G\,G^*}{E - m_{B_0}} \left(1 - Q\left(V + \frac{G\,G^*}{E - m_{B_0}}\right)\right)^{-1}\,. \qquad \text{(A.7)}
\end{aligned}$$

As $T = t + T^{\text{bare}}$, we have therefore found an expression for the bare component of the T-matrix. This may be rearranged into a more convenient form, giving

$$\begin{aligned}
T^{\text{bare}} &= (G + t\,Q\,G)\;G^*\;\{(E - m_{B_0})\,(1 - Q\,V) - Q\,G\,G^*\}^{-1}\;Q\,Q^{-1}\,, \\
&= (G + t\,Q\,G)\;G^*\left\{(E - m_{B_0})\,\left(Q^{-1} - V\right) - G\,G^*\right\}^{-1}\;Q^{-1}\,, \\
&= (G + t\,Q\,G)\;G^*\left\{E - m_{B_0} - \frac{G\,G^*}{Q^{-1} - V}\right\}^{-1}\left(Q^{-1} - V\right)^{-1}\,Q^{-1}\,, \\
&= (G + t\,Q\,G)\;\left\{E - m_{B_0} - G^*\,(1 - Q\,V)^{-1}\,Q\,G\right\}^{-1}\;G^*\;(1 - Q\,V)^{-1}\,, \\
&= (G + t\,Q\,G)\;\{E - m_{B_0} - G^*\;(1 + Q\,t)\;Q\,G\}^{-1}\;G^*\;(1 + Q\,t)\,, \\
&= (G + t\,Q\,G)\;\frac{1}{E - m_{B_0} - G^*\;(1 + Q\,t)\;Q\,G}\;(G^* + G^*\,Q\,t)\,, \\
&= (G + t\,Q\,G)\;\frac{1}{E - m_{B_0} - G^*\,Q\,G - G^*\,Q\,t\,Q\,G}\;(G^* + G^*\,Q\,t)\,. \qquad \text{(A.8)}
\end{aligned}$$

Considering the left-most term of this equation, returning to an integral notation we have

$$G + t\,Q\,G \to G_\alpha^{B_0}(k) + \sum_\gamma \int dq\,q^2\,\frac{t_{\alpha\gamma}(k, q; E)\,G_\gamma^{B_0}(q)}{E - \omega_\gamma(q) + i\varepsilon}\,, \qquad \text{(A.9)}$$

which is exactly the form of $\mathcal{G}_\alpha^{B_0}(k; E)$ from Eq. (2.37). Similarly for the right-most term of Eq. (A.8), we obtain $\mathcal{G}_\alpha^{B_0\,\dagger}(k; E)$. Finally, converting the terms in the denominator of Eq. (A.8) to an integral notation gives

$$G^*\,Q\,G \to \sum_\gamma \int dq\,q^2\,\frac{G_\gamma^{B_0}(q)\,G_\gamma^{B_0'}(q)}{E - \omega_\gamma(q) + i\varepsilon}\,, \qquad \text{(A.10)}$$

which is the self-energy $\Sigma_{B_0, B_0'}(E)$ from Eq. (2.44). Similarly, given the separable nature of the background t-matrix, with $t_{\alpha\beta}(q, q'; E) = f_\alpha(q)\,\tilde{t}_{\alpha\beta}(E)\,f_\beta(q')$, we also have the transformation

$$
\begin{aligned}
G\,Q\,t\,Q\,G \to & \sum_{\alpha\beta} \int dq\, q^2 \,\frac{G_\alpha^{B_0}(q)\, f_\alpha(q)}{E - \omega_\alpha(q) + i\varepsilon}\, \tilde{t}_{\alpha\beta}(E) \int dq'\, q'^2 \,\frac{f_\beta(q')\, G_\alpha^{B_0}(q')}{E - \omega_\alpha(q') + i\varepsilon}\,, \\
= & \sum_{\alpha,\beta} g_{f,\alpha,B_0}(E)\, \tilde{t}_{\alpha\beta}(E)\, g_{f,\beta,B_0'}(E) \qquad \text{(A.11)}
\end{aligned}
$$

which results in the expression for the background self-energy $\Sigma^{\mathrm{I}}_{B_0,B_0'}(E)$ from Eq. (2.47).

BIBLIOGRAPHY

[1] Chen-Ning Yang and Robert L. Mills. Conservation of Isotopic Spin and Isotopic Gauge Invariance. *Phys. Rev.*, 96:191–195, 1954.

[2] Michael E. Peskin and Daniel V. Schroeder. *An Introduction to quantum field theory*. Addison-Wesley, Reading, USA, 1995.

[3] R. L. Workman et al. Review of Particle Physics. *PTEP*, 2022:083C01, 2022.

[4] Waseem Kamleh, James Crawford Biddle, Derek B. Leinweber, and Adam Virgili. Emergent phenomena from centre vortices in dynamical QCD. *PoS*, LATTICE2022:397, 2023.

[5] James C. Biddle, Waseem Kamleh, and Derek B. Leinweber. Centre vortex structure in the presence of dynamical fermions. 2 2023.

[6] David J. Gross and Frank Wilczek. Ultraviolet Behavior of Nonabelian Gauge Theories. *Phys. Rev. Lett.*, 30:1343–1346, 1973.

[7] Murray Gell-Mann. The Eightfold Way: A Theory of strong interaction symmetry. 3 1961.

[8] Zhan-Wei Liu, Waseem Kamleh, Derek B. Leinweber, Finn M. Stokes, Anthony W. Thomas, and Jia-Jun Wu. Hamiltonian effective field theory study of the $\mathbf{N^*(1440)}$ resonance in lattice QCD. *Phys. Rev. D*, 95(3):034034, 2017.

[9] Jia-jun Wu, Derek B. Leinweber, Zhan-wei Liu, and Anthony W. Thomas. Structure of the Roper Resonance from Lattice QCD Constraints. *Phys. Rev. D*, 97(9):094509, 2018.

[10] Jonathan M. M. Hall, Waseem Kamleh, Derek B. Leinweber, Benjamin J. Menadue, Benjamin J. Owen, Anthony W. Thomas, and Ross D. Young. Lattice QCD Evidence that the $\Lambda(1405)$ Resonance is an Antikaon-Nucleon Molecule. *Phys. Rev. Lett.*, 114(13):132002, 2015.

[11] Zhan-Wei Liu, Jonathan M. M. Hall, Derek B. Leinweber, Anthony W. Thomas, and Jia-Jun Wu. Structure of the $\mathbf{\Lambda(1405)}$ from Hamiltonian effective field theory. *Phys. Rev. D*, 95(1):014506, 2017.

[12] Kenneth G. Wilson. Confinement of Quarks. *Phys. Rev. D*, 10:2445–2459, 1974.

[13] Christof Gattringer and Christian B. Lang. *Quantum chromodynamics on the lattice*, volume 788. Springer, Berlin, 2010.

[14] G. C. Wick. Properties of Bethe-Salpeter Wave Functions. *Phys. Rev.*, 96:1124–1134, 1954.

[15] M. Lüscher. Volume dependence of the energy spectrum in massive quantum field theories I. Stable particle states. *Communications in Mathematical Physics*, 104(2):177–206, June 1986.

[16] M. Lüscher. Volume dependence of the energy spectrum in massive quantum field theories II. Scattering states. *Communications in Mathematical Physics*, 105(2):153–188, June 1986.

[17] Martin Lüscher. Two-particle states on a torus and their relation to the scattering matrix. *Nuclear Physics B*, 354(2):531–578, May 1991.

[18] Jia-Jun Wu, T.-S. H. Lee, A. W. Thomas, and R. D. Young. Finite-volume Hamiltonian method for coupled channel interactions in lattice QCD. *Physical Review C*, 90(5):055206, November 2014.

[19] Song He, Xu Feng, and Chuan Liu. Two particle states and the S-matrix elements in multi-channel scattering. *JHEP*, 07:011, 2005.

[20] Michael Lage, Ulf-G. Meissner, and Akaki Rusetsky. A Method to measure the antikaon-nucleon scattering length in lattice QCD. *Physics Letters*, B681:439–443, 2009.

[21] V. Bernard, M. Lage, U. G. Meissner, and A. Rusetsky. Scalar mesons in a finite volume. *JHEP*, 01:019, 2011.

[22] Peng Guo, Jozef Dudek, Robert Edwards, and Adam P. Szczepaniak. Coupled-channel scattering on a torus. *Physical Review*, D88(1):014501, 2013.

[23] B. Hu, R. Molina, M. Döring, and A. Alexandru. Two-flavor simulations of the $\rho(770)$ and the role of the $K\overline{K}$ channel. *Physical Review Letters*, 117(12):122001, September 2016.

[24] Ning Li and Chuan Liu. Generalized Lüscher formula in multi-channel baryon-meson scattering. *Physical Review D*, 87(1):014502, January 2013.

[25] Maxwell T. Hansen and Stephen R. Sharpe. Multiple-channel generalization of Lellouch-Lüscher formula. *PoS*, LATTICE2012:127, 2012.

[26] M. Döring, H.-W. Hammer, M. Mai, J.-Y. Pang, A. Rusetsky, and J. Wu. Three-body spectrum in a finite volume: The role of cubic symmetry. *Physical Review D*, 97(11):114508, June 2018.

[27] Maxwell T. Hansen and Stephen R. Sharpe. Lattice QCD and Three-particle Decays of Resonances. *Annual Review of Nuclear and Particle Science*, 69(1):65–107, October 2019.

[28] Tyler D. Blanton, Fernando Romero-López, and Stephen R. Sharpe. $I = 3$ three-pion scattering amplitude from lattice QCD. *Physical Review Letters*, 124(3):032001, January 2020.

[29] J. M. M. Hall, A. C. P. Hsu, D. B. Leinweber, A. W. Thomas, and R. D. Young. Finite-volume matrix Hamiltonian model for a $\Delta \rightarrow N\pi$ system. *Phys. Rev. D*, 87(9):094510, 2013.

[30] Zhan-Wei Liu, Waseem Kamleh, Derek B. Leinweber, Finn M. Stokes, Anthony W. Thomas, and Jia-Jun Wu. Hamiltonian effective field theory study of the $\mathrm{N}^*(\mathbf{1535})$ resonance in lattice QCD. *Physical Review Letters*, 116(8):082004, February 2016.

[31] Yan Li, Jia-Jun Wu, Curtis D. Abell, Derek B. Leinweber, and Anthony W. Thomas. Partial Wave Mixing in Hamiltonian Effective Field Theory. *Phys. Rev. D*, 101(11):114501, 2020.

[32] Zhan-Wei Liu, Jia-Jun Wu, Derek B. Leinweber, and Anthony W. Thomas. Kaonic Hydrogen and Deuterium in Hamiltonian Effective Field Theory. *Phys. Lett. B*, 808:135652, 2020.

[33] Yan Li, Jia-jun Wu, Derek B. Leinweber, and Anthony W. Thomas. Hamiltonian effective field theory in elongated or moving finite volume. *Phys. Rev. D*, 103(9):094518, 2021.

[34] Curtis D. Abell, Derek B. Leinweber, Anthony W. Thomas, and Jia-Jun Wu. Regularization in nonperturbative extensions of effective field theory. *Phys. Rev. D*, 106(3):034506, 2022.

[35] Dan Guo and Zhan-Wei Liu. Pion photoproduction off nucleon with Hamiltonian effective field theory. *Phys. Rev. D*, 105(11):114039, 2022.

[36] Ross Daniel Young, Derek Bruce Leinweber, and Anthony William Thomas. Convergence of chiral effective field theory. *Prog. Part. Nucl. Phys.*, 50:399–417, 2003.

[37] Derek Bruce Leinweber, Anthony William Thomas, and Ross Daniel Young. Physical nucleon properties from lattice QCD. *Phys. Rev. Lett.*, 92:242002, 2004.

[38] Derek Bruce Leinweber, Anthony William Thomas, and Ross Daniel Young. Power counting regime of chiral extrapolation and beyond. *PoS*, LAT2005:048, 2006.

[39] Murray Gell-Mann, R. J. Oakes, and B. Renner. Behavior of current divergences under SU(3) x SU(3). *Phys. Rev.*, 175:2195–2199, 1968.

[40] J. M. M. Hall, D. B. Leinweber, and R. D. Young. Power Counting Regime of Chiral Effective Field Theory and Beyond. *Phys. Rev. D*, 82:034010, 2010.

[41] Anthony William Thomas. Chiral Symmetry and the Bag Model: A New Starting Point for Nuclear Physics. *Adv. Nucl. Phys.*, 13:1–137, 1984.

[42] Gerald A. Miller, Anthony William Thomas, and S. Theberge. Pionic Corrections in the MIT Bag Model. *Comments Nucl. Part. Phys.*, 10(3):101–108, 1981.

[43] E. A. Veit, Anthony William Thomas, and Byron K. Jennings. KN Scattering in the Cloudy Bag Model: s, p and d Waves. *Phys. Rev. D*, 31:2242, 1985.

[44] B. Bagchi and B. Mulligan. Off-shell T matrices for a class of separable nonlocal potentials. *Phys. Rev. C*, 10:2197–2205, 1974.

[45] V. S. Vladimirov. *Equations of Mathematical Physics*. Marcel Dekker, Inc., 95 Madison Avenue, New York, New York 10016, 1971.

[46] E. Anderson, Z. Bai, C. Bischof, S. Blackford, J. Demmel, J. Dongarra, J. Du Croz, A. Greenbaum, S. Hammarling, A. McKenney, and D. Sorensen. *LAPACK Users' Guide*. Society for Industrial and Applied Mathematics, Philadelphia, PA, third edition, 1999.

[47] S. Aoki et al. 2+1 Flavor Lattice QCD toward the Physical Point. *Phys. Rev. D*, 79:034503, 2009.

[48] Christopher Michael. Adjoint Sources in Lattice Gauge Theory. *Nucl. Phys. B*, 259:58–76, 1985.

[49] Martin Luscher and Ulli Wolff. How to Calculate the Elastic Scattering Matrix in Two-dimensional Quantum Field Theories by Numerical Simulation. *Nucl. Phys. B*, 339:222–252, 1990.

[50] Oliver Bar. Nucleon-pion-state contribution in lattice calculations of moments of parton distribution functions. *Phys. Rev. D*, 95(3):034506, 2017.

[51] Judith A. McGovern and Michael C. Birse. On the absence of fifth order contributions to the nucleon mass in heavy baryon chiral perturbation theory. *Phys. Lett. B*, 446:300–305, 1999.

[52] Pierre A. M. Guichon, Gerald A. Miller, and Anthony William Thomas. The Axial Form-factor of the Nucleon and the Pion - Nucleon Vertex Function. *Phys. Lett. B*, 124:109–112, 1983.

[53] R. Piessens, E. de Doncker-Kapenga, C.W. Überhuber, and D.K. Kahaner. *Quadpack: A Subroutine Package for Automatic Integration*. Springer Series in Computational Mathematics. Springer Berlin Heidelberg, 2012.

[54] INS Data Analysis Center. `http://gwdac.phys.gwu.edu/`. Online.

[55] R. L. Workman, R. A. Arndt, W. J. Briscoe, M. W. Paris, and I. I. Strakovsky. Parameterization dependence of T matrix poles and eigenphases from a fit to πN elastic scattering data. *Phys. Rev. C*, 86:035202, 2012.

[56] M. J. D. Powell. An efficient method for finding the minimum of a function of several variables without calculating derivatives. *The Computer Journal*, 7(2):155–162, 1964.

[57] Ulf-G. Meissner and J. A. Oller. Chiral unitary meson baryon dynamics in the presence of resonances: Elastic pion nucleon scattering. *Nucl. Phys. A*, 673:311–334, 2000.

[58] B. Juliá -Díaz, T.-S. H. Lee, A. Matsuyama, and T. Sato. Dynamical coupled-channel model of πN scattering in the W $\leq$ 2 GeV nucleon resonance region. *Physical Review C*, 76(6), dec 2007.

[59] T. Sato and T. S. H. Lee. Dynamical Models of the Excitations of Nucleon Resonances. *J. Phys. G*, 36:073001, 2009.

[60] J. M. M. Hall, A. C.-P. Hsu, D. B. Leinweber, A. W. Thomas, and R. D. Young. Finite-volume matrix hamiltonian model for a $\Delta \to N\pi$ system. *Phys. Rev. D*, 87:094510, May 2013.

[61] X.-L. Ren, E. Epelbaum, J. Gegelia, and Ulf-G. Meißner. Meson-baryon scattering in resummed baryon chiral perturbation theory using time-ordered perturbation theory. *The European Physical Journal C*, 80(5), may 2020.

[62] S. Theberge, Anthony William Thomas, and Gerald A. Miller. The Cloudy Bag Model. 1. The (3,3) Resonance. *Phys. Rev. D*, 22:2838, 1980. [Erratum: Phys.Rev.D 23, 2106 (1981)].

[63] Colin Morningstar, John Bulava, Andrew D. Hanlon, Ben Hörz, Daniel Mohler, Amy Nicholson, Sarah Skinner, and André Walker-Loud. Progress on Meson-Baryon Scattering. *PoS*, LATTICE2021:170, 2022.

[64] John Bulava, Andrew D. Hanlon, Ben Hörz, Colin Morningstar, Amy Nicholson, Fernando Romero-López, Sarah Skinner, Pavlos Vranas, and André Walker-Loud. Elastic nucleon-pion scattering at $m_\pi = 200$ MeV from lattice QCD. 8 2022.

[65] Christian Walther Andersen, John Bulava, Ben Hörz, and Colin Morningstar. Elastic $I = 3/2$ p-wave nucleon-pion scattering amplitude and the $\Delta(1232)$ resonance from N_f=2+1 lattice QCD. *Phys. Rev. D*, D97(1):014506, 2018.

[66] Curtis D. Abell, Derek B. Leinweber, Anthony W. Thomas, and Jia-Jun Wu. Effects of multiple single-particle basis states in scattering systems. 5 2023.

[67] Curtis D. Abell, Derek B. Leinweber, Zhan-Wei Liu, Anthony W. Thomas, and Jia-Jun Wu. Low-lying odd-parity nucleon resonances as quark-model like states. 6 2023.

[68] Adrian L. Kiratidis, Waseem Kamleh, Derek B. Leinweber, and Benjamin J. Owen. Lattice baryon spectroscopy with multi-particle interpolators. *Phys. Rev. D*, 91:094509, 2015.

[69] C. B. Lang, L. Leskovec, M. Padmanath, and S. Prelovsek. Pion-nucleon scattering in the Roper channel from lattice QCD. *Phys. Rev. D*, 95(1):014510, 2017.

[70] Peter C. Bruns, Maxim Mai, and Ulf G. Meissner. Chiral dynamics of the S11(1535) and S11(1650) resonances revisited. *Phys. Lett. B*, 697:254–259, 2011.

[71] P. C. Bruns and A. Cieply. Coupled channels approach to ηN and $\eta' N$ interactions. *Nucl. Phys. A*, 992:121630, 2019.

[72] Finn M. Stokes, Waseem Kamleh, and Derek B. Leinweber. Elastic Form Factors of Nucleon Excitations in Lattice QCD. *Phys. Rev. D*, 102(1):014507, 2020.

[73] M. J. D. Powell. An efficient method for finding the minimum of a function of several variables without calculating derivatives. *The Computer Journal*, 7(2):155–162, 1964.

[74] M. Selim Mahbub, Waseem Kamleh, Derek B. Leinweber, Peter J. Moran, and Anthony G. Williams. Structure and Flow of the Nucleon Eigenstates in Lattice QCD. *Phys. Rev. D*, 87(9):094506, 2013.

[75] C. Alexandrou, T. Leontiou, C. N. Papanicolas, and E. Stiliaris. Novel analysis method for excited states in lattice QCD: The nucleon case. *Phys. Rev. D*, 91(1):014506, 2015.

[76] C. B. Lang and V. Verduci. Scattering in the πN negative parity channel in lattice QCD. *Phys. Rev. D*, 87(5):054502, 2013.

[77] Robert G. Edwards, Jozef J. Dudek, David G. Richards, and Stephen J. Wallace. Excited state baryon spectroscopy from lattice QCD. *Phys. Rev. D*, 84:074508, 2011.

[78] Robert G. Edwards, Nilmani Mathur, David G. Richards, and Stephen J. Wallace. Flavor structure of the excited baryon spectra from lattice QCD. *Phys. Rev. D*, 87(5):054506, 2013.

[79] Derek B. Leinweber, R. M. Woloshyn, and Terrence Draper. Electromagnetic structure of octet baryons. *Phys. Rev. D*, 43:1659–1678, 1991.